Neutronics and fuel performance analysis of TRISO-based accident tolerant fuel for PWRs

AA Mphofu

orcid.org/0000-0002-5273-5004

Dissertation accepted in fulfilment of the requirements for the degree *Master of Science in Engineering Sciences with Nuclear Engineering* at the North-West University

Supervisor:	Prof MH du Toit
Co-supervisor:	Mr F Reitsma

Graduation:	June 2023
Student number:	28862163

ABSTRACT

South Africa has one nuclear power plant in Cape Town called the Koeberg nuclear power station. This power station still uses conventional uranium dioxide fuel pellets and zirconium cladding. Since the Fukushima-Daiichi nuclear power plant accident, efforts have been made to design alternative nuclear fuel forms in cases of accident conditions. Significant efforts have been made to develop new fuel cladding with different materials to reduce hydrogen production and new fuel pellets that can retain the fission products within the pellet structure (Zinkle *et al.*, 2014). In the Fukushima-Daiichi accident the nuclear core melted, resulting in fission products being released into the environment, thus creating an inhabitable zone. This loss of land was costly, as in Japan land is valuable, as it is in South Africa. A loss of land in South Africa could lead to incalculable consequences for generations. South Africa began designing and manufacturing a Pebble Bed Modular Reactor (PBMR) for commercial use before the project was shelved (Thomas, 2008). Before the project was cancelled, TRISO particle fuel had already been successfully manufactured and tested under irradiation.

FCM fuel uses TRISO particles embedded in a SiC matrix instead of the traditional graphite matrix. This study evaluates and compares FCM and UO_2 fuel in LWR conditions for neutronics and fuel performance.

A simulation is carried out to determine the performance of FCM fuel using the software SERPENT and STACY to compare the performance results of UO_2 and FCM fuel. The FCM fuel performance results are compared to experimental results of other TRISO-based fuel experiments, but these are predominantly for gas reactor conditions; thus the comparison is limited.

It is noted that FCM fuel performs better than fuel used in the older TRISO-based technologies built for gas reactor conditions; these results diverge from other simulation results where it performs worse than its counterpart when simulated using a SiC matrix.

Keywords: SERPENT, STACY, FCM, TRISO

ACKNOWLEDGEMENT

I want to thank God almighty for his love and protection throughout my journey till now. This was only possible because of his grace.

Secondly, I would like to thank my supervisor Dr Marina du Toit, for her help and guidance. Thirdly co-supervisor Dr Frederik Reitsma for taking time out of his schedule to guide this dissertation

I want to thank Ngoatladi Mashilangako, Tlangani Ringane and Nomthandazo Sebini for their personal and professional support throughout the year.

I want to thank the National Nuclear Regulator and North-West University for their financial assistance and support of my studies.

Lastly, I would like to give a special thanks to my family -to my number one supporters Rachel, Lesego, Masego, Obed Mphofu and my uncle Mokhine, the late Billy Motaung and my grandmothers and grandfathers-Thank you for your support and guidance.

TABLE OF CONTENTS

LIST OF TABLES

LIST OF FIGURES

NOMENCLATURE

Becquerel	Bq
Beginning of cycle	BOC
Carbon Monoxide	CO
Effective full power day	EFPD
End of cycle	EOC
Exa-Becquerel	EBq
Fissions per initial heavy metal atoms	FIMA
Fuel performance modelling	FPM
Fully ceramic microencapsulated fuel	FCM
Hot zero power	HZP
Inner Pyrolytic Carbon	IPyC
Light Water Reactor	LWR
Low enriched uranium	LEU
Middle of cycle	MOC
Oak ridge national laboratory	ORNL
Outer Pyrolytic Carbon	OPyC
Parts per million	ppm
Pressurised Water Reactor	PWR
Silicon Carbide	SiC
Source Term Analysis Code System	STACY
The Department of Energy Next Generation Nuclear Plant	DOE-NGNP
Thorium dioxide	ThO2
Tristructural-Isotropic	TRISO
Uranium Carbide Oxide	UCO
Uranium dioxide	UO2
Zircaloy	Zr

LIST OF SYMBOLS

Reactor multiplication factor	$\boldsymbol{k_{eff}}$
Enrichment of U_{234} in uranium	χ_{234}
Enrichment of U_{235} in uranium	χ_{235}
Enrichment of U_{238} in uranium	χ_{238}
The atomic mass of uranium	M_u
Caesium isotope 137	^{137}Cs
Silver metastable isotope 110	^{110m}Ag
Iodine isotope 131	^{131}I
Strontium isotope 90	^{90}Sr

CHAPTER 1: INTRODUCTION

1.1 Background

The nuclear accident at Fukushima Daiichi was one of the worst in the 21st century. It led to the anti-nuclear energy movement being revived worldwide, despite its low carbon emission. The accident began when a tsunami occurred because of a seismic slip rupture on the Pacific plate's rim, with a length of more than 500 km. The scram signal was activated to shut down all reactors, while simultaneously the transmission line tower to the Fukushima Daiichi nuclear power station collapsed, leading to a blackout at the power station. The emergency diesel generators mitigated the blackout, but a tsunami 15 metres high flooded the power station and the electrical equipment (Mizokami and Rempe, 2020).

Only three of the six reactor units operated that day, while the other three were in shutdown condition due to periodic inspections. The loss of electric power meant that the active systems could not remove the decay heat from the core, and the passive system could not efficiently remove heat in unit one, as the isolation condenser was not working and the time to restore power was too long. It led to the water in the reactor boiling and evaporating, fuel overheating, and fuel melting. The high-temperature steam reacted with the Zircaloy cladding to produce hydrogen, which led to a hydrogen explosion. The failure to remove heat from the core led to the degradation of the Zircaloy cladding, and the core melting led to the release of fission products and the reactor core melting through the containment building (Mizokami and Rempe, 2020).

The UO_2/Zr fuel system failed during the accident, and the plant was permanently damaged. Research into alternative fuel systems with better resistance to severe accident conditions was immediately initiated and is still underway, to be deployed in current operating reactors or for future designs. Accident Tolerant Fuel (ATF) is a proposed alternative fuel technology being developed. The aim is to find a fuel design compatible with the existing reactor systems that must have better resistance to accidents in order to limit the release of fission products and hydrogen production. One accident-tolerant fuel concept that garners interest is the change of cladding of the traditional Zircaloy material. Another is the improvement and changes to the traditional UO_2 pellets for TRISO-coated particle fuel (Hakim *et al.*, 2019). The shortcomings of the previous system have led to The Department of Energy Next Generation Nuclear Plant (DOE-NGNP) program requalifying the TRISO-coated particle fuel because of its ability to retain fission products (Lee *et al.*, 2013). This research will focus on the TRISO-coated fuel particle because of its known ability to retain fission products and the Fully Ceramic Microencapsulated

(FCM) matrix material that presents another fission product barrier.

The research will report on the neutronics, and fuel performance of the TRISO-coated fuel retrofitted for the PWR. Multiple studies have been conducted on TRISO-coated particles in light water reactors. For example, Lee et al. explore the neutronics of FCM Fuel Assemblies and cores using the Korean OPR-1000 reactor and the USA Westinghouse reactor as reference cores for their simulations (Powers *et al.*, 2013). Pope assesses the neutronic behaviour of fully ceramic microencapsulated (FCM) fuel in the PWR (Pope *et al.*, 2012).

The FCM fuel consists of TRISO fuel particles embedded in a SiC matrix and has been proposed for use in the PWR as the ATF concept. The advantage of the FCM is its ability to retain fission products and increase the time to fuel cladding failure. A common shortcoming regarding the FCM fuel is that it fails to maintain its cycle length and suffers from assembly power peaking issues arising from low reactivity in the FCM near the end of the cycle. Multiple studies focus on optimising fuel assembly geometry, packing methodology, increasing enrichment, and using large-diameter UN kernels at high packing fractions to alleviate the problem of shorter cycle lengths (IAEA, 2014).

It is critical to understand the nature of the SiC material in the FCM fuel as it is the first barrier before the fission products are released into the cladding system. An essential factor to consider is the gap between fuel and cladding, as the changes in the gap because of thermal expansion affect the thermal conductivity of the fuel assembly. Lavarenne's study on burnup-dependent modelling of fuel to clad gap conductance shows that the gap conductance increases linearly with the linear heat rating (Lavarenne *et al.*, 2022). Snead's study into the properties of SiC helps to lay the foundation for modelling the geometrical and thermal property changes during non-irradiated and irradiated SiC conditions (Snead *et al.*, 2007).

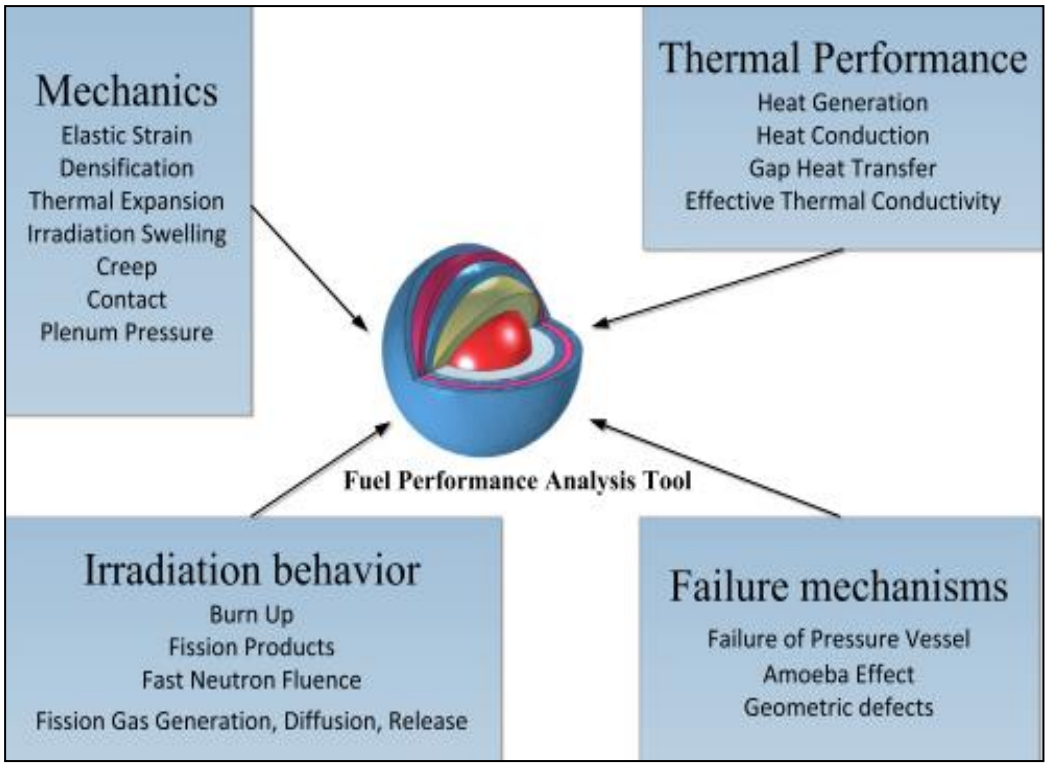

Figure 1-1:Modelling Structure of the TRISO fuel analysis tool (Zhang *et al*., 2020)

Zhang's paper illuminates a modelling structure of the TRISO fuel particle, as shown in Figure 1-1, and helps to show what variables and parameters should be considered when modelling using the modified fission gas release model (Zhang *et al.*, 2020). When examining different phenomena, we must remember that not all can be considered in our model due to resource constraints. For example, geometric defects might require detailed 3D finite element analysis. To model IPyC cracking, debonding, and asphericity, the computer code PARFUME uses results from Abaqus's detailed finite element analysis program in conjunction with its closed-form one-dimensional solution to make a statistical approximation of the stress levels in any particle (Collin and Power, 2013).

1.2 Problem statement

The Fukushima Daiichi disaster, earthquake and tsunami led to the loss of all power supply and consequential core meltdown and hydrogen explosions at three reactors. Substantial amounts of radioactive materials were released into the environment, leading to the evacuation and displacement of the public around the plant. Today, most BWRs (and PWRs) still use the same fuel pellet and zircaloy cladding pin form, which provides little trapping mechanism for fission gases and products once the zircaloy cladding fails than the other barriers like the pressurized loop and containment building are used as additional barriers. The fuel pellet's poor thermal conductivity and high-power density mean that the fuel has a high fuel centreline temperature,

making it more susceptible to melting, leading to zircaloy reacting with the coolant, producing hydrogen that can lead to the hydrogen explosions mentioned. The core melt can also efficiently inhibit the cooling or removal of decay heat, leading to additional radioactivity barrier failures (vessel, containment/confinement). Accident-tolerant fuel may be more effective in containing the radioactivity within the fuel pins during accidents.

1.3 Research aims and objectives

1.3.1 Aim

The research aims to compare the conventional PWR fuel pellet and FCM fuel at the same power levels in the standard 17 by 17 Westinghouse core. This entails evaluating the neutronics characteristics of both fuels and assessing the FCM fuel's ability to maintain the fission products within itself.

1.3.2 Objectives

- Run cases for 3D pin cell and fuel assembly with SERPENT using North-Anna as the representative PWR, using the conventional UO_2 fuel with Zircalloy cladding.
- Set up models for the FCM fuel compacts, which utilise randomly packed TRISO fuel format for North-Anna PWR utilising a 3D pin cell and fuel assembly design with burnup.
- Simulate normal operation for light water reactors using conventional and FCM fuel.
- Calculate the temperature profile of the UO_2 and FCM fuel.
- Determine the fuel cladding, coolant, and gap temperatures.
- Import data from neutronics calculations to run fuel performance calculations in STACY.
- Determine appropriate diffusion coefficients for individual layers based on literature.
- Extend STACY's code and model to take into account the SiC matrix.
- Compare the fuel performance of model data with experimental data where possible. Data is derived from literature or other sources.

1.4 Thesis statement

Simulate the fuel performance of the FCM fuel in the PWR for normal operating conditions and evaluate the FCM fuel's performance in terms of cycle length, neutron spectrum and releases and failures from the TRISO particles.

1.5 Structure of thesis

Chapter 2 explores the TRISO fuel characteristics, and the multiple studies conducted to use FCM in LWR conditions. Chapter 3 discusses the methodology used to conduct the simulations. Chapter 4 discusses the results of SERPENT and STACY codes. Chapter 5 compares the results from the codes and experimental results derived from the literature. Chapter 6 discusses the findings, shortcomings and recommendations for the study.

CHAPTER 2: LITERATURE REVIEW

2.1 Introduction

The original fuel form for the High-Temperature Gas Reactor was small coated particles called the TRISO particle fuel, embedded in a graphite matrix. This fuel development was continued by different countries worldwide, especially in South Africa, for the PBMR project (Gerczak, 2021). Many organisations are researching the feasibility and applications of FCM fuel in LWRs. The FCM technology and fabrication began at the Oak Ridge National Laboratory in the United States of America. The difference between the original TRISO particle fuel and the FCM fuel is that the matrix embedded is SiC instead of graphite (Al-Zahrani *et al.*, 2021).

Many papers exist regarding the use of FCM in LWR conditions. Deng's paper, for example, focuses on the neutronics and fuel cycle characteristics of the FCM fuel using the code OpenMC (Deng *et al.*, 2022). Powers' paper also examines FCM fuel in LWR conditions, using the Westinghouse 17 by 17 fuel as the reference core for their core analyses (Powers *et al.*, 2013). Lastly, Hakim's paper, like Powers and Deng's, focuses on the analysis of the neutronic and fuel characteristics of the FCM fuel, but Hakim's paper focuses on the performance of FCM fuel in small modular reactors using the SERPENT and SCALE codes (Hakim *et al.*, 2019). A commonality among these three primary papers mentioned is that uranium nitride is usually the fuel of choice rather than uranium oxide, because its higher density means more uranium atoms can fission. In all these papers, there is a tendency to change cladding material and fuel assembly arrangement to optimise for parameters for sustainable negative reactivity coefficient and burnup cycle length.

2.2 TRISO-coated particle

This section briefly explains the purpose and functions of each layer in the TRISO particle.

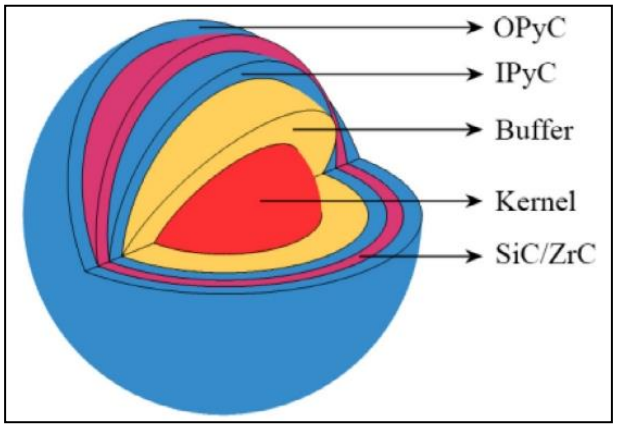

Figure 2-1:Drawing of TRISO-coated particle (Hales *et al*., 2013)

The TRISO particle fuel consists of four layers with different functions and the fuel kernel at the centre. Figure 2-1 shows that the kernel is coated repeatedly with different materials. Firstly, it begins with the kernel in the centre, followed by the porous carbon buffer layer. It is followed by the dense inner pyrolytic carbon layer (IPyC), silicon-carbon layer, and the dense outer layer pyrolytic carbon layer (OPyC).

2.2.1 Kernel

The spherical kernel contains fissionable fuel and is the first principal layer in delaying the release of fission products. A broad range of fissionable fuels exists, including UO_2, UC_2, and UCO. The primary difference between the UO_2 and UCO fuel is that UCO kernels can limit oxygen activity. This reduces the build-up of CO gas pressure and kernel migration phenomenon, which allows for higher burnup limits and thermal gradients (Wells *et al.*, 2021). The UN fuel is still an alternate fissionable fuel in the early stages of development, as the compound has a higher density and accommodates more uranium than the UO_2 fuel (Zakova, 2012).

2.2.2 Buffer

The roles of the buffer layer are to accommodate the irradiation-induced swelling in the kernel also to limit the pressure build-up by accommodating fission product gases and protect the IPyC from fission product recoil because the tension created in the layers experience creep which provides some relief to the SiC layer (Jiang *et al.*, 2021).

2.2.3 IPyC

The IPyC acts as a protective barrier for the kernel as chemical deposition of the SiC layer results in a chlorine attack on the kernel. The IPyC also protects the SiC layers from the fission product in the kernel, which is corrosive, and the IPyC has the dual function of relieving tensile stress in the SiC layer as well (Jiang *et al.*, 2021). This layer can essentially be considered the first load-bearing layer for providing structural support in the SiC Layer (Wells *et al.*, 2021).

2.2.4 SiC

The SiC layer is the primary barrier preventing metallic fission products from passing through the layer and the structural layer to handle tensile stresses (Jiang *et al.*, 2021). This layer essentially behaves as a pressure vessel for fission gasses produced inside the kernel, and its barrier is essential to ensure the impermeability of metallic fission products (Wells *et al.*, 2021).

2.2.5 OPyC

The OPyC layer is a secondary structure and fission gas barrier on top of the SiC layer. The layer provides a bonding area to the surrounding matrix material before being embedded into the matrix (Jiang *et al.*, 2021). This additional layer is helpful during the fuel compact formation as it helps protect the fuel particle (Verfondern, 2012).

2.3 Fuel failure mechanisms

Understanding how each TRISO layer behaves under irradiation and how the different fission products diffuse through each layer is essential. The advantage of the TRISO fuel is the various protective layers that help contain harmful fission products. The matrix material and grains also help to trap fission products. Simulating the release of fission products through the different layers is done by using Fick's classical law of diffusion (Fang *et al.*, 2021).

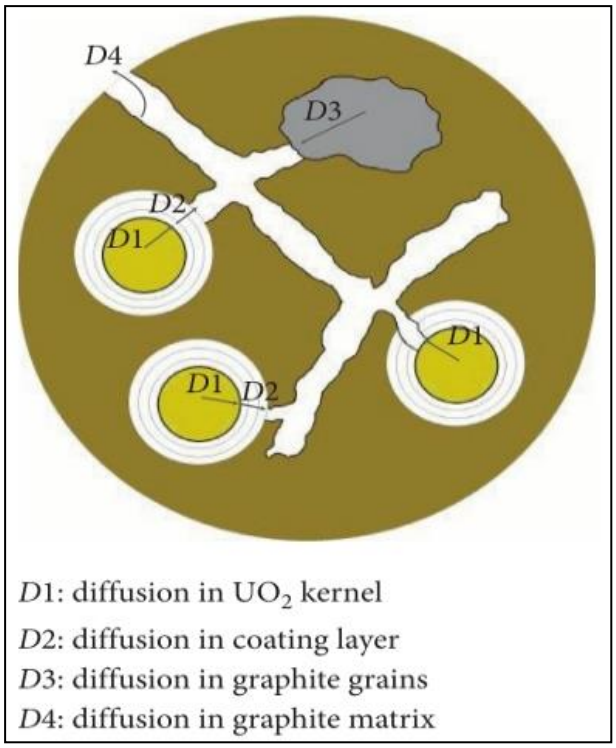

Figure 2-2:Diffusion coefficients of fission products (Fang et al., 2021)

The primary failure mechanism for TRISO-coated particles is mechanical and chemical failures. Mechanical failure is when the stress experienced is greater than the fracture strength, and chemical failure refers to the corrosion and decomposition of structural layers during irradiation, like SiC corrosion and kernel migration (Li *et al.*, 2021). Modelling the fuel performance of the FCM fuel requires a thorough understanding of the thermal-mechanical properties, the diffusion of fission products, and the release of fission products. Thermal-mechanical properties, diffusion of fission products, and release of fission products are important factors to understand (Jiang *et al.*, 2021). The art of modelling failure mechanisms in the TRISO fuel has proven difficult because most codes do not account for particular failure mechanisms in TRISO fuel, like debonding layers or SiC thinning. Statistical analysis methods predict failure fractions but use Weibull statistics in numerous fuel performance codes (Powers and Wirth, 2010).

When speaking about physical phenomena, it is essential to understand the influence of temperature, fast fluence, and burnup trajectories on fuel performance. This section briefly discusses primary failure mechanisms.

2.3.1 Pressure build-up from carbon monoxide formation

When ^{235}U fissions, two oxygen atoms are released, but about 1.67 of the oxygen atoms bind with the fission products. The excess oxygen then binds with the carbon-based layers like the pyrolytic carbon, leading to the production of CO. This process can damage the other layers as

carbon binds with other materials and the carbon binds when oxidation takes place to make CO. This CO can damage the SiC layer when the IPyC fails (Verfondern, 2012). Past developments in the USA favour using the UCO multi-phase mixture of UO_2, UC, and UC_2 because of its superior performance. The advantage of using UCO is that the lower production of CO is negligible, leading to a lower internal gas pressure, which lowers the probability of failure fractions (Jiang *et al.*, 2021).

When designing the kernel, an important design consideration is the oxygen potential. The oxygen potential is used as a barometer of which elements will successfully bind with oxygen and which will not. The oxygen potential increases as a function of burnup and leads to the production of CO. The production of CO leads to an increase in partial pressure, which translates directly into coating stresses (Eltawila, 2004).

2.3.2 Impact of irradiation on pyrolytic carbons

When the kernel is irradiated, the kernel swells and the buffer layer shrinks, which in turn causes the void volume for gases formed to decrease. Under-irradiation causes the inner pyrolytic carbon to experience a shrinkage in the radial and tangential directions. However, it begins to swell in the radial direction at modest irradiation, depending on the material's density, temperature, and anisotropy. This phenomenon can put the layers in tension in the tangential direction, which creates a compressive force on the rigid layer, provided it remains intact. Cracks or debonding at the interface may form during irradiation, and creep-induced irradiation can also lead to the failure of the layers (Verfondern, 2012).

2.3.3 Irradiation-induced IPyC cracking failure

Cracking in the IPyC has been attributed to the high anisotropy of the PyC layer and develops when internal stresses become greater than the fracture strength (Wells *et al.*, 2021).

2.3.4 Creep failure of PyC

Post-irradiation results reveal that thinned and failed PyC for temperatures greater than 2000 ℃ for long durations do not lead to direct failures of the SiC layer (Wells *et al.*, 2021).

2.3.5 Debonding between IPyC and SiC layers

When radial stress in the IPyC and SiC layers develops, debonding occurs because the radial stress exceeds the bond strength between the two layers. This happens because the larger tensile stresses in the SiC stresses and the IPyC shrinkage reduced tensile stress in the SiC layer (Verfondern, 2012).

2.3.6 Kernel migration

Kernel migration, or the amoeba effect, happens when the kernel is displaced closer to the coating layers of the TRISO particle. It is defined as the kernel reaching the IPyC layer, leading to a complete particle failure (Verfondern, 2012).

Kernel migration primarily depends on the fuel's temperature and macroscopic temperature gradient, with a secondary dependence on burnup (Wells *et al.*, 2021).

2.3.7 Pressure vessel failure

The phenomenon of coating layers failing, similar to pressure vessel failure, can occur during irradiation when fission gases accumulate in the porous buffer layer. The pressure build-up from fission gases increases with burnup, leading to the coating layers being in tensile stress until they burst into pieces. In a simplified model, the layer that behaves as the pressure vessel is the SiC layer and weakens during the irradiation in the fast fluence region. The layer will only fail when the internal pressure exceeds the tensile strength (Verfondern, 2012).

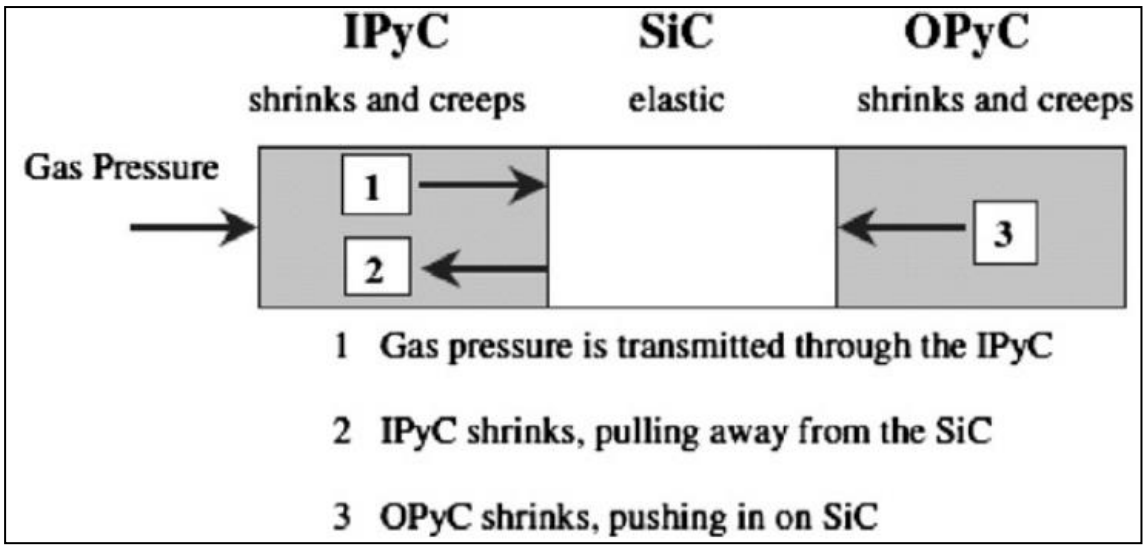

Figure 2-3:Pressure vessel TRISO layer interaction (Powers and Wirth, 2010)

Figure 2-3 shows that during the build-up of gas pressure, the forces transmit to the IPyC, SiC, and OPyC layers. Irradiation causes the IPyC and OPyC to shrink and creep while the SiC layer exhibits an elastic response, as seen in Figure 2-3 (Wells *et al.*, 2021).

Fast fluence impacts the radiation damage of the particles and changes in properties and dimensions in the layers (Wells, Phillips and Geelhood, 2021).

2.3.8 Fission product attack

In past experiments, noble metals travel from the kernel to the inner surface, which can damage the layer, leading to the failure of the SiC layer (Verfondern, 2012). Specifically, palladium and silver migrate from the kernel to the SiC layer, where damage occurs, and when the SiC layer fails, the IPyC and OPyC fail (Wells *et al.*, 2021).

2.3.9 Thermal decomposition of the SiC layer

Thermal decomposition refers particularly to constituents of SiC layers decomposing at temperatures above 2000°C and can lead to particle failure due to the degradation effect on the layer (Verfondern, 2012).

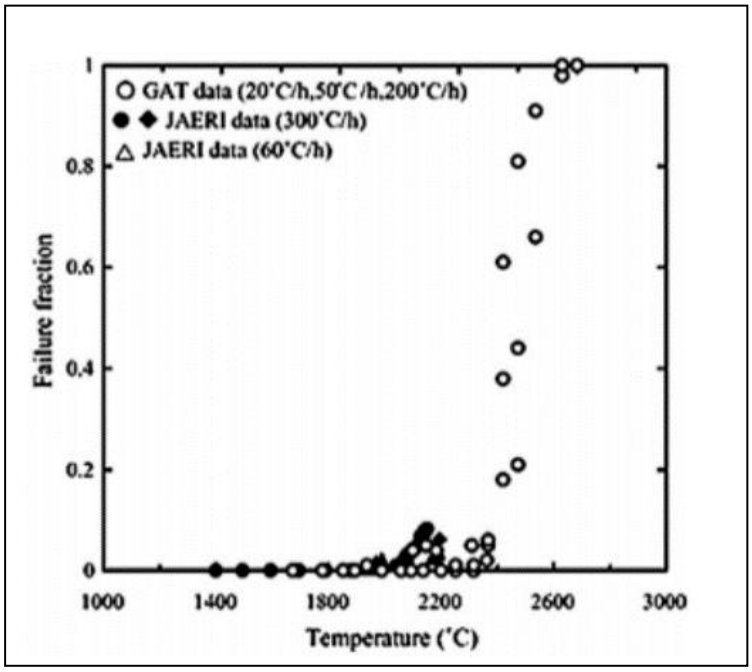

Figure 2-4:Failure fraction as a function of temperature for coated fuel particles (Wells *et al.*, 2021)

According to the paper by Wells and Phillips, Zhou and Tang summarised fuel tests performed by others on irradiated fuel particles to the temperature of 2600°C, and the results concluded that the failure began above 1800°C and that all particles failed at 2600°C, as shown in Figure 2-4 (Wells *et al.*, 2021).

2.3.10 Non-retentive SiC failure

This failure is broken down into two mechanisms, the diffusion release through intact SiC and the degradation of the SiC layer, which allow for measurable permeability. The SiC layer's degradation mechanism is CO corrosion and the diffusion of caesium through SiC layer (Wells

et al., 2021). The diffusion release through intact SiC is not considered a structural failure, but the SiC layer is, from the standpoint of functionality, a failure or degraded in some way (IAEA, 2010).

2.3.11 Kernel coating mechanical interaction failure

In a high temperatures environment, the gap between the kernel and coating layers closes as the presence of a strong temperature gradient leads to the migration of kernel and the carbon liberated in opposite direction and when the kernel migrates all the way through the buffer and hits the TRISO coating it is destroyed, which results in a mechanical interaction between the layers. This interaction is termed kernel-coated mechanical interaction (KCMI). Experimentally this failure has not been reported, but the IAEA states that modelling efforts have predicted that the SiC layer will fail quickly after the onset of KCMI (IAEA, 2010).

2.3.12 Summary

Exploring the different fuel failure mechanisms helps us understand the different parameters that affect the structural integrity of coated particles and which are the most common to most minor failure mechanisms for coated particles. It is also essential to understand that the STACY code does not account for every failure mechanism and particularly fails to account for fission product attacks for the element palladium as historically the focus is the strontium, caesium, iodine and krypton.

2.4 Fission product transport phenomena

This section will briefly discuss the transport and release of fission products.

2.4.1 Types of particles

In intact TRISO-coated particles, fission products diffuse away from the kernel to all the coating layers in the matrix. Each fission product diffuses at different rates through the layers before reaching the matrix material of the compact and the coolant. These transport rates are relatively minimal and can be practically negligible for short irradiation times but may build up over time, especially if very high temperatures are experienced. There are also defective TRISO-coated particles and failed particles considered to be bare fuel kernels in the modelling, where fission products do not necessarily travel through the coating layers but get released into the matrix material. These particles are considered in the modifications of the overall diffusion coefficients (Verfondern, 2012).

2.4.2 Inventory build-up

A broad spectrum of fission product nuclides is produced from fission. Most fission products have short half-lives and can form stable oxide compounds in the fuel kernel. Activation products like ^{134}Cs and ^{110m}Ag formed from neutron capture must be tracked. The decay of fission products affects the diffusion rates through coating layers. Radionuclides must be divided into short-lived and long-lived radionuclides to accurately account for the diffusion rate change through layers (Verfondern, 2012).

2.4.3 Initial distribution in accidents

There is an initial number of TRISO coated particles but some uranium particles are outside the fuel kernel or are in a specific layer due to the manufacturing process(Verfondern, 2012). This phenomenon is usually discussed as contamination outside the kernel (IAEA, 2010).

2.4.4 Recoil

At birth, fission products have high kinetic energy that travels a certain distance before stopping because of the surrounding material. In some cases, this can happen near the fuel kernel's surface directly into the buffer region, known as the recoil effect. There are other instances where fission products in the OPyC layer escape to the adjacent matrix material or fission products are formed in the matrix grains due to uranium contamination. This also can happen because fission products formed in the matrix grain can escape the grains without directly diffusing them into the grain boundaries. Direct recoil is independent of the irradiation parameters and temperature where fission products are released (Verfondern, 2012).

2.4.5 Chemisorption effect of metallic fission products

Due to adsorption and desorption processes, diffusing atoms transition at the boundary between the coolant flow and the fuel elements. In practice, adsorption is vital in cases where porous solids have a large specific surface (Verfondern, 2012).

2.4.6 Influence of chemical reactions on release behaviour

The chemical reactions in the nuclear reactor usually occur in the primary and secondary coolants for the following compounds: H_2O, CO_2, CO, and H_2 or N_2. These reactions occur in the HTGR of temperature ranges 300°C to 1200°C and are corrosive to the graphite core as they degrade the core structure. The reactions can be thermal, radiolytic or ad-sorptive; water carbon reactions are endothermal, making them consume nuclear decay heat. This leads to high temperatures and material loss in the reactor. When liquid water comes into contact with

graphite, the chemisorbed metallic fission products mobilise to form stable compounds with water because carbon reacts to form CO_2, CO. The process may liberate the chemisorbed metallic fission product at the surface This could be because of the degradation process that takes place at the surface (Verfondern, 2012). Nonetheless, this applies to helium as coolant for HTGRs not for LWRs where the coolant is water.

2.4.6.1 Influence of hydrogen reaction in the cladding system

The Zircaloy-4 cladding system of the LWR is a metal component meaning that it is susceptible to waterside corrosion and hydrogen pickup which alter the properties of the cladding system. Hydrogen is a highly reactive and flammable that is kept to a minimum (Suman, 2021).

According to Suman (2021) it confirmed that the creep and ductile strength decreases proportional to the concentration of hydrogen present in the system. This means that because of the extension of fuel burn-up there is a higher likelihood of hydrogen pickup. The cladding does provide a certain amount of protection from release of fission product (Suman, 2021).

2.4.7 Diffusion of fission products in TRISO particles

The FCM fuel during irradiation leads to the build-up of fission products, and these fission products go through the process of diffusion through the various layers because of the concentration gradients developed over time in the kernel, which forces the fission products to diffuse through the various layers out of the fuel (Gerczak, 2021). The diffusion mechanism in the TRISO particle is crucial as it determines the concentration and distribution of various fission products throughout the fuel and its various layers. This can be represented using the fission product species conservation or mass diffusion defined by Equation 2-1 (Hales *et al.*, 2021):

$$\frac{\partial C}{\partial t} + \nabla \cdot J + \lambda C - S = 0 \qquad 2\text{-}1$$

Where C is the concentration, λ and S are the radioactive decay constant and source rate of a specific species, and J is the mass flux. From Equation 2-1 , the fission product diffusion is derived and is given in the mass flux J, also known as Fick's law of diffusion in Equation 2-2 (Hales *et al.*, 2021):

$$J = -D\nabla C \qquad 2\text{-}2$$

Where D is the diffusion coefficient and is defined in the Arrhenius form as:

$$D = \sum_i D_{0,i}\, e^{\left(\frac{-Q_i}{RT}\right)} \qquad 2\text{-}3$$

In Equation 2-3, R is the universal gas constant, T is the temperature, Q is the activation energy, and D_0 is the pre-exponential factor. From Equation 2-3, we observe that diffusion is temperature dependent, but Hales mentions that $D_{0,1}$ is a function of the fast neutron fluence (Hales *et al.*, 2021).

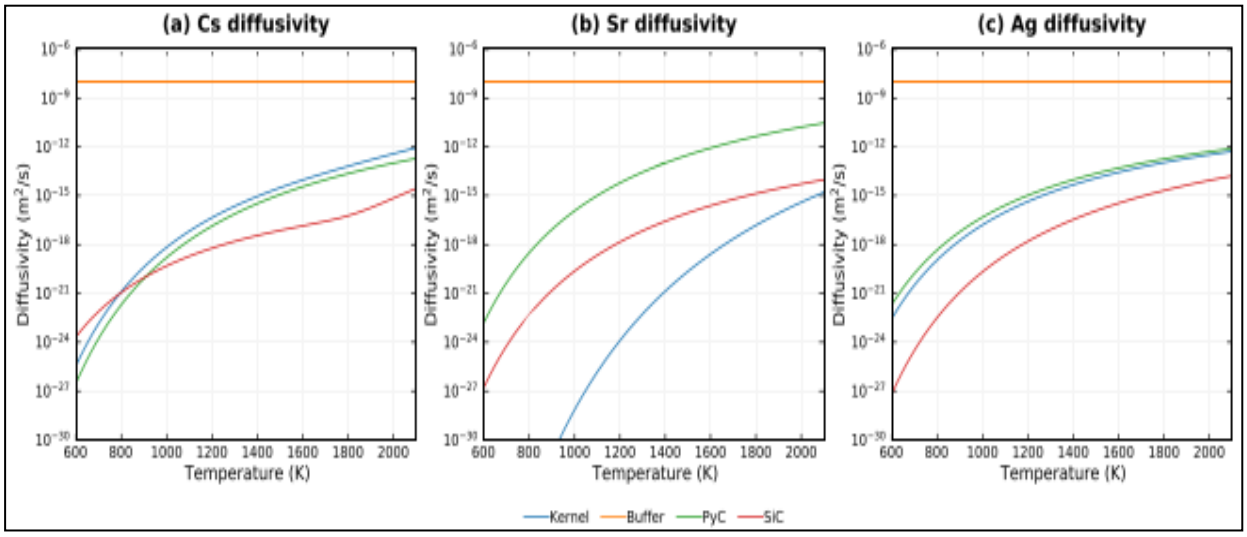

Figure 2-5:Diffusives of Cs, Sr and Ag in different layers from Hales (2021) (IAEA, 1997)

Figure 2-5 shows the diffusivities of caesium, strontium, and silver for the different TRISO layers for a fuel compact with a fuel radius of 251 µm. The fuel compact had reached a FIMA of 20% in the German advanced gas reactor and had received a neutron fluence of 5.5 x 10^{25} n/m^2. Hale modelled the fission product diffusion in the TRISO fuel particles with the BISON code and compared it with PARFUME results and experimental data (Hales *et al.*, 2021). The fundamental interest of this study is the constant diffusivity of the buffer layer, as the buffer layer is highly porous and has close to no retention ability. This attribute of the buffer layer could be used to describe the diffusivity of fission products in the pores of the matrix. The buffer diffusivity in Figure 2-5 can be considered synonym to rapid transport.

2.4.8 Summary

It is essential to understand the driving force for the diffusion and transport of fission products, as STACY does not categorise the method of transport. This helps to understand the practical limits of the simulation. It also shows which transport phenomena are essential in using FCM fuel in LWR conditions.

Notably, the transport of mobile fission metals is structure sensitive and more complex than

classical Fickean diffusion, as factors like lattice diffusion, grain boundary diffusion, and pore diffusion could be the driving mechanism for the migration of species; thus, Fick's law drives the overall migration process (Verfondern, 2012).

2.5 Fuel performance modelling

When it comes to modelling, it is crucial to consider the number of intact and defective coated particles as this affects the effective diffusion coefficients for different fission products in different layers. The coating layer's integrity affects the fission product transport and release behaviour. This also means that the fission product transport and release behaviour can affect the coating layer's performance, thus making the two dependent variables.

2.5.1 Simulation of fission product transport and release behaviour

The most common model is the numerical solution based on Fick's law of diffusion for the fission product transport in the TRISO fuel embedded in the graphite. The German codes FRESCO and GETTER and most codes that took part in the TECDOC-1674 benchmark were developed based on Fick's laws of diffusion (IAEA, 2012).

A modelling method used is the statistical modelling approach developed from a joint project by the USA and Germany. The model assumes that the SiC layer failure is more of a statistical phenomenon and uses the Weibull distribution for layer thickness distribution, which has a degradation rate distribution. Another method is the diffusion transport of fission product, which is calculated by assuming that fuel materials are homogeneous, which effectively leads to the calculation being called diffusion coefficients (Verfondern, 2012).

It is also essential to understand the quantity of fission products released by FCM fuel. The use of fuel performance codes helps simulate the generation, quantity, release, and radiation hazards in the nuclear power plant. Hence the quantity of fission products released from the fuel element through permeation and diffusion can contribute to the primary radioactivity source in the FCM fuel or the power plant (Fang *et al.*, 2021).

2.5.1.1 Transport of fission products

The rate of migration of fission product species through the homogeneous medium is called the mass flux, and the driving mechanism for migration is the concentration gradient. According to Fick's first law, as described by Cracks, flux for atoms diffusing in a medium is proportional to the concentration gradient (Verfondern, 2012):

$$J_r = -D\frac{\partial C}{\partial r} \quad 2\text{-}4$$

Where J_r is the diffusion flux (atoms $m^{-2}s^{-1}$), D is the diffusion coefficient (m^2s^{-1}), C is the concentration (atoms m^{-3}), and r is the spherical position from the centre of the coordinate system (Verfondern, 2012).

The Ficks second law describes diffusion by the time-dependent change of the concentration field. By assuming the diffusion coefficient D to be constant, including the source (e.g. production from the nuclear reaction) and the sink to also be constant (e.g., decay of radioactive materials), Fick's second law of diffusion can be written as follows (Verfondern, 2012):

$$\frac{\partial C}{\partial r} = D\left(\frac{\partial^2 C}{\partial r^2} + \frac{1}{r}\frac{\partial C}{\partial r}\right) - \lambda c + S \quad 2\text{-}5$$

Where λ is the decay constant (s^{-1}) and S is the fission source product. The purpose of Equations 2-4 and 2-5 is to develop a solution for Equation 2-5 by applying appropriate boundary conditions for the following:

$$\frac{\partial c}{\partial r}|_{r=0} = 0 \quad 2\text{-}6$$

$$c_1 = c_2 \;\&\; -D_1\frac{\partial c}{\partial r}|_1 = -D_2\frac{\partial c}{\partial r}|_2 \quad 2\text{-}7$$

Equation 2-6 boundary conditions assume zero concentration gradient at the radius centre, while Equation 2-7 boundary conditions assume the continuity of flux and concentration for two adjacent materials with different diffusion coefficients (D_1 and D_2) in Equation 2-7. A third boundary condition not shown assumes that the mass transfer can describe fission product transport from the fuel elements surface to the coolant. This boundary condition was developed for the application in HTGR and could be applied to PWR reactors with gap-filled helium or xenon (Verfondern, 2012).

2.5.1.2 The fission gas release

The release of long-lived fission products is modelled using the Booth model, which also relies on the direct recoil model. The model is broken down into a two-step process where firstly, the gas atoms are driven from the grains to the grain boundaries and then secondly, the gas atoms at the grain boundaries are released to the free surface of the fuel, where they are released into the free volume of the TRISO particle. The gas release fraction released by the kernel is given by Equation 2-8 (Jiang *et al.*, 2021):

$$FGR = (RF_{recoil} + [1.0 - RF_{recoil}]RF_{Booth})FGP \quad 2\text{-}8$$

In Equation 2-8, RF_{recoil} and RF_{Booth} are the release fractions of fission gases regarding the direct recoil and diffusion. The FGP(mol) is the amount of fission gases produced in moles in the kernel, and Equation 2-8 assumes that all fission gases are released into the void volume (Jiang *et al.*, 2021).

2.5.1.2.1 Direct recoil

Experimental data allows us to account for the direct kinetic release of fission gases from the kernel to buffer from geometrical considerations and fission fragment ranges. Assuming a gas mixture composed of 18.5 and 81.5% krypton and xenon, respectively, it gives us the following recoil fraction (Jiang *et al.*, 2021):

$$RF_{recoil} = 0.185RF_{recoil,Kr} + 0.815RF_{recoil,Xe} \quad 2\text{-}9$$

$RF_{recoil,Kr}$ and $RF_{recoil,Xe}$ are the release fractions due to recoil in Equation 2-9, and are the release fractions for krypton and xenon. They depend on the ranges of krypton and xenon in the kernel (i.e. r_i for i=Kr, Xe). The radius on the kernel is $r_k(m)$ which is given in Equation 2-10 (Jiang *et al.*, 2021):

$$RF_{recoil,i} = \frac{0.25\left(r_k^3 - [r_k - r_i]^3\right)}{r_k^3} \quad 2\text{-}10$$

2.5.1.2.2 Booth model

The diffusive release using the Booth equivalent sphere diffusion model uses estimates of releases through kernel grains to grain boundaries and then the transport through interconnected porosity. The Booth release fraction is given by Equation 2-11 (Jiang *et al.*, 2021):

$$RF_{Booth} = 1.0 - \frac{6r_{grain}^2}{Dt}\sum_{n=1}^{\infty}\frac{1 - e^{-\frac{n^2\pi^2 Dt}{r_{grain}^2}}}{n^4\pi^4} \quad 2\text{-}11$$

Where r_{grain} (m) is the radius of the diffusing sphere, D is the diffusivity of the fission gas in the grain, and t is the diffusion time (Jiang *et al.*, 2021).

2.5.1.3 Summary

Section 2.5.1 provided the fundamental framework used to measure and track the release and transport of long-lived fission gases and discussed the primary driving mechanism for the

transport of fission products used in most codes. It further cemented that the diffusion coefficient of fission products is a combination of various factors.

2.5.2 Simulation of coated particle performance

This section explains the fundamental framework used in the PANAMA code and subsequently used in the STACY to calculate failure fractions probability.

Powers and Wirth (2010) talks about fuel performance codes and how they can be categorised into two sections: closed-form analytical and numerical solutions. The closed solution is utilised to reduce 3D stress-strain displacement calculation for spheres to 1D symmetric spheres. This method allows a system of equations to be solved from the OPyC/Matrix boundary interface. The method is less computationally demanding than FEM analyses, thus allowing for a large set of particles to be solved. However, the method simplifies TRISO particles to the point where asphericity and temperature gradients across TRISO particles are ignored, together with many other factors. The method is only suitable for predicting pressure vessel failure, and other factors like cracking or debonding are 3D effects that have to be accounted for in different ways and are discussed further (Powers and Wirth, 2010).

Idaho National Laboratory in the United States developed the PARFUME code, which utilises Miller's analytical closed-form solution. The PARFUME code is unique because it incorporates multi-dimensional effects using 3D ABAQUS calculations to aid the 1D model. This allows PARFUME to account for most behaviour and failure mechanisms accurately. PARFUME also allows the user to specify boundary conditions to model external stresses on the TRISO particle if necessary (Miller *et al.*, 2010). Powers and Wirth (2010) mentions PARFUME and other codes that try to model the fuel performance of TRISO particles provided up to burnup levels of 20% FIMA for UO_2 fuels (Powers and Wirth, 2010).

Modelling the coated particle performance means simulating the mechanical performance of the TRISO-coated fuel particles. The principal modelling approach used depends on two independent failure mechanisms. The first is the pressure vessel failure with the degradation effect of the SiC layer of the particle. The second model is the thermal decomposition of the SiC, which depends on the temperature and burnup of the particle. The overall failure fraction is calculated from the Equation 2-12 and 2-14 to form Equation 2-15 (Verfondern, 2012).

2.5.2.1 Pressure vessel model

The pressure vessel model uses a simplified SiC layer that is assumed to be a thin shell similar to a soap bubble. Other layers in the TRISO particle are ignored, and it is understood that a

pressure vessel fails when the stress in the SiC layers is more than the tensile strength of the material, which can be represented in Equation 2-12 by the Weibull distribution. Equation 2-12 is the probability of a pressure vessel of a particle as a function of time and temperature. (Verfondern *et al.*, 2014):

$$\Phi(t,T)_p = 1 - \mathrm{e}^{-\mathrm{In}\ 2\ \mathrm{x}\left(\frac{\sigma_t}{\sigma_0}\right)^m} \qquad 2\text{-}12$$

The stress in the SiC layer, σ_t (Pa) is determined with the following equation for thin shell pressure vessel in Equation 2-13 (Verfondern *et al.*, 2014). σ_t (Pa) is determined with the following equation for a thin shell pressure vessel in Equation 2-13 (Verfondern *et al.*, 2014):

$$\sigma_\mathrm{t} = \frac{\mathrm{r} \times \mathrm{p}}{2\mathrm{d_o}} \times \frac{1 + (\dot{\mathrm{v}} \times \mathrm{t})}{\mathrm{d_o}} \qquad 2\text{-}13$$

In Equation 2-13, r is the mean radius of the SiC layer, p is the gas pressure inside the particle, d_o is the initial thickness of the SiC layer, $\dot{v}$ is the volume corrosion rate according to Montgomery, and t is time (Verfondern *et al.*, 2014).

2.5.2.2 Thermal decomposition model

In the thermal decomposition model, the failure of SiC is determined by applying the following semi-empirical relationship:

$$\Phi(\mathrm{t},\mathrm{T})_d = 1 - e^{-\alpha\xi^\beta} \qquad 2\text{-}14$$

In Equation 2-14, ξ is the action integral and α, β are empirical constants. The action integral ξ comprises the entire temperature time history experienced by the particle. The parameters α, β are different for loose particles or particles of fuel spheres and are derived from temperature tests up to 2500°C for particles irradiated in Experiment DR-K6 or AVR-GO2 spherical fuel elements (IAEA, 1997).

2.5.2.3 Overall failure fraction model

The overall failure fraction, $\Phi(\mathrm{t},\mathrm{T})_{total}$ is a combination of two single independent failure probabilities, $\Phi(\mathrm{t},\mathrm{T})_d$ and $\Phi(\mathrm{t},\mathrm{T})_p$ and is shown in Equation 2-15 (Verfondern, 2012):

$$\Phi(\mathrm{t},\mathrm{T})_{total} = 1 - \{(1 - \Phi(\mathrm{t},\mathrm{T})_d)(1 - \Phi(t,T)_p)\} \quad 2\text{-}15$$

2.5.3 Summary

Section 2.5 overall goes through the modelling methodology of different nuclear codes and the mathematical equations.

2.6 Neutronics analyses of FCM fuel in LWR conditions

This section discusses multiple studies that simulate the fuel performance of FCM in LWR conditions, their feedback coefficient, isotopes inventory, cycle length and failure fractions on coated particles.

Using FCM in PWRs has been researched extensively, especially for existing and new PWR reactors like the EPR and SMR water-based reactors. Institutions such as the Oak Ridge National Laboratory, Idaho National Laboratory and Brookhaven National Laboratory have done extensive research and confirmed the feasibility of FCM fuel in PWRs (Al-Zahrani *et al.*, 2021).

2.6.1 Studies concerning FCM in LWR conditions

The International Energy Research initiative (I-NERI) carried out a three-year study with the ORNL, USNC and the Korea Atomic Energy Research Institute (KAERI) to assess the feasibility of replacing the current fuel in LWR with the FCM fuel. The reference core used was the Westinghouse 17 by 17 core and the Korean OPR-1000 core with fuel assemblies of dimensions 16 by 16. USNC worked with the Westinghouse core while the KAERI took charge of the OPR-1000 core. The study compared the reactivity in the cycle length and evaluated the neutron spectra. In order to compare the UO_2 fuel and the FCM fuel, a new fuel assembly was devised. The FCM fuel in the study used uranium nitride because it had a higher density than UO_2 and had compatible characteristics (higher total uranium mass loading) with the reference 17 by 17 assembly in terms of power generation, thermohydraulics and neutronics (Powers *et al.*, 2013).

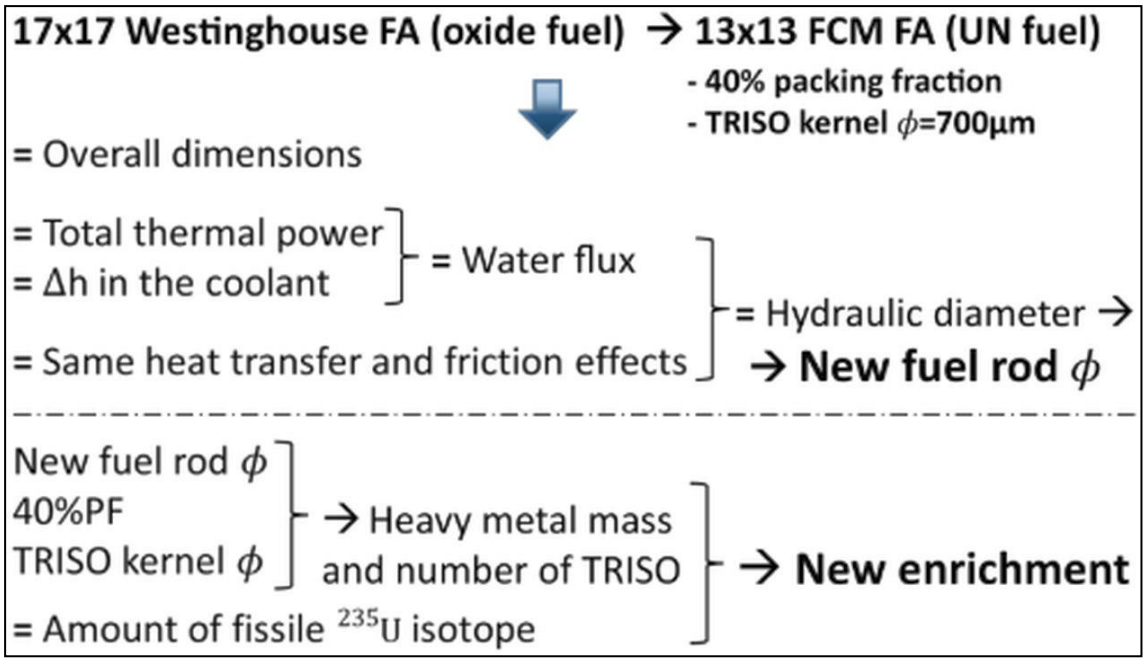

Figure 2-6:Fuel Assembly (FA) and packing fraction (PF) design criteria (Powers et al., 2013)

Figure 2-6 illustrates the first goal for the new assembly design, which is to maintain the overall thermohydraulic properties and neutronics between the reference fuel assembly and the new fuel assembly with the FCM fuel. The second goal is to maintain the same number of fissile ^{235}U isotopes of the reference and new fuel assembly models. It is important to note that the cladding for the new fuel assembly is simulated with zircaloy instead of alternate cladding (Powers *et al.*, 2013). More recent studies use SiC cladding when simulating a fuel assembly's neutronic behaviour because SiC has a small neutron capture capability, about 25% less than Zr alloys, for the same cladding wall thickness (Liu, 2017).

Another comparable study from Qasim et al. (2018) focuses on the small modular PWR loaded with FCM fuel. This study compares the traditional UO_2 and the FCM fuel by comparing their reactivity coefficients, power peaking factor, cycle length, rod cluster control assembly (RCCA) and shutdown margins. The fuel assemblies used in this study differ because they are trying to conserve the hydraulic diameter, as shown in Figure 2-5, and the I-NERI discussed previously. The paper states that using SERPENT is better than other methods like reactivity-equivalent physical transform (RPT) and volume-weighted homogenisation (VWH) because of its ability to deal with the double heterogeneity problem. The VWH produces substantial errors as it does not account for the self-shielding effects. For the RPT method, the results diverge after the beginning of the cycle (Qasim Awan *et al.*, 2018).

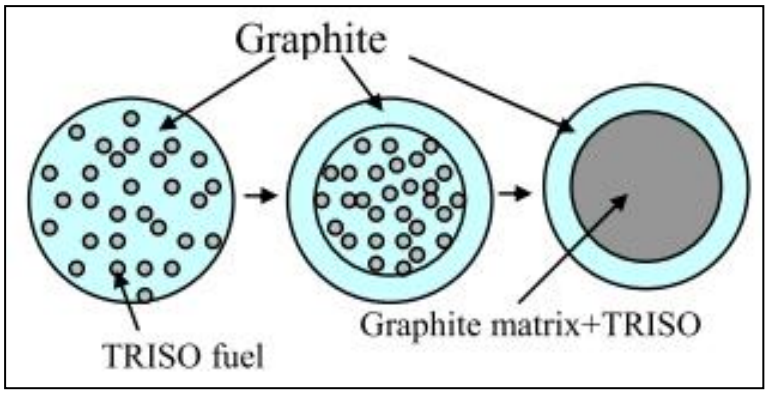

Figure 2-7:The RPT concept (Kim *et al*., 2005)

In the conventional pebble bed fuel, TRISO particles in a graphite matrix are randomly dispersed, and this typical configuration leads to the so-called double heterogeneous problem. Most conventional lattice codes cannot handle the double heterogeneity media, and the DRAGON code can handle it for limited accuracy. In order to use conventional lattice code systems, double heterogeneous regions are converted into homogeneous regions known as volume-weighted homogeneous, resulting in an under-estimated reactivity. For the RPT method, the self-shielding effect is adjusted by changing the physical configuration of the problem. This is depicted in Figure 2-7, where the fuel particles are moved into a smaller volume and then the inner heterogeneous region is homogenised for a volume-weighted method. The reduced radius of the new homogenous region in the centre is determined by trying to match the neutron multiplication factor of the reference core (Kim *et al.*, 2005).

According to Powers' findings, the required enrichment depends on the packing fraction and size of the TRISO particles. This means a simple invariance in fissile fuel is not enough because the lower total uranium mass loading means a faster depletion of the ^{235}U isotope as the burnup increases. A disadvantage of the FCM fuel is that the lower total uranium mass loading leads to the lower breeding of ^{239}Pu and ^{241}Pu isotopes. As for the moderator temperature coefficient (MTC), the FCM has less negative feedback during the first half of the cycle compared to the traditional UO_2 fuel, and the same can be said for the fuel temperature coefficient (FTC). The coolant void coefficient (CVR) shows safer behaviour for the 13 by 13 FCM fuel assembly than the 17 by 17 FCM fuel assembly. Failure fractions depend on the fluence, the strength of the SiC layer and the temperature, as a threshold exists for where the number of failure fractions increases exponentially (Powers *et al.*, 2013).

2.6.2 Other works on the neutronics analysis of FCM in LWRs

Table 2-1 lists studies that examine the behaviour of FCM fuel in LWR conditions, the analysis tools used, and the treatment of heterogeneity components and the type of codes and cell

treatment used by their respective codes.

Table 2-1:Different work done on neutronic analyses

Reference	Neutronic Transport code	Cell Treatment	Types of code
(Cho and Hong, 2020)	DeCart2D	Double heterogeneity	Monte Carlo code
(Pope et al., 2012)	DRAGON-4	Double heterogeneity	Deterministic code
(Al-Zahrani et al., 2021)	OpenMC	Double heterogeneity	Monte Carlo code
(Hakim et al., 2019)	SCALE6.1.2	Heterogeneity-homogeneity cell weighted	Monte Carlo code

Monte Carlo codes are more reliable than deterministic codes because they consider the self-shielding effect. An advantage to using Monte Carlo codes is that they are very flexible as they allow for new fuel cladding combinations or unconventional moderator (e.g. lead) combinations because there are fewer correction formulas or approximate formulas than in deterministic codes. Monte Carlo codes can also handle complex geometry problems, while deterministic codes have limited use. The only advantage deterministic codes have over Monte Carlo codes is that they are less computationally intensive and generally require little time to run (Chen and Yuan, 2017).

2.6.3 The contrast between irradiation behaviour in LWR and HTR

The main points in a paper by Powers are summarised below (Powers *et al.*, 2013) :

1. In an environment where the temperature can range from 600℃ to 950℃ and the gas pressure is below 4 MPa for a neutron fluence of 11 x 10^{21} n/cm^2 (E >0.18 MeV), for temperatures below 910℃, the primary gas species are xenon and krypton, but above 910℃, caesium becomes the primary gas specie.
2. The failure fraction for SiC increases with an increased fast fluence when assuming failure fraction using Weibull distribution, but this depends on the failure strength of the SiC and PyC layers. In an environment where the fast fluence is 8 x 10^{21} n/cm^2 (E> 0.18 MeV), the failure increases but is mitigated if the strength of PyC and SiC is 200 MPa and 400 MPa, respectively. This could be because the Weibull modulus may be a wider distribution with increasing fast fluence which makes the results linked to a high uncertainty.

It is important to note that the material properties are well understood for fast fluence under 4 x 10^{21} n/cm^2 and the parabolic correlation for irradiation-induced dimensional changes in particular layers. This is because the fast fluence in the typical HTR ranges from 4 to 5 x 10^{21}

n/cm^2 (E>0.18 MeV), while the fast fluence in the LWR has an extended range up to 10 x 10^{21} n/cm^2 (E>0.18 MeV). This means that the material properties derived from HTR experiments must be carefully extrapolated for the FCM fuel in LWR. The Weibull modulus in this case is six which means that that with an fast fluence increasing the mean value and a Weibull distribution becoming wider means the results are linked with high uncertainty (Powers *et al.*, 2013).

2.6.4 Summary

Section 2.6 compares how different experiments tried to compare the FCM and UO_2 fuel in a somewhat fairer way. The common design constraint would be to ensure that the number of ^{235}U is the same in the UO_2 and FCM fuel. This paper will also be adopted in this approach to have a fair comparison. This section also contrasts the behaviour of gas and water reactors.

2.7 SiC in FCM

2.7.1 Fabrication processes

In the FCM fuel, the most critical material of significant concern is the SiC matrix and layer because there are many fabrication routes. These different fabrication routes result in different mechanical properties. Various fabrication methods exist, such as sintering, direct conversion, gas phase reaction and polymer pyrolysis for synthesising SiC. The chemical vapour deposition (CVD) techniques primarily manufacture the SiC layer and produce highly crystalline, stoichiometric and high-purity β-SiC (Snead *et al.*, 2007).

Another standard fabrication route is a liquid phase sintering method called the nano-infiltration transient eutectic phase process (NITE). This method produces the SiC matrix and a dense SiC matrix, which is hot-pressed and processed to obtain the FCM pellets. The method uses fewer oxides additives and allows for lower temperature treatment (200-400°C) which archives properties close to the CVD SiC. Manufacturing methods dramatically affect the thermal and mechanical properties of SiC under non-irradiated and irradiated conditions (Deng *et al.*, 2022).

The NITE fabrication method is used only for the SiC matrix, while the SiC particle layer uses the CVD fabrication method. They both have similar material qualities and are assumed to have the same diffusion of fission product rates. This assumption will be used to carry out the simulation and is assumed because of the lack of consensus on NITE-SiC matrix material properties (Schappel, 2017).

2.7.2 High volume packing

A way to mitigate the reduced total uranium mass inventory is to increase the packing fraction

from the range of 34% to 40% to around the range of 44% to 74%. Historically a packing fraction of 60% was achieved for the Fort St. Vrain Reactor (Brown *et al.*, 2022). Increased packing fraction using conventional manufacturing methods (e.g. CVD) has shown that the number of particles broken in their final form increases with particle packing fraction, and experimental evidence has shown that particles are more likely to touch along the axis of compression than either perpendicular to the pressing direction (Morris and Pappano, 2007).

There are two methods for increasing the packing fraction proposed. The first is the use of multiple-sized particle sizes. The second is the conventional manufacture of TRISO particles and matrix materials using advanced manufacturing (Brown *et al.*, 2022). The latter approach was adopted for the Transformational Challenge Reactor (TCR) program sponsored by the USA Department of Energy. The approach relies on additive manufacturing to create the SiC matrix with the traditional CVD-TRISO particles (Terrani *et al.*, 2021).

2.7.2.1 TCR manufacturing

Figure 2-8 shows the entire fuel manufacturing process for the FCM fuel. The fuel element shell is first designed on CAD software and then printed using the binder jet method. The fuel element shell is filled with TRISO particles from traditional manufacturing methods. A SiC powder fills the interstitial spaces, the same one used in the binder jet. Then finally, chemical vapour infiltrates the fuel element and shell, resulting in the thermal decomposition of methyl trichlorosilane(MTS), and deposits a highly stoichiometric and crystalline SiC to fill the remaining pores (Terrani *et al.*, 2021).

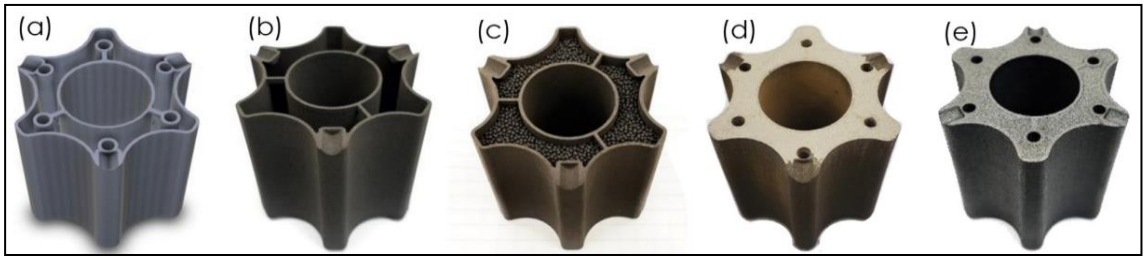

Figure 2-8: (a) CAD design on fuel element shell, (b) CAD design element shell printed with binder jet, (c) TRISO particles in fuel element shell, (d) SiC powder fills the interstitial spaces between particles, (e) Fuel element after CVI treatment (Terrani *et al*., 2021)

In Figure 2-8, it must be noted that the progression in production of two different elements is shown, where (a), (d), and (e) contain internal cooling channels, while those are absent in (b)

and (c). The final product is the FCM fuel with multiple inherent barriers to radionuclide release. The chemical vapour infiltration (CVI) process depends on their being open pores to progress, and the SiC matrix terminal density depends on the part's surface volume. As the open pores are closed, only the sealed outer surface continues to grow, but deeper in, the SiC matrix remains porous, as shown in Figure 2-9. This method can achieve as high as 92% theoretical densities for thin and optimal parts. The fully infiltrated element in Figure 2-8(e) has an average density of more than 85%, where the surface density starts from 100% to less as it decreases into thickness. The 3D-printed SiC matrix closely mimics the stoichiometry and structure of a CVD-manufactured SiC (Terrani *et al.*, 2021).

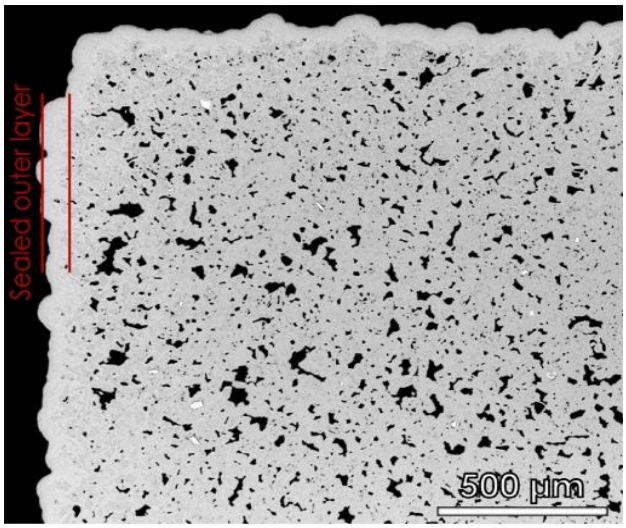

Figure 2-9: (In black) 3D printed SiC showing pores in the microstructure from an optimal image, (Slightly darker grey) is the original 3D printed powder and (Slightly lighter grey) the CVI matrix. Note: Growth of the outer SiC layer as the inner pores have sealed off (Terrani *et al*., 2021)

2.7.3 SiC material properties

We must discuss the material properties of the SiC material as they form the matrix and the particle layers most critical to containing fission products.

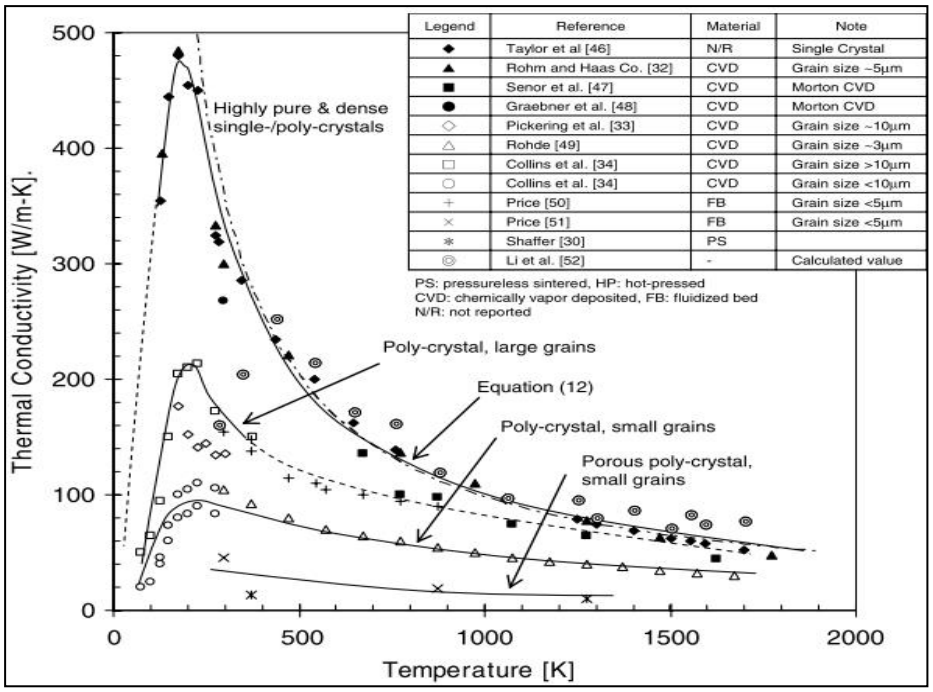

Figure 2-10:Thermal conductivity of SiC at elevated temperatures (Snead *et al.*, 2007)

Figure 2-10 shows the thermal conductivity of different fabricated SiC at elevated temperatures. The importance of Figure 2-10 comes from the grain size of the SiC, as Snead notes that thermal conductivity also depends on the nature of the grain boundaries. For example, a hot-pressed SiC shows poorer thermal conductivity. This can be attributed to sintering additives (considered impurities in the SiC form) having essentially lower thermal conductivity than the SiC material (Snead *et al.*, 2007).

2.7.4 Weibull characteristics strength

The effects of neutron irradiation on the strength of various SiC forms are essential to understanding how to simulate the fuel performance of the FCM fuel properly. Snead notes that the strength of the sintered SiC and reaction-bonded SiC forms exhibit strength deterioration in neutron irradiation (Snead *et al.*, 2007). Table 2-2 summarises the Weibull strength of CVD-SiC, which are essential material properties required later to simulate the performance of the FCM in LWR conditions. One of the shortcomings when using data from Snead's work is that an accurate description of how Weibull modulus trends with irradiation dose and temperature is not yet possible (Snead *et al.*, 2007).

Table 2-2:Summary of Weibull statistical strength of CVD-SiC Neutron (Snead *et al.*, 2007)

Strength test-Author	Neutron dose (dpa)	Irradiation temperature (K)	Weibull modulus	Weibull mean strength (MPa)	Weibull characteristic strength (MPa)	Number of tests
Flexure-Newton	Non-irradiated		9.6	433	450	25
	1.5-4.6	573	6.2	582	618	56
	1.5-4.6	773	5.5	541	578	55
	1.5-4.6	1073	8.7	567	592	34
Flexure-Kutoh	Non-irradiated		9.9	353	366	23
	6	573	5.5	433	463	10
	6	773	10.8	626	648	20
	7.7	1073	7.9	598	627	31
Internal Pressurisation-Byun	Non-irradiated		7.6	301	316	32
	1.9	1293	4.4	340	369	17
	4.2	1293	5.4	341	365	22
	4.2	1553	3.8	342	377	24

2.7.5 Summary

The manufacturing process for the SiC layer and SiC matrix is an important topic that needs to be explored to differentiate between the layer and matrix attributes in Section 2.7. Using the additive manufacturing higher packing fraction this is possible and allows us to assume that the diffusion coefficients for a SiC layer and SiC matrix manufactured from additive manufacturing are very similar.

2.8 STACY code

STACY is a code that comprehensively describes the fission product transport and release behaviour in an HTGR core (Verfondern *et al.*, 2014). The STACY code has been extended to simulate different scenarios and prismatic block for the HTR. These extensions allow for Fickean diffusion in cylindrical bodies and are resolved; fission product release calculations can be performed based on the fission product inventories from programs like SERPENT that can perform depletion calculations (Allelein *et al.*, 2016). STACY replaces the former codes FRESCO, PANAMA and SPATRA because of its higher precision than its predecessor (Kasselmann *et al.*, 2014).

Figure 2-11 shows the transportation model for fission products for TRISO fuel embedded in a matrix. $\dot{Q}_{tot}$ is the total formation rate of a fission product under consideration and $U_{CP,def}, U_{frac,Grains}, U_{frac,CP,int}, U_{CP,Bound}$ are respectively the amount of uranium in defective

coated particles, a fraction of total uranium in graphite, a fraction of total uranium in intact coated particles and a fraction of total uranium at grain boundaries. Figure 2-11 shows the overall process of calculating the amount of fission product released into the coolant (Xhonneux and Allelein, 2014).

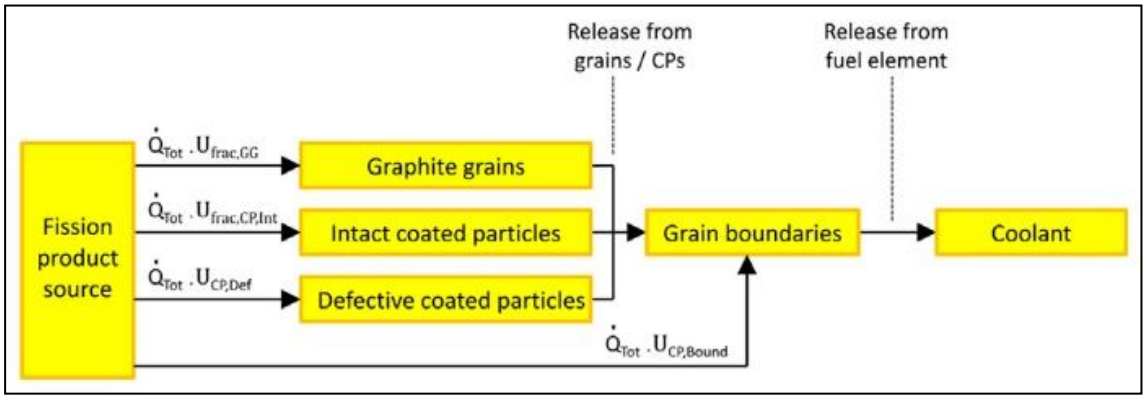

Figure 2-11:Transport model for fission product release calculation in STACY (Xhonneux and Allelein, 2014)

An important parameter needed as input in STACY, the standalone version, is FIMA. According to Kepisty (2007), "FIMA is defined as the percentage of heavy metal atoms that have been removed from the initial fuel compositions" (Kępisty and Cetnar, 2017).

$$FIMA = \frac{\Delta N_{HM}}{N_{0,HM}} = \frac{P\Delta t/\overline{E_{fiss}}}{N_{0,HM}} = BU\frac{\overline{M}}{\overline{E_{fiss}}} \qquad 2\text{-}16$$

Where: ΔN_{HM} is the number of heavy nuclei that fissioned, and $N_{0,HM}$ is the initial number of heavy-metal nuclei atoms shown in Equation 2-16. BU is the burnup and $\overline{M}$ is the weighted average molar mass of the total uranium mass composition in Equation 2-16. P is the thermal power in the system, and Δt is the time interval that the reactor runs and $\overline{E_{fiss}}$ is the energy deposited per fission of a single atom in Equation 2-16 (Kępisty and Cetnar, 2017).

2.9 Relevant fission products to track

Table 2-3 shows the isotopes that are important in safety analyses for an HTGR, and they are not limited to the HTGR but are also applicable to the PWR. For example, noble gases like xenon and krypton are products of fission. Those gaseous fission products are released into the free volume of the fuel rod, which increases the internal fuel rod gas pressure. In addition, the released gaseous fission products degrade the thermal conductance of the gas in the gap, causing higher fuel temperature, which acts as a burnup limiting factor because of pressure build-up and cladding tube integrity degradation (NEA, 2010).

Uranium, plutonium and other actinide products must be tracked as they are toxic to people and the environment in severe accident conditions (NEA, 2010). As for STACY, the code can only track caesium, strontium, silver and iodine in the FCM fuel, but this is for the standalone version (Xhonneux and Verfondern, 2016).

Table 2-3:Radiologically relevant fission products considered in HTGR safety analyses (Verfondern, 2012)

Fission Product	Half-Life	Relevance
^{131}I	8.021 days	Significant for design and licensing
^{133}I	20.81 hours	
^{134}Cs	2.066 years	Long-term behaviour after extreme accidents and in risk analyses
^{137}Cs	30.07 years	Long-term behaviour after extreme accidents and in risk analyses
^{90}Sr	28.78 years	Long-term behaviour after extreme accidents and in risk analyses
^{110m}Ag	249.8 days	Essential for maintenance in direct cycle plants despite the small quantity produced
^{111}Ag	7.454 days	Necessary for normal and accident conditions
^{85}Kr	10.783 years	Indicator of particle coating failure and conservative upper limit for iodine release
^{90}Kr	32.32 seconds	Precursor of ^{90}Sr
^{133}Xe	5.247 days	Necessary for normal and accident conditions
^{137}Xe	3.818 minutes	Precursor of ^{137}Cs
^{3}H	12.323 years	Important for waste management
^{14}C	5730 years	Important for waste management

2.10 Past experiments

This section discusses TRISO-based fuels and is used later to compare the performance of past experiments and the FCM fuel simulated in this paper.

2.10.1 OGL-1 experiment

The Japanese program conducted an irradiation experiment for the OGL-1, a high-temperature in-pile gas loop used for proving the irradiation performance of fuel elements regarding in-pile failure and fission product's behaviour in the fuel element (IAEA, 1997).

Table 2-4 shows the in-pile failure fractions for the TRISO particle in a fuel compact, and the Table 5-1 based on Table 2-4 compares the failure in coatings with the results from STACY in Chapter 5.

Table 2-4:In-pile failure of TRISO particles irradiated in OGL-1 (IAEA, 1997)

OGL-1	Compact name	Irradiation conditions			Failure fraction (Through coating)		Failure fraction (SiC coating)		EOL R/B (Kr-88)
		Time (EFPD)	Temperature ℃	%FIMA	BOL	EOL	BOL	EOL	EOL
10th	10109	130.2	1331	2.8	2.6×10^{-4}	6.6×10^{-4}	7.5×10^{-4}	1.2×10^{-3}	3.2×10^{-6}
15th	15116	218	1180	2.3	2.7×10^{-6}	3.7×10^{-8}	5.1×10^{-5}	-	3.8×10^{-7}

2.10.2 FRAJ2-P27 experiment

Table 2-5 comes from the post-irradiation examination from the German reference program in reactor performance. The FRAJ2-P27 was a research reactor in Juelich and was used to test the fuel performance of LEU TRISO particles.FRAL2-P27 had 3 capsules with each capsules containing 3 compacts with a total of 7272 coted particles plus 68 coated particles. For the first capsule half of the loose particles had a thicker SiC layer and the krypton release refers to a complete capsule while caesium refers a test on a single compact (IAEA, 1997). Table 2-5 is used for limited comparison with results obtained from the STACY program.

Table 2-5:Release of fission product (IAEA, 1997)

Compact name		Irradiation conditions			Release at the end of irradiation	
Time (EFPD)		Temperature ℃ (Surface/Center)	Fluence [E>0.18MeV]	%FIMA	Fractional release ^{137}Cs	EOL R/B ^{88}Kr
P27/1	232	880 / 1080	1.4	7.6	2×10^{-5}	2×10^{-6}
P27/2	232	1220 / 1320	1.7	8.0	1×10^{-4}	1×10^{-5}

2.10.3 FCM replacement fuel for LWRs Experiment

This experiment is different from the OGL-1 and the FRAJ2-P27 experiment because this one is based on simulation results.

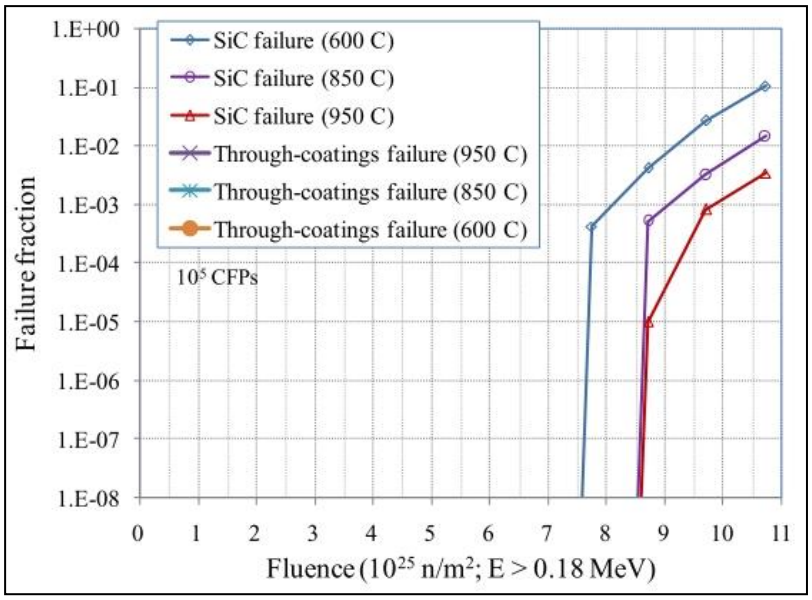

Figure 2-12:Variation of failure fraction of TRISO particle (Powers et al., 2013)

Figure 2-12 shows the predicted failure fraction of the TRISO particles in an LWR from Power's paper. Powers (2013) says that the failure fraction increases dramatically at $8 \times 10^{21} \frac{n}{cm^2}$ when using Weibull distributions for the PyC and SiC strengths. It is also stated that no failure occurs for 10^5 TRISO particles when the PyC and SiC failure strengths are given as 200 MPa and 400 MPa, respectively. From Figure 2-12 it is safe to assume that the through-coatings failure don't happen or are insignificant according to the author. The Weibull modulus in this experiment was six with a mean fracture strength of 400MPA. The code used for neutrons analysis was the DECART2D/MASTER developed by KAERI as full core neutron transport code while SERPENT was used for depletion calculations. The COPA code was used to evaluate the fuel performance of the FCM fuel (Powers *et al.*, 2013).

2.10.4 Safety design requirement

Establishing safety requirements is essential to evaluate the fuel performance of the FCM fuel. An essential design criterion is to minimise the failure fractions from manufacturing defects to reduce the overall failure fractions during normal operation. A design criterion used is that the fuel must have an overall failure fraction of the less than 2×10^{-3} for the entire lifetime. This assumption was taken from the Japanese HTTR (IAEA, 1997).

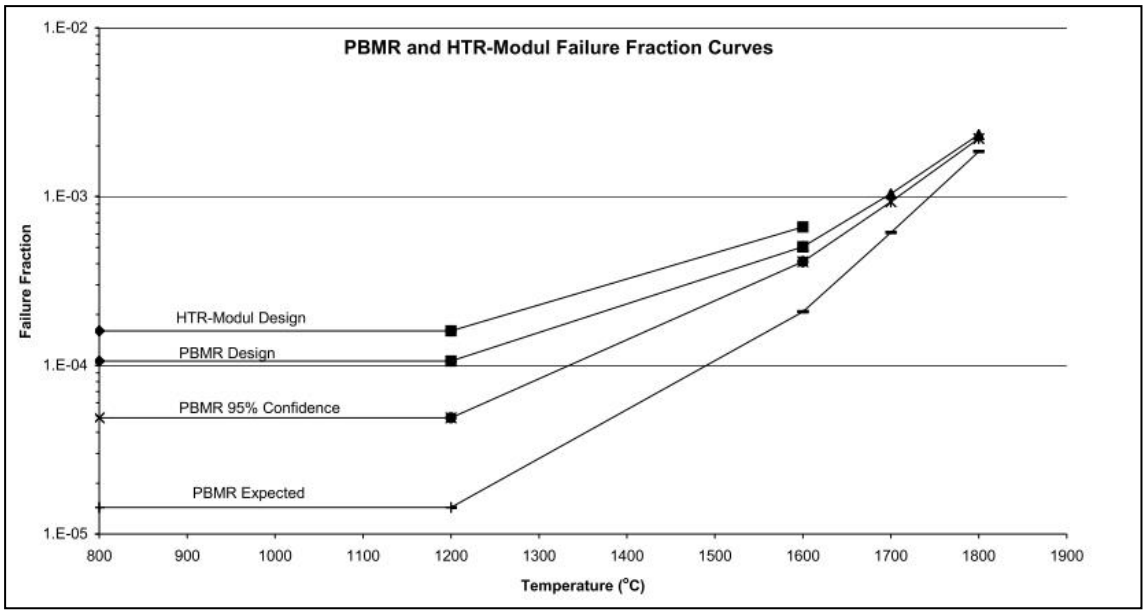

Figure 2-13:Trumpet curve (IAEA, 2010)

Figure 2-13 is based on the statistical evaluation of all German irradiations and heat-up testing of the KUFA tests performed at the Forschungszentrum Julich in Germany. Figure 2-13 shows that the failure fractions increase for temperatures above 1200℃ and is burnup dependent until the 1200℃.For the accident conditions happen above 1200℃ it seen that failure fraction are influeneced by higher temperatures (IAEA, 2010). The figure also shows the design value for failure fraction, which can also be used to evaluate whether the FCM fuel is reliable in LWR conditions.

Figure 2-13 is a conservative curve used to describe the general TRISO particle failure during irradiation until 1200 ℃ and the accident conditions for the HTR-Modul. From Figure 2-13 it seen that the failure fractions is 1×10^{-4} and 2×10^{-4} for the PBMR and HTR-Modul design respectively.The failure fraction for PBMR expected for manufactured induced defect fraction is 2×10^{-5} and that for the PBMR with 95% confidence manufacted defect it is 6×10^{-5} (IAEA, 2010).

2.11 Summary

The literature discussed the fuel failure mechanisms that can occur in FCM fuel and how the fission products are distributed in the FCM fuel. The fuel performance modelling approach used in STACY and other programs is discussed. The fission product of importance is discussed, and past experiments will be examined for limited comparisons. The Chernobyl accident will be used to determine the improvements brought about by the FCM fuel technology.

CHAPTER 3: RESEARCH METHODOLOGY

The research method is quantitative because software is used to simulate the neutronics and fuel performance of the fuel. To evaluate the neutronics and fuel performance, the programs SERPENT and STACY will be used for neutronics exploration and fuel performance evaluation. These codes have passed the Verification and Validation (V&V) process. SERPENT, in particular, has been used in multiple papers to verify results for newly developed codes, for example the deterministic code called MPACT (Gorton *et al.*, 2019). The STACY code is merged from FRESCO-I, FRESCO-II, PANAMA, and SPATRA to form one integral code, which has already gone through the Verification and Validation process (Xhonneux and Allelein, 2014). These codes will be used to simulate the fuel behaviour of FCM.

3.1 Analysis tools

3.1.1 SERPENT

For modelling the neutronic behaviour of the FCM fuel, a pin-cell analysis will be performed using SERPENT to track the burnup. SERPENT is a continuous-energy Monte Carlo particle transport code that can track the burnup and reactivity of a simulation model (Hakim *et al.*, 2019). SERPENT can determine the power peaking factor of a fuel assembly and perform depletion calculations. It is used for burnup and depletion for pin-cell, fuel assembly, and full-core models. The fuel pellets are the UO_2 fuel and the FCM fuel with randomly packed TRISO particles. SERPENT will be used to compare the neutron spectrum for UO_2 and the FCM fuel for different points in the cycle. This is important in understanding how spectrum softening/hardening differs for fuels. SERPENT can also allow us to measure the radial power distribution and understand assembly power peaking regarding FCM fuel (Hakim *et al.*, 2019).

3.1.2 STACY

STACY is a fuel performance code that predicts a complete reactor core's overall fission product release, but this is not for the standalone version (Xhonneux and Allelein, 2014). The standalone version only works for one pin at a time. STACY will be used to model the diffusive release of fission products in the FCM fuel. STACY can accurately account for the number of defective TRISO particles which are treated as bare kernels where when nuclides are released from the kernels they immediately enter the matrix graphite. STACY also allows the user to estimate the fission product released into the fuel cladding system. This way, the internal pressure within the system can be determined. A representative fuel pin analysis will also be done to determine the fuel performance of the FCM fuel in comparison to the UO_2 fuel currently

being used. This can be repeated for different positions and burn-up histories, including postulated accident conditions.

3.2 North Anna modelling reference

The primary reference for the North Anna model comes from analysing the PWR critical configurations report from the ORNL. The KENO V program is used for criticality calculations for North Anna 1 Cycle 5 BOC, which yielded a value for k_{eff} of 1.0040 ± 0.0005. The k_{eff} results are approximately 2% $\Delta k/k$ greater than those reported for the North Anna and North Anna reactor critical benchmark calculations performed with the original SCALE scoping calculations. The model used in the report was a full core model (Bowman and Suto, 1996).

The North Anna core consists of 157 Westinghouse fuel assemblies in a 17 x 17 lattice containing 264 fuel rods, which have 24 control rod guide tubes and one instrument tube. Critical conditions are based on the HZP start-up testing for BOC-5, where the critical boron concentration was 1836 ppm and the core components at 559 K are based on nominal HZP conditions. All control rods were in a fully withdrawn state. The top and bottom reflector is a 50:50 mixture of borated H_2O and stainless steel, approximately 25 cm thick (Bowman and Suto, 1996).

The North Anna safety analysis report from the US National Regulator Council (NRC) is also used as a reference to verify and validate the main information for the fuel assembly from the ORNL report. This is an essential step as the ORNL report assumes a uniform temperature for the UO_2 fuel while the safety report only provides the centreline temperature with the UO_2 thermal conductivity (NRC, 2016).

3.2.1 Reactor setup

Table 3-1 contains design parameters from the safety analysis report from the USA NRC safety report (NRC, 2016). The information in Table 3-1 has been processed and converted into units that SERPENT uses as input.

Table 3-1:North Anna Reactor Design Configuration (NRC, 2016)

Design Parameters	Numbers	Units
Thermal power	2775	MWth
Coolant temp inlet	559.15	K
Average temp rise	37	K
Average thermal output	17.84	kW/m
Peak temp centerline	2060.92	K
Pressure drop core	163.40	kPa
Nominal pressure	15.513	MPa
Active fuel height	364.998	cm
Number of fuel assemblies	157	
Fuel rods per assembly	264	
Lattice pitch	21.50364	cm
Pin pitch	1.25984	cm
Cladding radius	0.409575	cm
Cladding thickness	0.057	cm
Cladding material	Zircaloy-4	
Pellet radius	0.4095	cm
Guide tube inner diameter	1.143	cm
Guide tube outer diameter	1.22428	cm
Average velocity	4.60248	m/sec
Fuel density	10.31	g/cm^3
Boron concentration in coolant	1836	ppm

3.2.2 Pin cell

Material properties are important for simulation in SERPENT and are used for neutronics calculations. The material parameters important in SERPENT are the material density and elemental composition breakdown. Material properties can either be extracted from literature or SERPENT's built-in material properties library can be used.

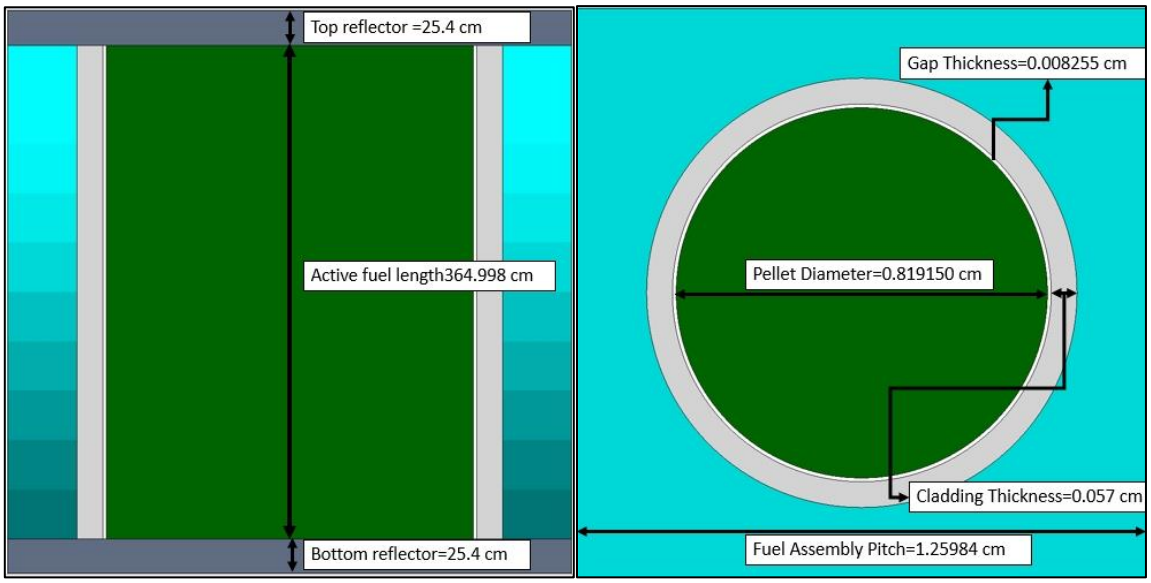

Figure 3-1:Pin cell dimensions (not to scale), (a)Side view of the pin, (b)Top view of the pin

Figure 3-1 depicts the dimensions of the pin in the SERPENT-generated image and is used to confirm whether the geometry in the SERPENT code is accurate for simulation. The figure uses the following colours for different materials:

- Fuel is green
- Water is in different shades of blue from Figure 3-1(a) side view, and the water has a boron concentration of 1836 ppm
- Zircaloy-4 cladding is light grey
- The mixture of water and steel is dark grey from Figure 3-1(a) side view

The boundary condition for the pin used in SERPENT is the reflective boundary for the x and y-axes, where the neutrons are reflected back into the geometry. The z-axis is applied with a black boundary where the neutrons escape the geometry (Lepp, 2011).

3.2.3 Fuel assembly

The boundary conditions for a fuel assembly are the same as those in the pin cell discussed in Section 3.2.2. The material properties of the pin and the fuel assembly are the same because the fuel assembly is composed of the pin cell with guide tubes in some areas.

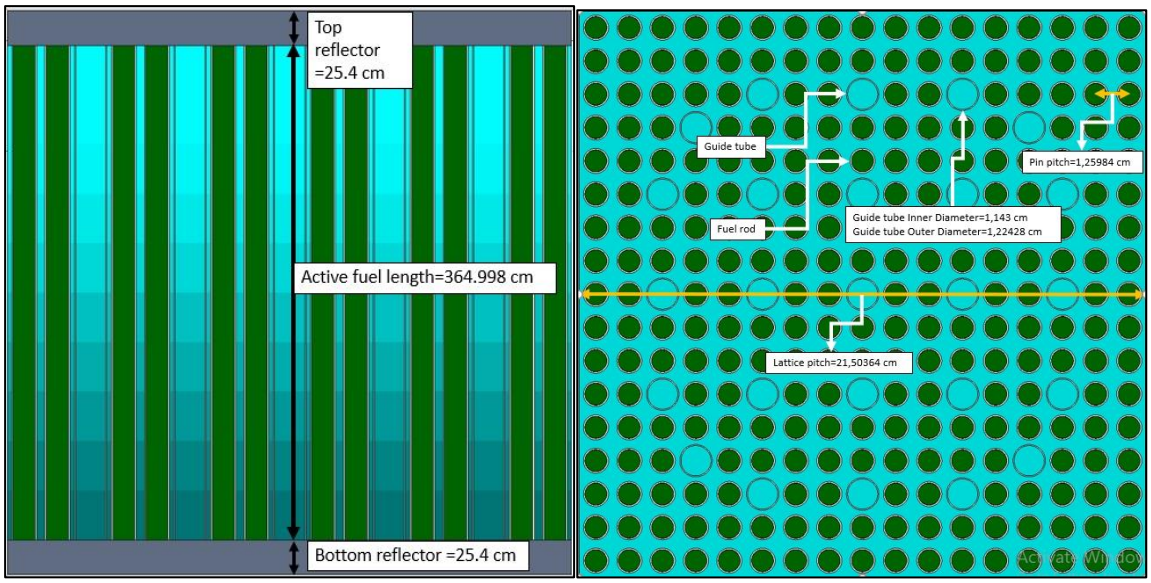

Figure 3-2:17 x 17 Fuel assembly (a) top view (b) side view

Figure 3-2 depicts the dimensions and labelling of different fuel assembly components from the SERPENT-generated image. Like Figure 3-1(a), where there are top and bottom reflectors, Figure 3-2(a) also contains the same reflector material.

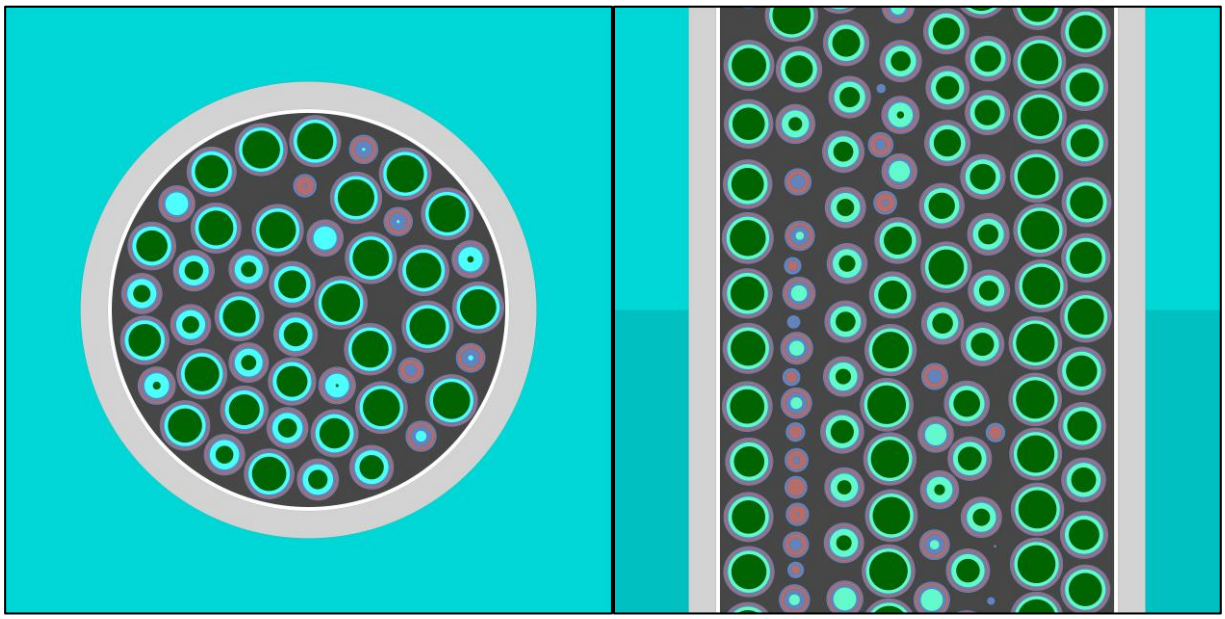

Figure 3-3:FCM fuel in the pin model (a) cross sectional top view (b) cross sectional side view

Figure 3-3 is the FCM fuel in the pin model, and the dimensions of the different components are the same as in Figure 3-1; thus, only the fuel is changed in the pin and fuel assembly model.

Figure 3-3 (b) is the cross-sectional view of 0.62992 cm by 0.62992 cm to be able to see properly the TRISO particles

Figure 3-3 uses the following colours for different materials:

- Fuel is green
- SiC matrix is dark grey
- IPyC and OPyC are purple
- The SiC layer is red
- Buffer layer is light blue (outside the pin model, the water is in a darker shade of blue than the buffer layer)

3.2.4 Fuel material compositions

This section will focus on the fuel composition calculation methodology in the BEAVRS manual.

The fuel compositions are based on calculation methodology from the BEAVRS document from MIT for benchmarking PWR. The benchmark is based on the depletion of two operational cycles of a commercial nuclear power plant and provides a detailed description of fuel assemblies, burnable absorbers, in-core fission detectors, core loading patterns, and numerous in-vessel components (Horelik *et al.*, 2017).

The example in BEAVRS uses detailed assembly loading. The actual core averaged enrichment for the first cycle for highly enriched bundles is $\chi_{235} = 3.1\%$, and the enrichment for ^{234}U is 0.8% per enrichment percentage of $\chi_{235} = 3.1\%$.This can be seen in Equation 3-1:

$$\boldsymbol{\chi_{234} = 0.008 \times \chi_{235}} \tag{3-1}$$

As for ^{238}U the rest of the total uranium mass in the initial fuel loading is calculated in Equation 3-2:

$$\boldsymbol{\chi_{238} = 100\% - \chi_{235} - \chi_{234}} \tag{3-2}$$

The atomic mass of uranium (M_u) is calculated using Equation 3-3 from the weight percentage of uranium isotopes and the isotropic masses from JANIS (from library ENDF-VII):

$$\boldsymbol{M_u = \frac{1}{\left[\frac{\chi_{234}}{M_{234}} + \frac{\chi_{235}}{M_{235}} + \frac{\chi_{238}}{M_{238}}\right]}} \tag{3-3}$$

The weight fraction of uranium and oxygen in UO_2 is calculated by Equations 3-4, and 3-5:

$$\omega_U = \frac{M_U}{M_U + 2 \times M_O} \tag{3-4}$$

$$\omega_O = 1 - \omega_U \quad (3\text{-}5)$$

The fuel density is calculated from the BEAVRS core average enriched, where the mass and volume are used to get the fuel density, as shown in Equation 3-6. The fuel density is assumed constant for fuel enrichment ranging from 0% to 20% for simplicity and convenience for simulation. The formula used in BEAVRS is Equation 3-6.

$$\rho_{fuel} = \frac{m_{fuel}}{V_{fuel} \times \omega_U} \quad (3\text{-}6)$$

To calculate the number of ^{235}U atoms per cubic centimetre, we use Equation 3-7:

$$N_{235U} = \frac{\rho_{235U} \times N_A}{M_{235U}} \quad (3\text{-}7)$$

To calculate the density of U and ^{235}U we use Equations 3-8 and 3-9:

$$\rho_U = \rho_{UO_2} \times \omega_U \quad (3\text{-}8)$$

$$\rho_{235U} = \chi_{235} \times \rho_U \quad (3\text{-}9)$$

To find the number of ^{235}U atoms, we first calculate uranium's atomic mass using Equation 3-3. Secondly, we calculate the percentage weight of uranium in UO_2 from Equation 3-4. Thirdly, the average density of the fuel ($10.31 \frac{g}{cm^3}$) is multiplied by the weight percentage of uranium to calculate the average density of uranium, as shown in Equation 3-8. The average density of uranium is used to calculate the atom density of ^{235}U using Equation 3-7 by calculating the density of ^{235}U using Equation 3-9. With the atom density, the number of ^{235}U atoms can be determined by multiplying the atom density by the volume occupied by the fuel (Lamarsh and Baratta, 2001).

3.2.4.1 Thermal conductivity of UO_2

The thermal conductivity of UO_2 is derived from the NRC safety analysis report, and the following equations are used to determine the thermal conductivity of UO_2 at 95% theoretical density (NRC, 2016):

$$K_{UO_2} = \frac{1}{11.8 + 0.023T} + 8.775 \times 10^{-13} T^3 \quad (3\text{-}10)$$

Where T is the temperature (in ℃), and K is thermal conductivity ($\frac{W}{cm-℃}$) in Equation 3-10.

3.2.5 Material composition for FCM

The material properties (specifically density and thermal conductivity) for the various TRISO layers were obtained from the literature. The material compositions of the various materials were taken from the SERPENT built-in material libraries. The dimensions used for the TRISO particle were taken from the Keun paper for the MMR reactor by the USNC (Keun *et al.*, 2014). It is important to note that the buffer, IPyC and OPyC layers are materially composed of carbon only, and their density is the only difference between them.

The parametric dimension for the particles in the FCM fuel used in the simulation is shown in Table 3-2, which is derived from Keun's paper.

Table 3-2:TRISO particle material properties used for simulation (Keun *et al*., 2014)

Parameters	Numbers	Units
Kernel radius	0.04	cm
Buffer layer thickness	0.007	cm
IPyC layer thickness	0.0035	cm
SiC layer thickness	0.0035	cm
OPyC layer thickness	0.0020	cm
Buffer layer density	1.0	g/cm^3
IPyC & OPyC layer density	1.9	g/cm^3
SiC layer & matrix density	3.2	g/cm^3
TRISO packing fraction	58%	-
Fuel enrichment	14.668%	-

Table 3-3 contains the thermal conductivity of the TRISO layers as they are used to calculate the temperature of the FCM pellets using the axial and radial temperature calculation methods discussed in Sections 3.3.2 and 3.3.3.

The thermal conductivity for SiC is extracted from Figure 2-10 for a lower thermal conductivity that is conservative and is derived from Wells' paper (Wells *et al.*, 2021).The NITE-SiC matrix contains less impurities than the CVD-SiC but their material properties are assumed to be same because of the lack of data on NITE-SiC material properties (Deng *et al.*, 2022).

Table 3-3:Thermal conductivities of the FCM fuel (Collin and Power, 2013)

Layer	Thermal conductivity (with T temperature (K))	Units
Buffer	0.5	W/m-K
IPyC & OPyC	4	W/m-K
SiC layer & matrix	$\frac{17885}{T} + 2$	W/m-K

Table 3-4 contains the tensile strength measurements of SiC specimens from the German

particle batch, EO 1607. These measurements are used in the STACY code as the SiC parameters for the SiC layer.

Table 3-4:SiC strength parameters used for simulation (Verfondern, 2012)

Parameter	Properties	Unit
Strength (σ_{00})	834	MPa
Modulus (m_{00})	8.02	-
Defective coatings fraction due to manufacturing	3×10^{-5}	-

3.2.5.1 The diffusion parameter for FCM layers

Table 3-5 and Table 3-6 list the effective diffusion coefficients used in STACY as parameters used for simulation. In Table 3-5 and Table 3-6, the diffusion coefficient of $D_{0,1}$ for the SiC pores and carbon buffer are the same. This is because the carbon buffer layer has a 50% porosity, meaning it has a weak fission product retention ability. It is assumed that the SiC pores diffusion coefficient should exhibit similar behaviour to the carbon buffer layer because the buffer has no retention ability.

Table 3-5 and Table 3-6 focus on those specific isotopes because STACY is only meant to track those four isotopes for the standalone version. The parameters in Table 3-5 and Table 3-6 are used in STACY to simulate the fuel performance in the FCM fuel.

Table 3-5:Diffusion coefficients of caesium and strontium

		$D_{0,1}$[m²/s]	Q_1[kJ/mol]	$D_{0,2}$[m²/s]	Q_2[kJ/mol]	Reference
Caesium	UO_2	5.6×10^{-8}	209	5.2×10^{-4}	362	(IAEA, 1997)
	Buffer	1×10^{-8}	–	–	–	(Collin *et al.*, 2016)
	IPyC &OPyC	6.3×10^{-8}	222	–	–	(IAEA, 1997)
	SiC grains & layer	$5.5 \times 10^{-14} e^{\frac{\Gamma}{5}}$	125	1.6×10^{-2}	514	(IAEA, 1997)
	SiC pores	$1 * 10^{-8}$	–	–	–	Assumption
Strontium	UO_2	2.2×10^{-3}	488	–	–	(IAEA, 1997)
	Buffer	1×10^{-8}	–	–	–	(Collin *et al.*, 2016)
	IPyC &OPyC	2.3×10^{-6}	197	–	–	(IAEA, 1997)
	SiC grains & layer	1.2×10^{-9}	205	1.8×10^{6}	791	(IAEA, 1997)
	SiC pores	1×10^{-8}	–	–	–	Assumption

Table 3-6 lists diffusion coefficients for silver and iodine. The diffusion coefficient for iodine is derived from the diffusion coefficient from krypton and xenon because they are all in the gas phase, and Collins confirms that they can be considered to have the same diffusion coefficient (Collin, 2016). An assumption is that the buffer and SiC pore diffusion coefficients are equal because SiC pores barely have a retention ability; thus, their properties are assumed to be the same as the buffer layer.

Table 3-6:Diffusion coefficient in silver and iodine

		$D_{0,1}$[m²/s]	Q_1[kJ/mol]	$D_{0,2}$[m²/s]	Q_2[kJ/mol]	Reference
Silver	UO_2	6.7×10^{-9}	165	–	–	(IAEA, 1997)
	Buffer	1×10^{-8}	–	–	–	(Collin *et al.*, 2016)
	IPyC &OPyC	5.3×10^{-9}	154	–	–	(IAEA, 1997)
	SiC grains & layer	3.6×10^{-9}	215	–	–	(IAEA, 1997)
	SiC pores	1×10^{-8}	–	–	–	Assumption
Iodine	UO_2	8.8×10^{-12}	54	6.0×10^{-1}	480	(IAEA, 2010)
	Buffer	10^{-8}	–	–	–	(IAEA, 2010)
	IPyC &OPyC	1.0×10^{-30}	–	–	–	(IAEA, 2010)
	SiC grains & layer	1.0×10^{-30}	–	–	–	(IAEA, 2010)
	SiC pores	10^{-8}	–	–	–	Assumption

3.2.5.2 Uranium contamination and defective manufacturing

Table 3-7 is based on two assumptions; firstly, the inventory contamination in the traditional graphite matrix is the same as in a SiC matrix, and secondly, the inventory fraction for the traditional graphite matrix is used for SiC pores and SiC grain.

Table 3-7:Uranium inventories outside the fuel kernel (Verfondern, 2012)

Uranium outside fuel kernel	Inventory fraction
U in buffer	1.0×10^{-3}
U in IPyC	1.0×10^{-4}
U in SiC	1.0×10^{-6}
U in OPyC	1.0×10^{-6}
U in SiC grains	1.0×10^{-7}
U in SiC pores	1.0×10^{-7}

3.2.6 Conclusion

Section 3.2 details the parameters used in SERPENT and STACY simulation to obtain the neutronic and fuel performance of the FCM fuel.

3.3 Thermohydraulic modelling for North Anna

This section discusses the axial and radial temperature distribution for the UO_2 fuel and FCM

fuel. For the FCM fuel it is assumed the fuel is a homogenised fuel with the thermal properties volume-weighted for the FCM fuel. It is assumed for the model that the coolant remains sub-cooled and that the heat source for the FCM fuel comes from the whole fuel. The extrapolated height used to calculate $\dot{q}'''_{max}$ in Equation 3-11 is 105% of the height of the fuel assembly. The height was discretised into 10 intervals for SERPENT where in each interval the temperature was homogenised. For STACY the average single temperature was used, because STACY only takes a single temperature. The units for all formulas used are SI units.

The axial pin temperature helps to define discretised axial temperatures that are used in SERPENT. The radial pin temperature is also calculated but this does not mean that SERPENT takes radial discretised temperature and STACY as well doesn't take radial discretised temperature. The purpose of the radial temperature is to avoid taking the centre and the surface temperature of the fuel and just taking of the average of the two temperatures. The radial pin temperature is used to provide a more accurate single average temperature as explained further in Section 3.3.5.1.

3.3.1.1 Why is the heat transfer coefficient important to calculate?

The fundamental reason why we need to calculate the heat transfer coefficient is that the definition of heat transfer coefficient basically tells us how efficiently heat is transferred between a fluid and a solid surface. It helps to predict the thermal behaviour of materials and thermal systems (Bergman *et al.*, 2007).Firstly, in this case it is important to understand the temperature distribution as it will help us to evaluate the UO_2 and FCM fuel thermal performance. Secondly, the FCM coated particles failure fraction is influenced by the fuel's temperature.

These thermal hydraulic calculations are done Microsoft Excel and iterative calculations are used to calculate pin temperature distribution for the axial and radial direction in a spreadsheet. The discretization of the temperature is also done in Microsoft Excel on a spreadsheet.

It is important to note that this temperature is assumed constant for all the burnup steps and not coupled between the neutronic and thermal hydraulics, the focus of the study is to couple the neutronics and fuel performance with the assumption of the temperature distribution.

3.3.2 Axial pin temperature distribution

In order to obtain the axial temperature distribution of the fuel pin, we use analytical solutions from Massoud to calculate the temperature distribution along the axial axis. The analysis is limited to PWRs where the coolant remains subcooled (Massoud, 2005).

Before we can find the temperature distribution, we must first find the volumetric heat generation rate $\dot{q}'''_{max}$ for the North Anna Reactor. To find $\dot{q}'''$ we use the formula below, which also assumes that the axial power profile along the fuel rod is cosine-shaped (Reihman, 1980):

$$\dot{q}'''_{max} = \frac{2\mathrm{P}_{\text{ave power per rod}}}{\mathrm{H}_{\text{extrapolated height of reactor}}\,\mathrm{D}_{\text{fuel}}^{2}\,\mathrm{sin}\left(\frac{\pi \mathrm{H}}{2\mathrm{H}_{\text{extrapolated height of reactor}}}\right)} \qquad 3\text{-}11$$

Where :

- $\mathrm{P}_{\text{ave power per rod}}$=The power per rod
- $\mathrm{H}_{\text{extrapolated height of reactor}}$ =105%of the height of the reactor
- D_{fuel} =The diameter of the UO_2 fuel pin
- H=the height of the fuel assembly

The fuel rod power axial volumetric heat generation profile is calculated using the Equation **3-12**:

$$q'''(z) = \dot{q}'''_{max}\,\cos\frac{\pi z}{H_e} \qquad 3\text{-}12$$

In Equation **3-12** H_e is the extrapolated height of the fuel rod, z is the location of the fuel reference to the point of reference. $q'''(z)$ is the volumetric heat generation at a specific point along the z-axis (parallel to height of fuel rod)

It is assumed that the coolant in the core remains subcooled, and this allows for the assumption that $dh = c_p dT$ where the pressure drop is negligible, and the coolant temperature calculated is for bulk coolant.

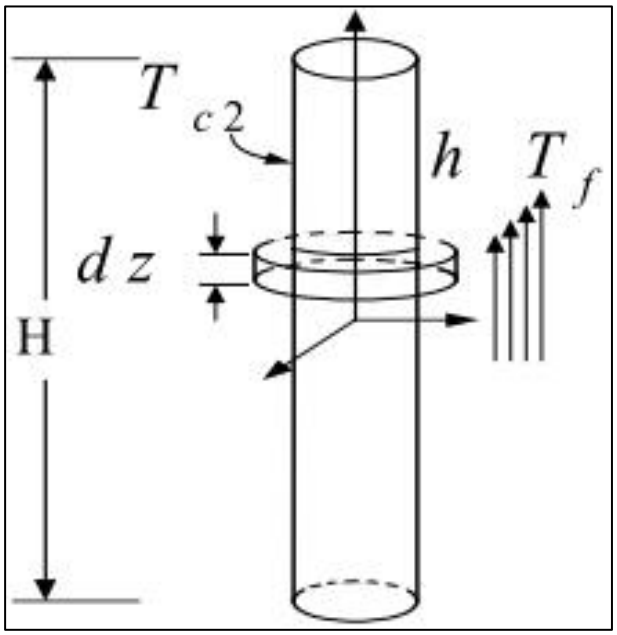

Figure 3-4:Schematic of coolant flow along fuel rod (Massoud, 2005)

In Figure 3-4 T_f is the coolant temperature ,T_{C2} is the outer cladding surface, h (and h_f) is the heat transfer coefficient of the coolant and H is the height of the fuel rod .Figure 3-4 shows the bulk coolant flow along the fuel rod, and we find that total heat generation is $\dot{m}c_p dT_f = d\dot{Q}$ where $\dot{Q} = \dot{q}'H = \dot{q}''\dot{P_{c2}}\,H = \dot{q}'''A_F\,H$ and that $P_{c2} = \pi d_{c2}$ and $A_F = \pi d_F^2/4$. Substituting $d\dot{Q}$ for $\dot{q}'''A_F\,dz$ in the total rate of heat generation, we get Equation 3-13 which is the energy rate balance (Massoud, 2005):

$$\dot{m}c_p dT_f = \dot{q}'''(Z)\,A_F\,dz \qquad 3\text{-}13$$

We now integrate Equation 3-14:

$$\int_{-H/2}^{z} \dot{m}c_p dT_f = \dot{q}'''_{max}A_F \int_{-H/2}^{z} \cos\left(\frac{\pi z}{H}\right) dz \qquad 3\text{-}14$$

Carrying out the integration and simplifying of Equation 3-14, we get the coolant temperature in Equation 3-15:

$$T_f(z) = T_{f,in} + \frac{\dot{q}'''_{max} \times \dot{A}_F \times H}{\pi \dot{m} c_p}\left[1 + sin\left(\frac{\pi z}{H}\right)\right] \qquad 3\text{-}15$$

This process can be repeated for coolant channels. For example, let's say we have the coolant

temperature. T_f is the temperature of the coolant and P_{c2} is the perimeter of the outer fuel cladding surface. We can then find the clad axial temperature distribution from the steady state heat balance using Equation 3-16.

$$d\dot{Q} = h_f(P_{c2}dz)\left(T_{c2} - T_f\right) \qquad 3\text{-}16$$

Substituting for the rate of heat transfer in Equation 3-13 and the fluid temperature of Equation 3-15 and using Equation 3-16 integrated form, we get the outer surface clad temperature as function of height along the z-axis in Equation 3-17:

$$T_{c2}(z) = T_{f,in} + \frac{\dot{q}'''_{max} \times V_F}{\pi \dot{m} c_p}\left[1 + sin\left(\frac{\pi z}{H}\right)\right] + \frac{\dot{q}'''_{max} \times A_F}{h_f P_{c2}}\left[cos\left(\frac{\pi z}{H}\right)\right] \qquad 3\text{-}17$$

In Equation 3-17, the heat transfer coefficient h remains constant from the inlet to any elevation.

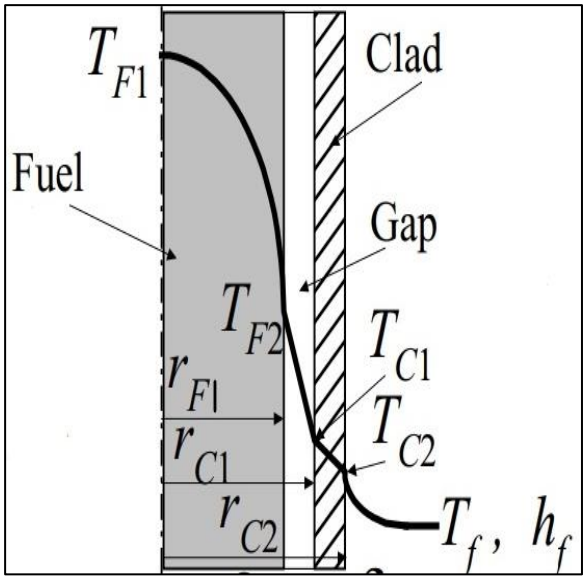

Figure 3-5:Temperature profile in a cylindrical fuel rod (Massoud, 2005)

Since the temperature outside of the cladding from Equation 3-17 is known, it is possible to find the temperatures for the inside of the cladding T_{c1} and the fuel surface temperature T_{F2} by using the corresponding thermal resistance from Equations 3-20 to 3-22; we should get a temperature profile for these two sections as shown in Figure 3-5, and their respective formulas are listed below; from Equations 3-18 to 3-19, we find the following (Massoud, 2005) :

$$T_{c1}(z) = T_{f,in} + \frac{\dot{q}'''_{max} \times V_F}{\pi \dot{m} c_p}\left[1 + sin\left(\frac{\pi z}{H}\right)\right] + \dot{q}'''_{max}\left[cos\left(\frac{\pi z}{H}\right)\right] \qquad 3\text{-}18$$

$$T_{F2}(z) = T_{f,in} + \frac{\dot{q}'''_{max} \times V_F}{\pi \dot{m} c_p}\left[1 + sin\left(\frac{\pi z}{H}\right)\right] + V_F\left(R_f + R_C + R_G\right)\dot{q}'''_{max}\ \left[cos\left(\frac{\pi z}{H}\right)\right] \qquad 3\text{-}19$$

Where the thermal resistance of gap (R_G), clad (R_C), and flow (R_f) are given below:

$$R_G = \frac{1}{2\pi r_{F1} L h_G} \quad 3\text{-}20$$

$$R_C = \frac{\ln \frac{r_{C2}}{r_{C1}}}{2\pi L k_C} \quad 3\text{-}21$$

$$R_f = \frac{1}{2\pi r_{C2} L h_f} \quad 3\text{-}22$$

3.3.3 Radial pin temperature distribution

The governing differential equation for the temperature distribution in the radial direction is given by the Equation 3-23 where $q'''(z)$ is the homogeneously distributed in the fuel compact and is treated as a constant for a particular volume along the z-axis:

$$\frac{d^2T}{dr^2} + \frac{1}{r}\frac{dT}{dr} + \frac{q'''(z)}{k_{fuel}} = 0 \quad 3\text{-}23$$

The boundary conditions for Equation 3-23 are the following:

$$T = T_{F2} \; at \; r = r_{F2} \quad 3\text{-}24$$

$$\frac{dT}{dr} = 0 \; at \; r = 0 \quad 3\text{-}25$$

The solution for Equation 3-23 is subject to the boundary conditions in Equations 3-23 and 3-24, and its final solution is shown in Equation 3-26 (Bergman *et al.*, 2007):

$$T(r)(\mathrm{z}) = T_{F2}(\mathrm{z}) + \frac{q'''(z)}{4k_{fuel}} r^2_{outer\ fuel}\left(1 - \frac{r^2}{r^2_{outer\ fuel}}\right) \quad 3\text{-}26$$

Equation 3-26 allows us to get the radial temperature distribution and is used to get the temperature at a ¼, ½, and ¾ radius from the centre. The temperatures profile is used for the average temperatures from the centre to ¼ of the fuel radius. Then ¼ to ½ radius until the outer fuel surface is reached. We get the following equation for ¼, ½ and ¾ radius (Bergman *et al.*, 2007):

$$T_{1/4}(\mathrm{z}) = T_{F2}(\mathrm{z}) + \frac{15q'''(z)D^2_{fuel}}{256k_{fuel}} \quad 3\text{-}27$$

$$T_{1/2}(\mathrm{z}) = T_{F2}(\mathrm{z}) + \frac{12q'''(z)D^2_{fuel}}{256k_{fuel}} \quad 3\text{-}28$$

$$T_{3/4}(\mathrm{z}) = T_{F2}(\mathrm{z}) + \frac{7\,q'''(z)D^2_{fuel}}{256k_{fuel}} \quad 3\text{-}29$$

From there, the average temperature of the fuel is estimated using discretized temperatures in the radial and axial temperature distribution as shown in section 3.3.5.

3.3.4 Heat transfer coefficient

3.3.4.1 Convection between coolant and cladding surface

To find the surface temperature of the fuel cladding T_{c2} as shown in Figure 3-5.Equation 3-17, the coolant heat transfer coefficient h_f is needed.To find h_f we need to calculate the equivalent diameter D_e for the coolant flow.

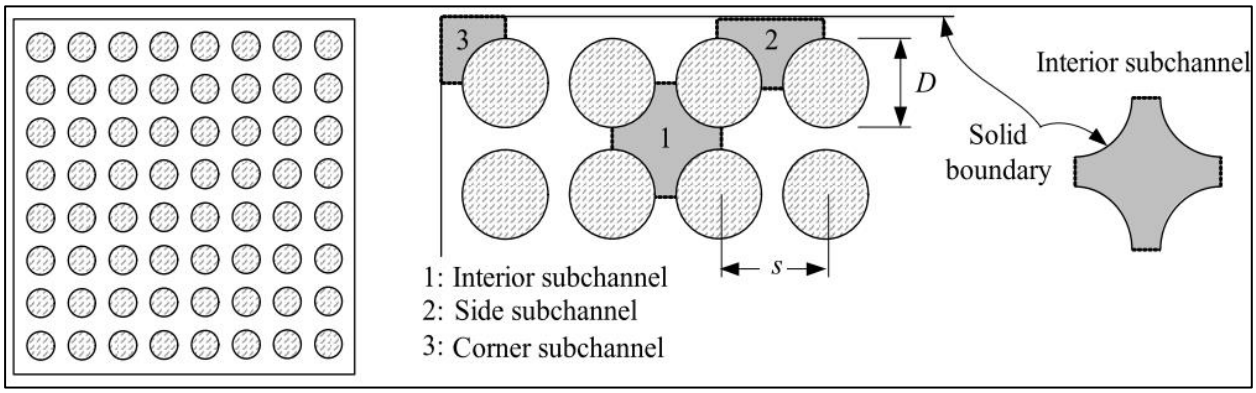

Figure 3-6:Hydraulic diameter for interior (1), side (2) and corner (3) subchannel for a fuel assembly (Massoud, 2005)

Figure 3-6 shows that in the interior subchannel (1), a control area is created, bounded by the gap between the fuel rods and surrounded by four fuel rods. The wetted perimeter consists of the rods wetted by the coolant of the interior subchannel (the four quadrants of the surrounding rods and the gap are imaginary, so it is not considered part of the wetted perimeter of the interior subchannel) (Massoud, 2005).

$$\mathrm{D_e} = \frac{2\left[\mathrm{s}^2 - \frac{\pi \mathrm{D}^2}{4}\right]}{\left[\left(\frac{\pi \mathrm{D}}{2} + \mathrm{s}\right)\right]} \qquad 3\text{-}30$$

$$= \frac{4\left[\mathrm{s}^2 - \frac{\pi \mathrm{D}^2}{4}\right]}{\pi \mathrm{D}} \qquad 3\text{-}31$$

$$= \frac{\left[\mathrm{s}^2 - \frac{\pi \mathrm{D}^2}{4}\right]}{\left[\left(\frac{\pi \mathrm{D}}{4} + \mathrm{s}\right)\right]} \qquad 3\text{-}32$$

The hydraulic diameter is essentially determined by $D_e = \frac{4A}{P}$, where A is the flow area of the subchannel of interest (like the interior subchannel solid boundary, as shown in Figure 3-6) and P is the wetted perimeter of the fuel rods where the interior subchannel is placed. Equations

3-30, 3-31, and 3-32 calculate the equivalent diameter of the side, interior and corner subchannels, respectively, where D is the diameter of the fuel rod and s is the horizontal or vertical distance between two fuel rods (Massoud, 2005).

Finding the heat transfer coefficient between the fuel rod and the coolant will require us to get the equivalent hydraulic diameter for the subchannel of interest and the Reynolds and Prandtl number for the coolant. From there, we get the Nusselt number and the heat transfer coefficient (Massoud, 2005).

First, we get the equivalent diameter for the interior subchannel using Equation 3-31. Secondly, we calculate the Reynolds number using Equation 3-33 (Massoud, 2005):

$$Re = \frac{\rho_f V_f D_e}{\mu_f} \quad 3\text{-}33$$

Where ρ_f is the coolant mean density in the reactor, V_f is the coolant mean velocity in the reactor and μ_f is the coolant mean kinematic viscosity. Thirdly to get the Nusselt number, we use Equation 3-34 (Massoud, 2005):

$$Nu_D = C\ Re_D^{0.8} Pr^n \quad 3\text{-}34$$

Where n=0.4. Because the coolant is being heated, the Prandtl number can be found in the thermodynamic table of properties for water, and C is a coefficient recommended by Weisman in relation to s and D, which are the pitch and diameter as shown in Figure 3-6. C is the coefficient for a square array in Equation 3-36 (Massoud, 2005):

$$C = 0.042\frac{s}{D} - 0.024\ where\ (1.1 \leq \frac{s}{D} \leq 1.3) \quad 3\text{-}35$$

Lastly, the Nusselt number is:

$$Nu = \frac{hD_{channel}}{k_{Water}} \quad 3\text{-}36$$

Where k_{water} is the thermal conductivity of water. By equalising Equations 3-34 and 3-36, we can make h the subject of the formula and find the heat transfer coefficient for the coolant. Thus the heat transfer is:

$$h = \frac{k_{water} Nu}{D_e} \quad 3\text{-}37$$

3.3.4.2 Gap heat transfer coefficient

The full safety analysis report(FSAR) is an environmental report and is a formal request to obtain operating license for the plant according to NRC standards. This usually done after all the construction and design details have already been worked out (Lamarsh and Baratta, 2001).The FSAR of North Anna provides a method for determining the heat transfer coefficient for the gas-filled gap in fuel. All it requires is to find the helium's thermal conductivity for the gas in question. The heat transfer coefficient can be calculated using the formula provided by the safety report in Equation 3-38 (NRC, 2016):

$$h_G = 1500k_G + \frac{4}{0.006 + 12\delta} \tag{3-38}$$

Equation 3-38 provides the heat transfer coefficient for the gas. The equation works with the British unit system (unit for thermal conductivity $\frac{Btu}{hr.ft.^{\circ}\mathrm{F}}$), where k_G is the thermal conductivity of the gas and δ is the gap width between the fuel pellet and the cladding. The gap heat transfer coefficient is used to calculate the thermal resistance in Equation 3-20 which in turn was used to determine the radial temperatures of the fuel pin.

3.3.5 Homogeneous temperature distribution for FCM fuel

The breakdown of Section 3.3.4.1 and 3.3.4.2 shows how the temperature distribution in the axial and radial direction can be calculated. In the case of the FCM fuel TRISO particles in the SiC matrix are randomly distributed. In order to determine the temperature distribution, it was assumed that the FCM fuel is a homogenous mixture of all the materials in the fuel. This reduces the complexity but also reduces the accuracy of the temperature distribution.

Sections 3.3.4.1 and 3.3.4.2 are therefore also used to calculate the temperature distribution in the FCM fuel but the difference is the thermal conductivity in the formulas change from k_{fuel} to $k_{FCM}^{homogeneous}$. The thermal conductivity is calculated by a simple volume weighting process in Equation 3-39

$$k_{FCM}^{homogeneous} = \sum_{n=1}^{6} k_n \left(\sum_{n=1}^{6} V_n \Big/ V_{total} \right) \tag{3-39}$$

In Equation 3-39 the summation from one to six represents the different layers that must be weighted. For one it is the kernel, two is the buffer, three is the IPyC layer, four is the SiC layer, five is the OPyC layer then lastly six is the SiC matrix.

The drawback of using this method is that the fuel temperature of the FCM fuel can be

underestimated and that assuming a constant temperature and density throughout the lifecycle of FCM fuel leads to less reliable results.

3.3.5.1 Discretization of axial and radial temperature

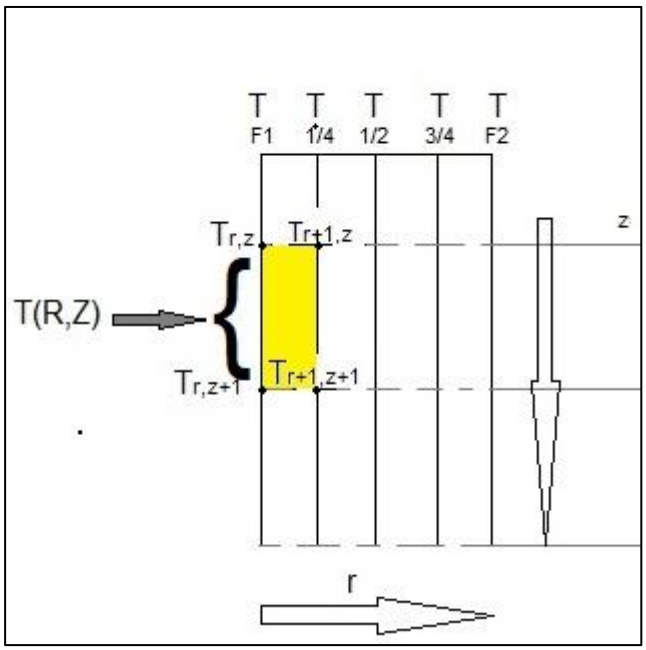

Figure 3-7:Fuel rod discretization

In order to define a temperature for a region of the fuel rod it is important to know discrete points temperature. This method is very similar to the nodal network approach of applying finite-difference for of heat equations. Figure 3-7 shows how four nodes will be used to calculate the average temperature a specific region. The difference is that the Equation 3-40 is used to define the temperature of a specific volume and not a nodal point temperature in a nodal network:

The axial length for the fuel pin was discretized into 10 equal lengths and the radial radius was discretized into 4 equal radiuses:

$$T_{FCM,}^{homogeneous}(\mathrm{R,Z}) = \frac{[T_{z,r} + T_{z,r+1}] + [T_{z+1,r} + T_{z+1,r+1}]}{4} \quad 3\text{-}40$$

$$T_{FCM,Volume-weighted}^{homogeneous}(\mathrm{Z}) = \sum_{\mathrm{R}=1}^{k} T_{FCM}^{homogeneous}(R,Z)\left(\sum_{\mathrm{R}=1}^{k} V_{R,Z} \Big/ V_{total}\right) \quad 3\text{-}41$$

$$T_{FCM,single\ whole\ temperature}^{homogeneous} = \sum_{\mathrm{Z}=1}^{m} T_{FCM,Volume-weighted}^{homogeneous}(\mathrm{Z})\left(\sum_{\mathrm{Z}=1}^{m} V_{R,Z} \Big/ V_{total}\right) \quad 3\text{-}42$$

Equation 3-42 is used to describe the single homogenous temperature a at a specified axial height and is the temperature used in SERPENT as the temperatures in the fuel rod in

SERPENT is sliced into 10 equal parts and with their own temperature. Equation 3-42 is the temperature used get a single homogenous fuel pin temperature which is used in STACY.

3.3.6 Thermodynamic material properties

The thermodynamic properties of water and helium for different temperatures and pressures were extracted from Fundamentals of Heat and mass transfer textbook (Bergman *et al.*, 2007). These values were taken to excel to create a spreadsheet and extract formulas from the numbers using excel formula function for graphs. These properties are used to simulate the system's temperature in SERPENT.

3.3.7 Verification

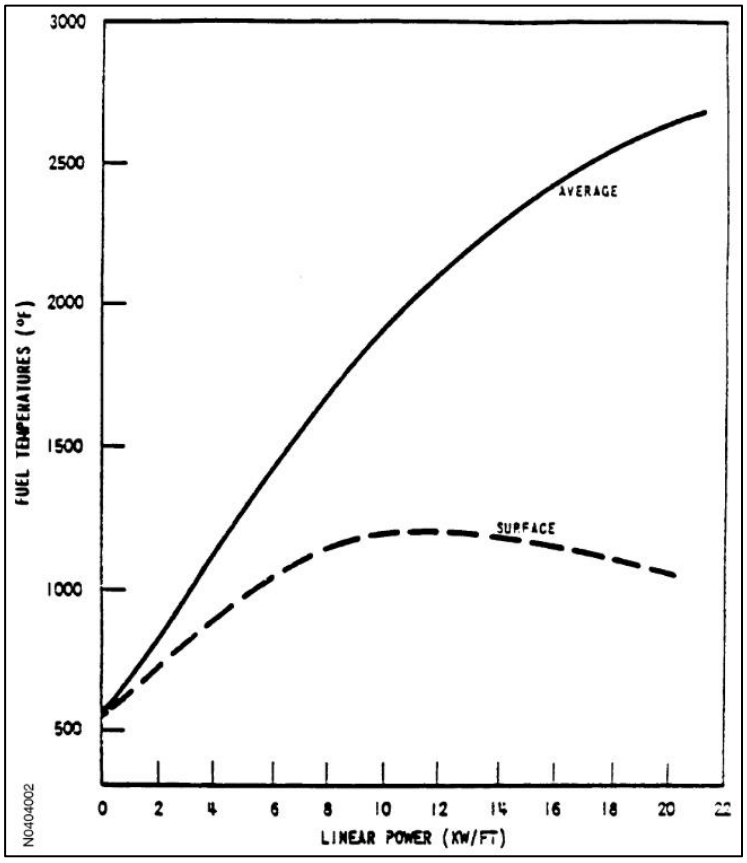

Figure 3-8:Fuel average and surface temperatures versus linear power for typical peak values during fuel rod lifetime (NRC, 2016)

In order to verify whether the method of calculating the average fuel temperature is correct, the temperature from our method discussed earlier is compared to the temperature in Figure 3-8 for the linear power our reactor is producing. The deviation between the calculated and figures' results is examined later in Table 3-10 and Table 3-11.

3.3.8 Conclusion

Section 3.3 details the methodology for calculating the temperature of the fuel and its components.

3.4 Verification and validation

An effective strategy to verify a fuel assembly model is to calculate the fuel volume in the SERPENT model and compare it with hand calculations of the fuel volume in assemblies. Similar processes are repeated to check all the inputs.

The study requires that we verify the data we get from SERPENT and STACY to trust the results produced. Previous irradiation experiments can be used to validate the reliability of the SERPENT and STACY. The limitation of experimental data is that the data gathered were based on high flux irradiation reactors, so we can only validate with available information. The case for the research is to compare the experimental data for the TRISO-coated particle and the simulation model developed using the STACY code. The experimental data that may be used is the PBMR fuel pebble bed project developed in South Africa. This can then be adapted to the PWR fuel in the Koeberg Nuclear Power Station that North-Anna represents (Mulasi, 2021). If these fuel performance data are unavailable, other data from the FRAJ2-P27 German irradiation experiment can be used for limited comparisons.

The validation work may also identify input data that is not available in the literature that needs to be clarified or measured. This will add value to identifying what measurements are required in future experimental programmes.

3.4.1 Verification

In this section we verify the calculations produced in SERPENT and manual calculations to make sure the geometries for the fuel assembly is correct.

3.4.1.1 Volume method

Table 3-8 shows the volume of the pin from the SERPENT-generated calculations and manual calculations based on the cylindrical calculations.

Table 3-8:Reference Pin volume calculations

Reference Pin	Manual Calculation	SERPENT Generated	Deviation
Fuel	192.356 cm^3	192.405 cm^3	0.025%
Cladding	58.344 cm^3	58.332 cm^3	0.021%

Table 3-9 shows the SERPENT-generated and manual calculations for different FCM fuel and cladding parts.

Table 3-9:FCM fuel volume calculations

	Manual Calculation	SERPENT Generated	Deviation
Fuel	39.256 cm^3	39.252 cm^3	0.010%
Buffer	24.426 cm^3	24.421 cm^3	0.020%
PyC	26.446 cm^3	26.453 cm^3	0.026%
SiC	17.589 cm^3	17.587 cm^3	0.015%
Matrix	84.637 cm^3	84.653 cm^3	0.019%
Cladding	58.344 cm^3	58.338 cm^3	0.011%

3.4.1.2 Fuel temperature

Table 3-10 compares the temperature from the safety report based on Figure 3-8 with the average fuel temperature from thermodynamics mathematical modelling.

Table 3-10: Average fuel temperature from thermodynamic modelling versus safety report (NRC, 2016)

Calculated (K)	Safety Report (K)	Deviation
929.424	912.836	1.817%

Table 3-11 compares the surface temperature from the safety report based on Figure 3-8 with the surface fuel temperature from thermodynamics mathematically modelling.

Table 3-11: Average surface fuel temperature from thermodynamic modelling versus safety report (NRC, 2016)

Calculated (K)	Safety Report (K)	Deviation
719.767	766.045	6.041%

3.4.1.3 Shannon entropy

The Shannon entropy is used to determine the convergence of the source distributions because statistical noise influences the results and there is a statistical uncertainty associated with the results for the number of active cycles. That is why it important to run a enough cycles free from contamination initial guess for fission distribution (Brown, 2006).

The Shannon entropy is used to validate the accuracy of the results produced from SERPENT for the simulation.

3.4.2 Validation

3.4.2.1 Full core reactor

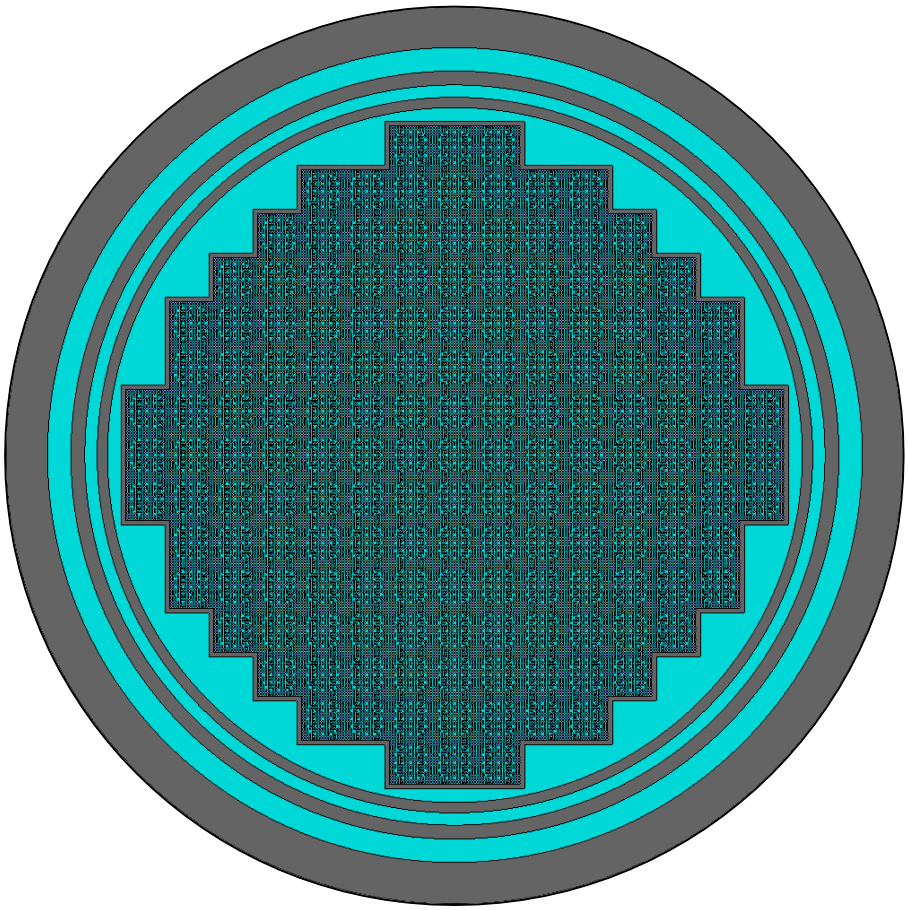

Figure 3-9:Full core used for validation

Figure 3-9 shows the full core of North Anna, which is used to compare the Idaho National Laboratory and SERPENT results. The material composition and temperatures are similar to the fuel assembly.

3.4.2.2 Results

Table 3-12 compares the reactivity stated in the ORNL analyses of PWR critical configurations for North Anna and the one calculated in SERPENT.

Table 3-12:Reactivity from safety report of full core reactor versus the reactivity in SERPENT full core (Bowman and Suto, 1996)

North Anna	Safety Report	SERPENT
k_{eff}	1.004	1.007
Reactivity (pcm)	398.406	724.709

3.4.3 Conclusion

When comparing the SERPENT model with the reactivity from the ORNL critical configuration report, we see that the reactivity from the report is almost half of what is produced from the safety report. This can be attributed to the fact that the k_{eff} of the safety report is based on SCALE calculations which are about 2% $\frac{\Delta k}{k}$ greater than those reported in the North Anna and the North Anna reactor critical benchmark calculations. The ENDF/B-IV and ENDF/B-V files used in the ORNL critical configuration using SCALE code (Bowman and Suto, 1996).

The fuel temperatures of the fuel rods calculated were in good agreement with the ones in the NRC safety report for North Anna. This indicates that the method for determining the temperature of the different components of the nuclear reactor was sufficiently accurate.

3.5 Simulation setup

This section lays out the process of simulating the fuel pins and assemblies. The process will entail how the simulation is done, the parameters of importance and the design constraints used for the models. The design constraint used in this simulation is regarding the number of ^{235}U atoms which must be the same in the UO_2 and FCM models for the simulations. Figure 2-6 depicts the way to convert the standard UO_2 fuel for the FCM fuel.

The simulations can be separated into two parts, one for the average fuel temperature from the pin model and two for the fuel temperature of the hottest pin in the fuel assembly.

3.5.1 Model breakdown structure:

1. The SERPENT code 2.1.31 is loaded onto the computer.
2. The pin and fuel assembly models were developed with their assigned material

properties, as shown in Sections 3.2.2 and 3.2.3.

3. The fuel enrichment of the FCM fuel was determined using methodology from Section 3.2.4 to ensure that the amount of ^{235}U is the same in the UO_2 and FCM fuel.
4. The moderator temperature was calculated using Section 3.3 methodology and the codes can be found in Sections 7.2.2 that were used in SERPENT.
5. The isotopes tracked are ^{235}U, ^{238}U, ^{239}Pu, ^{240}Pu, ^{131}I, ^{110m}Ag, ^{137}Cs, ^{90}Sr .
6. The burnup and cycle length are automatically measured by the SERPENT code when doing burnup calculations.
7. A random dispersion algorithm in SERPENT is used to randomize the TRISO particles in FCM fuel, and a packing fraction of 58% was chosen.
8. A surface detector in SERPENT is used to track the neutron flux on a fuel rod and the neutron spectrum in the pin and fuel assembly is measured for all burnup steps.
9. A detector that measures power is used to produce a power map for the fuel assemblies to extract the hottest pin, examine the neutron flux in order to recalculate the discretized axial temperature for SERPENT and which will be for the STACY input as an single average temperature of the fuel pin.
10. The SERPENT input codes can be found in the appendix under Section 7.2.

3.5.2 Flowchart process

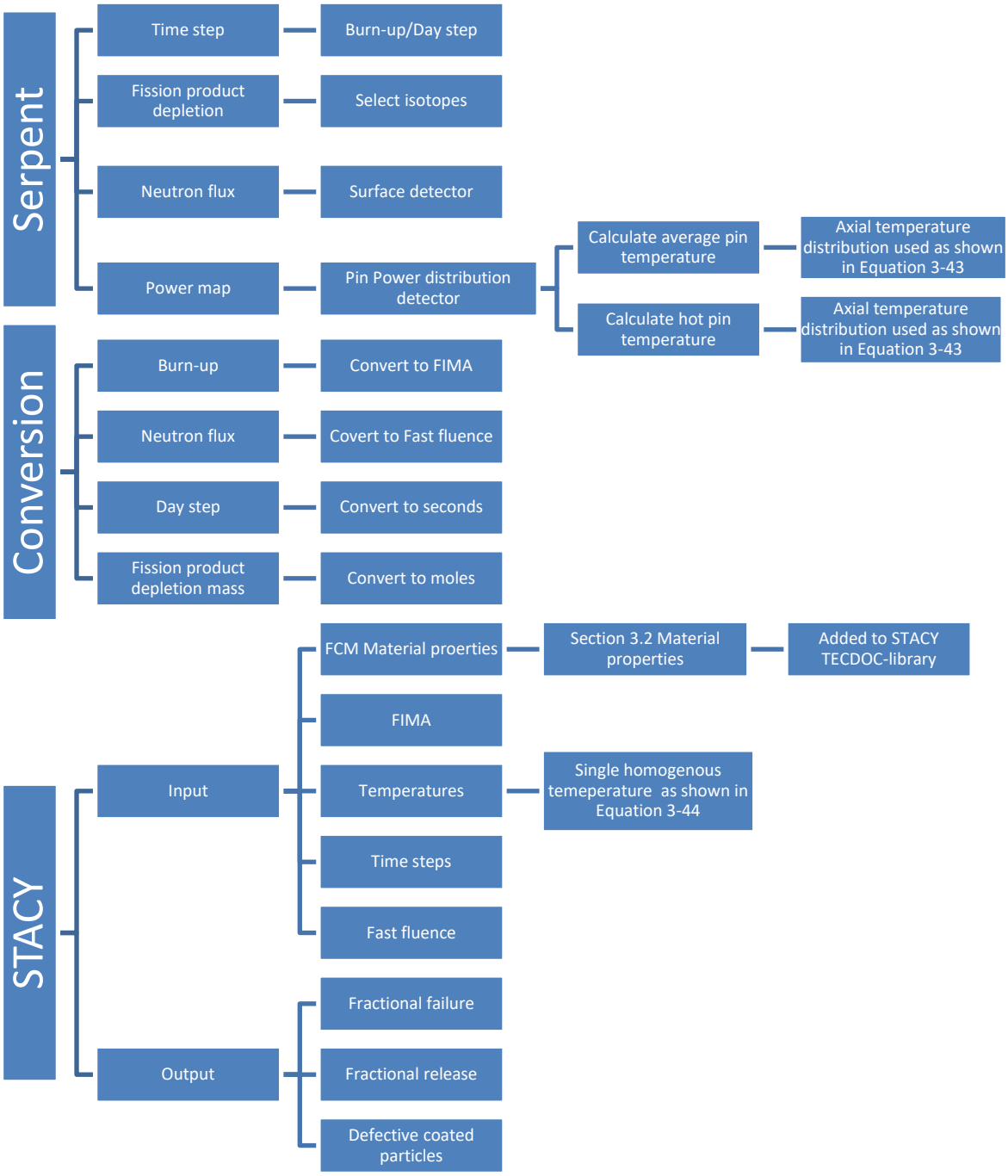

Figure 3-10:Basic flowchart of the simulation process

Figure 3-10 is a simplified version of what is being said in Sections 3.5.1 and Section 3.5.3.The figure shows a step for conversion, which entails converting in an excel spreadsheet or hand calculation.

3.5.3 Stacy code setup

1. The STACY standalone version examines one pin at a time
2. Some of the input for the STACY code comes from SERPENT, such as FIMA, burnup, neutron flux and cycle length.
3. The pin model in STACY uses a single temperature representing the whole fuel pin temperature.
4. The FIMA for the pin and fuel assembly can be calculated using Equation 2-16.
5. The fuel assembly is used to extract the highest power pin, and then we use Section 3.3 to recalculate the new temperature of that pin and apply the surface detector .
6. The neutron flux from SERPENT is converted to fast fluence and adjusted in the excel spreadsheet because the flux from the surface detector is integrated for the area.
7. The fast fluence for STACY was calculated for values greater than 0.1 MeV, meaning that the surface detector boundary for neutron energy must also be 0.1 MeV for SERPENT.
8. The results from STACY are tabulated in an excel spreadsheet for plotting.
9. The STACY input code can be found in Section 7.3.
10. The diffusion of coefficients are shown in Section 7.3.1
11. The nuclear data library used in SERPENT is ENDF-VII.

3.6 Summary

Chapter 3 discussed the analysis tools used for the North Anna specification in Section 3.2. The pin and assembly fuel are modelled using the North Anna specifications in Section 3.2. The temperatures of the different components were calculated using the method in Section 3.3. Section 3.4 inspects whether the model is correct and consists of hand calculations and the NRC safety report. Section 3.5 entails the steps and process to set up the model in SERPENT and STACY codes with their codes in the appendix in Section 7.For STACY only an one code was included as the others only vary with temperature and the nuclide being tracked.

CHAPTER 4 RESULTS AND DISCUSSION

4.1 Fuel rod temperature profile

The temperature profile helps to illustrate the temperature in the fuel rod for the UO_2 fuel and the FCM fuel for average power and highest power.

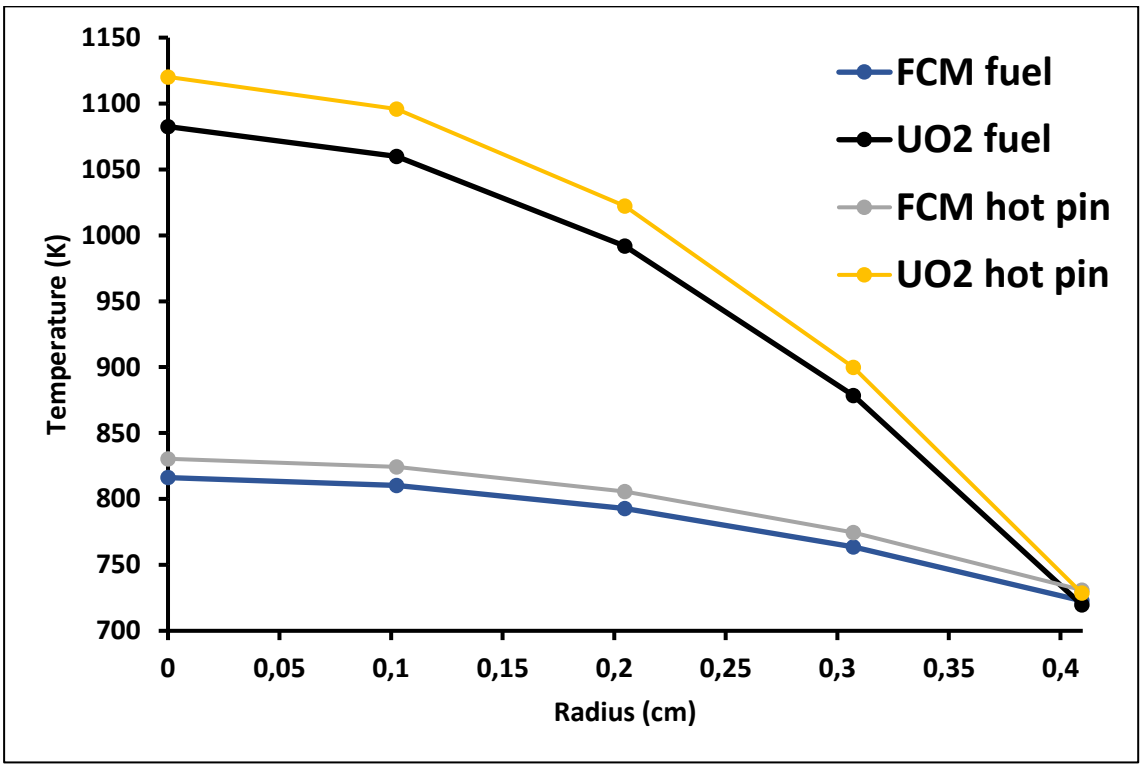

Figure 4-1:Temperature profile for the traditional UO_2 and FCM fuel

Figure 4-1 shows that the FCM fuel's thermal conductivity results in a lower fuel centreline temperature than the UO_2 fuel for both the average and hot pins. A lower fuel temperature centerline improves the reactor's safety overall, allowing more time to cool down and prevent fuel from melting.

4.2 Pin cell

In this section, we will discuss the results of SERPENT and STACY. This section examines the fuel and neutron spectra cycle length from the BOC, MOC and EOC.

4.2.1 Cycle length

This section compares the multiplication factor as a function of EFPD between the pin of UO_2 and the FCM fuel pellets for the same power, as shown in Figure 4-2.

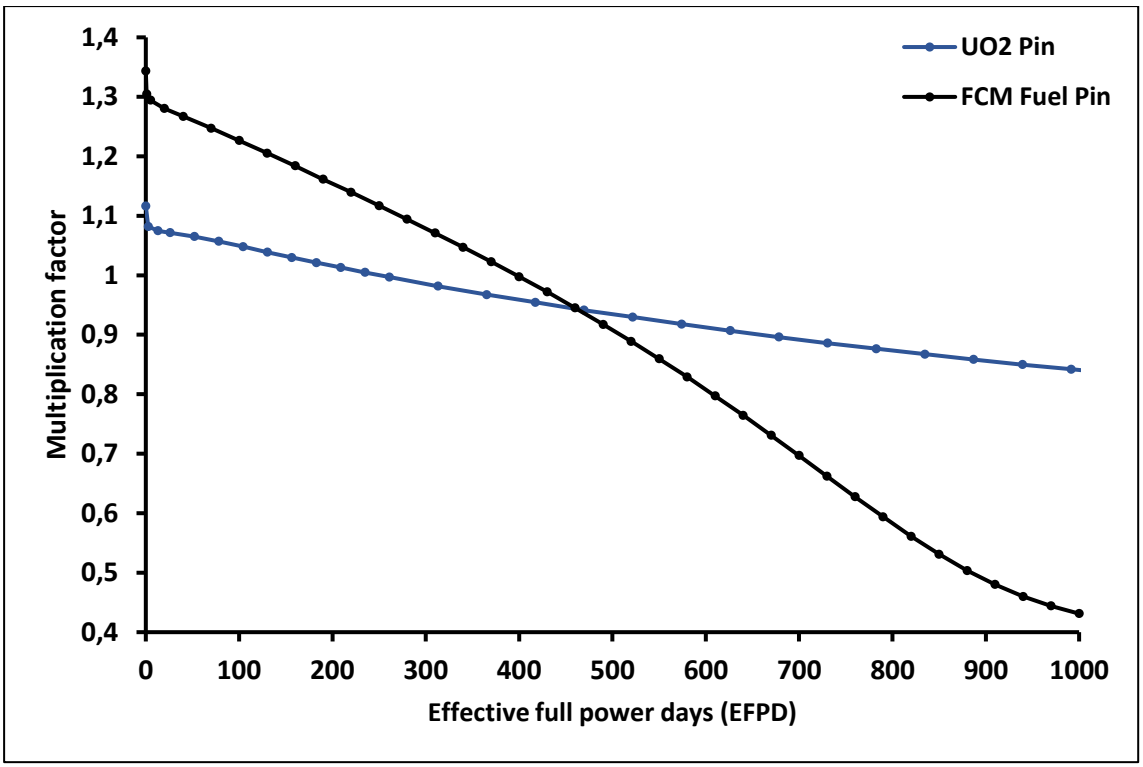

Figure 4-2:k_{eff} vs EFPD for UO_2 fuel and FCM fuel

Figure 4-2 shows that the FCM fuel has a higher reactivity at the BOC than the UO_2 fuel. The FCM fuel has a higher enrichment because of the lower uranium loading in the FCM than the UO_2 fuel. The design constraints regarding the same ^{235}U atoms in the FCM and UO_2 fuel imply that a higher enrichment is required in the FCM fuel to compensate for the lower total uranium mass loading. The UO_2 pellet fuel falls from super-critical to subcritical between 234 and 260 EFPD, while the FCM fuel is between 370 and 400 EFPD. The UO_2 and FCM fuel reactivity cross between 460 and 500 EFPD. This is because the ^{235}U is depleted quickly because of the better neutron spectrum of FCM fuel properties that allow for more thermalised neutrons and that plutonium plays less of a role in energy production. The UO_2 has a smoother gradient than the FCM fuel, which allows it to last longer as the number of EFPD increases because of the excessive production of plutonium compared to FCM fuel, as plutonium plays a role in energy production. That is why at the EOC, the reactivity of the UO_2 pellet fuel is higher than the FCM fuel. The maximum uncertainty for the results of the UO_2 pellet is 26 pcm, while for the FCM fuel it is 34 pcm.

The number ^{235}U between the two fuel designs remain the same but the ratio of $\frac{^{235}U}{^{238}U}$ increases which could contribute to an overall lower resonance absorption leading to a higher multiplication factor for the FCM fuel at the BOC. Lastly because the FCM fuel is in carbon and silicon based matrix they carbon is known to moderator which contributes to a softer neutron

spectrum.

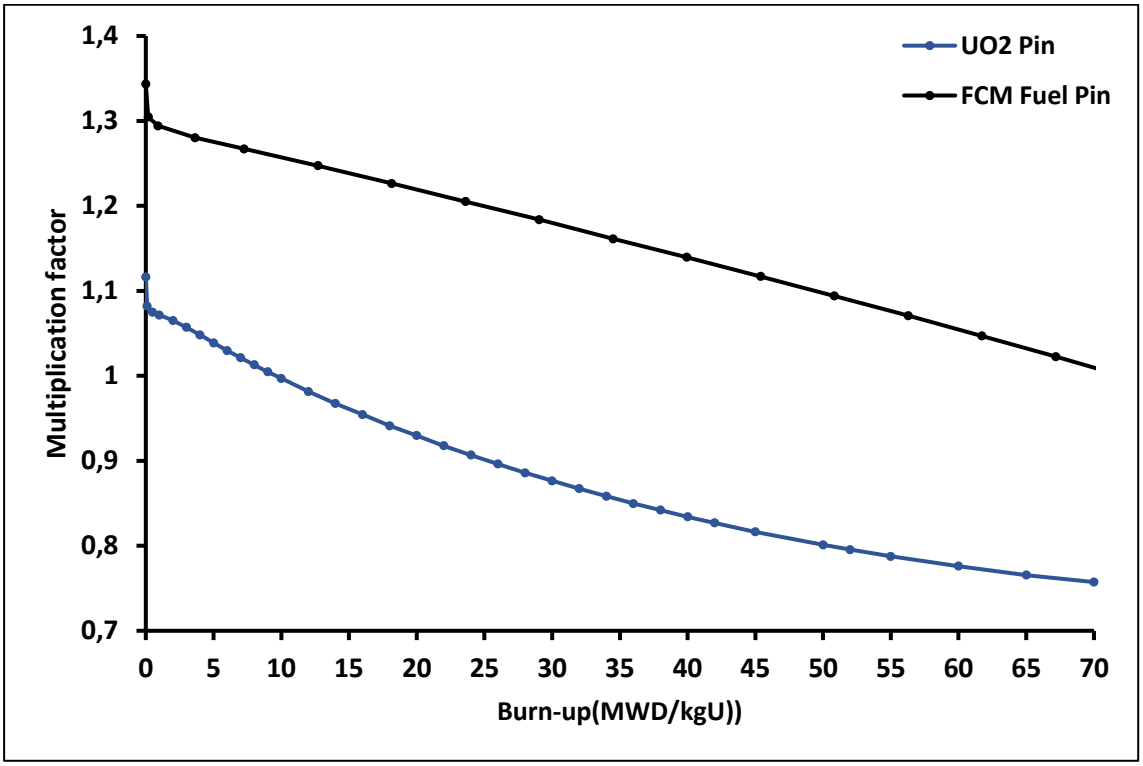

Figure 4-3: k_{eff} vs EFPD for UO_2 reference fuel and FCM fuel

Figure 4-3 shows that at the BOC, the reactivity of FCM fuel is higher than the UO_2 fuel pellet and remains higher than the UO_2 pellets until 70 MWD/kgU (EOC). At 70 MWD/kgU, it is about 370 to 400 EFPD, while for the UO_2 pellets fuel, it is at 1823 EFPD. This is first because of the lower total uranium mass loadings ($^{235}U+^{238}U$), and secondly, it tells us that with the FCM fuel, more power can be extracted from less total uranium mass loadings. This tells us that the efficiency of converting mass into energy is better in the FCM fuel than in the UO_2 pellet. The improved efficiency comes at the cost that increased enrichment in the FCM fuel is required to compensate for the lower total uranium mass loading. It should be bed noted that the results is limited because the FCM fuel would be optimally for one cycle use but there is a lack of understanding when used for more than one cycle.

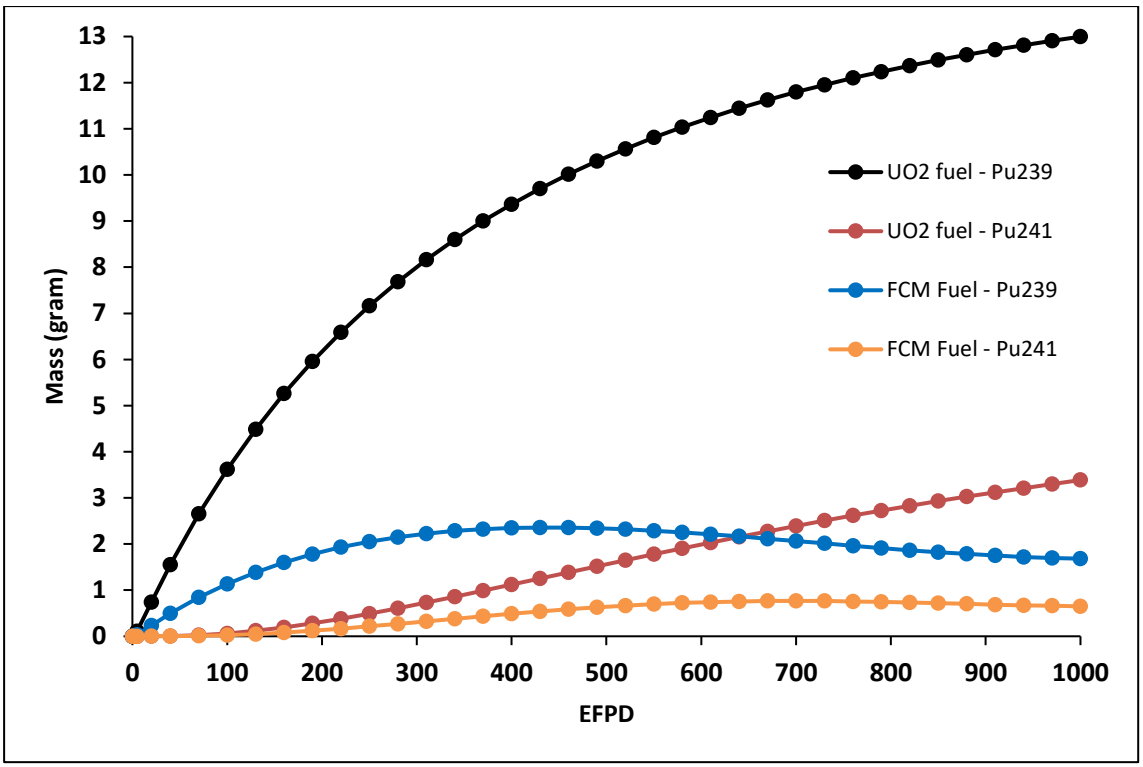

Figure 4-4:Plutonium build-up during irradiation of UO_2 fuel and FCM fuel

Figure 4-4 depicts the build-up of plutonium in the pin models. It is seen from Figure 4-4 that in the UO_2 fuel, there is more production of plutonium than in the FCM fuel. Plutonium's rapid build-up is responsible for energy contribution in an LWR during the late stages of a cycle (Massih, 2006). Plutonium is produced from the capture in ^{238}U. ^{239}Pu production is more prevalent in the UO_2 fuel than in the FCM fuel because of the self-shielding effects in both fuels. The neutron spectrum shift closer to the resonance and fast energies as burnup increases in the fuel. The spatial self-shielding that lowers the flux in the centre of the fuel is dominant in the UO_2 fuel as there is a layer that acts as a thin wall UO_2 fuel.

The fact that the enrichment between the two fuels differ in terms of U^{235}/U^{238} and because the FCM fuel has a higher enrichment the production of plutonium is lowered and the decreased U^{238} effects the overall resonance absorption since U^{235} is very fission ready fuel while U^{238} is not.

4.2.2 Neutron spectrum

This section will examine and elaborate on the phenomenon observed from the neutron spectrum of the UO_2 pin and FCM fuel.

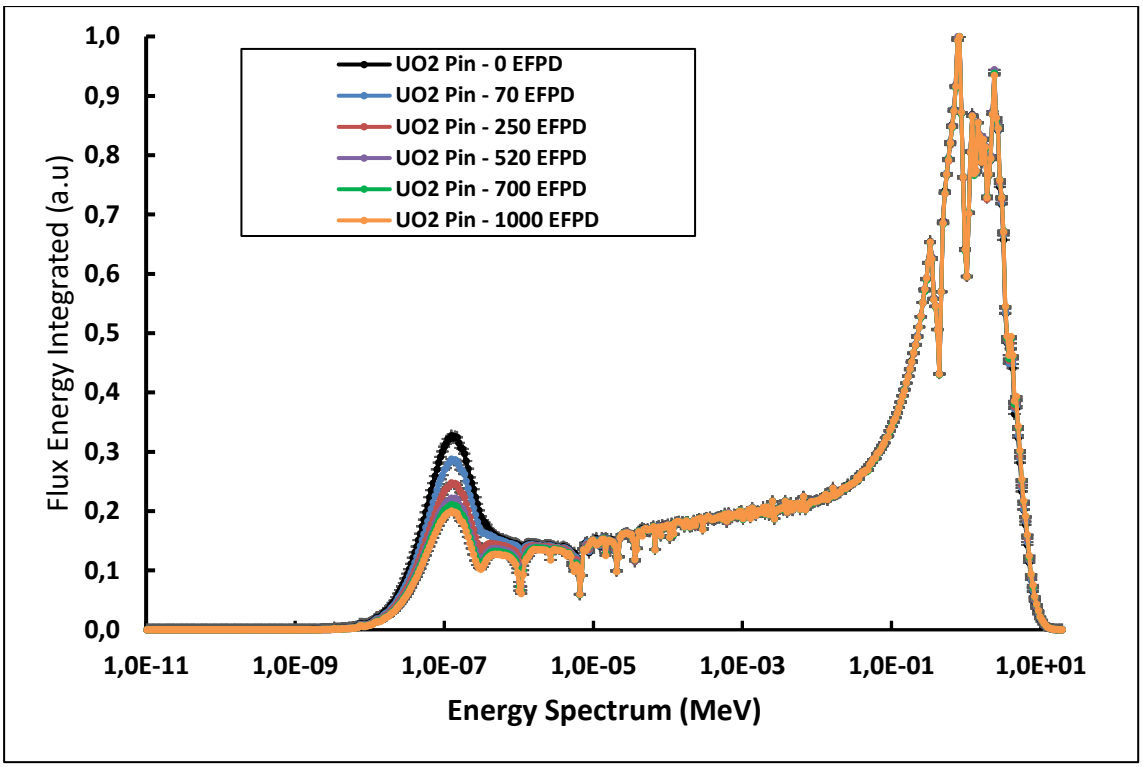

Figure 4-5:Neutron spectrum of UO_2 pin at different EFPD days

Figure 4-5 depicts the neutron spectrum for the UO_2 pin at different EFPD days, precisely at 0, 70, 250, 520, 700 and 1000 EFPD. From Figure 4-5, the neutron spectrum at the beginning of the cycle has the most thermal neutrons. As the number of EFPD increases, the neutron spectrum hardens, meaning fewer thermal neutrons are available.

The hardening of the neutron spectrum shifts the energy spectrum towards the resonance region. In the resonance region, there is an increase in the neutron absorption probability. A neutron has energy near the resonance region, but this reduces the effective absorption per nucleus due to the depression of the energy-dependent flux near the resonance region. At the energy below the resonance region where the absorption cross section becomes small, the neutron flux reaches almost the same value above the resonance. This phenomenon in energy-dependent neutron flux near the resonance energy is known as the energy self-shielding (Lamarsh and Baratta, 2001).

Neutrons are born in the fuel and are moderated in the moderator. These thermal and epithermal neutrons return to the fuel to cause further fission, but with energy self-shielding, the neutrons are absorbed by nuclei near the fuel surface. The surface layers of the fuel geometrically shield the inner layers from the neutron flux leading to a lower neutron flux inside the fuel rod (Lamarsh and Baratta, 2001).

The energy self-shielding and spatial self-shielding help explain the production of plutonium from captures. The increase in neutron capture happens because of the energy and spatial self-shielding effect. As the neutron spectrum hardens, the neutron energy shifts to near the resonance region of ^{238}U and then the fast region where capture is prevalent in ^{238}U, before decreasing as the energies increase further. The hardening of the spectrum means more plutonium is produced from capture in ^{238}U, and the ^{239}Pu fast fissions can contribute to one third of the energy production in typical LWR reactors.

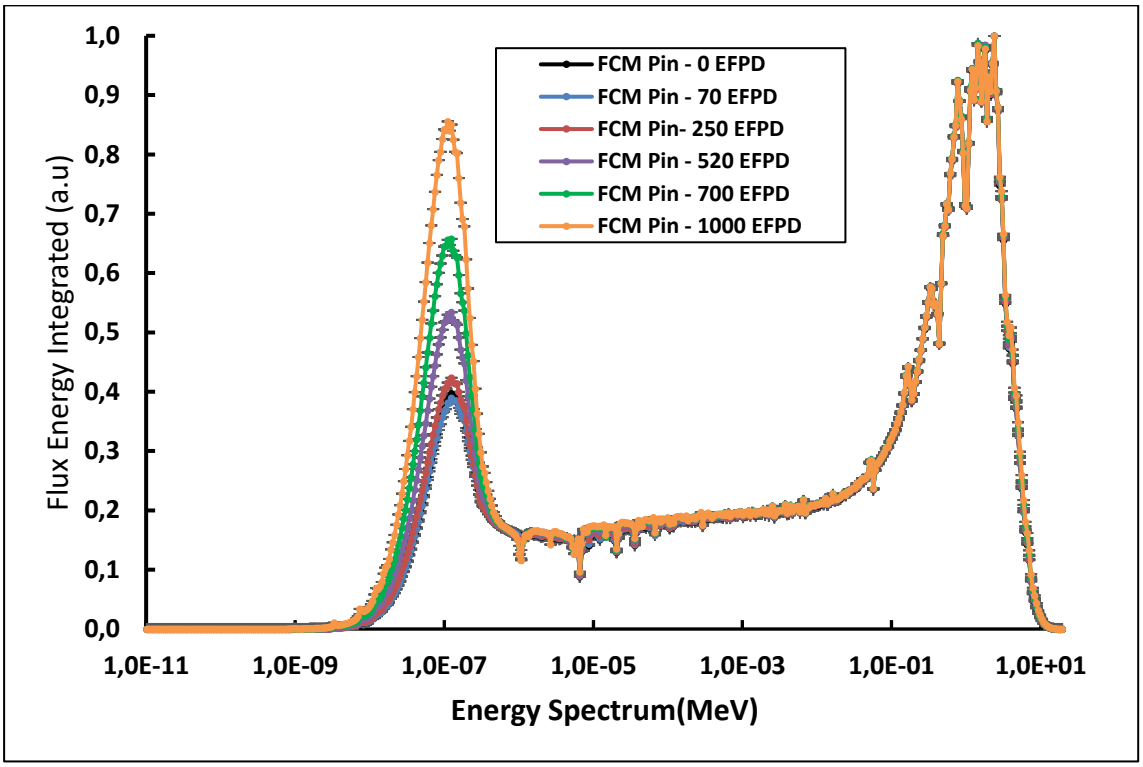

Figure 4-6 Neutron spectrum of FCM fuel pin at different EFPD days

Figure 4-6 depicts the neutron spectrum for the FCM pin at different EFPD days, precisely at 0, 70, 250, 520, 700 and 1000 EFPD. From Figure 4-6, the neutron spectrum at the beginning of the cycle has the least thermal neutrons. As the number of EFPD increases, the neutron spectrum softens, meaning more thermal neutrons are available.

However, the softening of the spectrum as the EFPD increases leads to low plutonium production because in the UO_2 fuel the neutron spectrum hardens, shifting the neutron energies near away from the resonance region rather than the fast region where capture in ^{238}U takes place. At the same time, the FCM fuel moves away from the resonance region to the thermalised region.

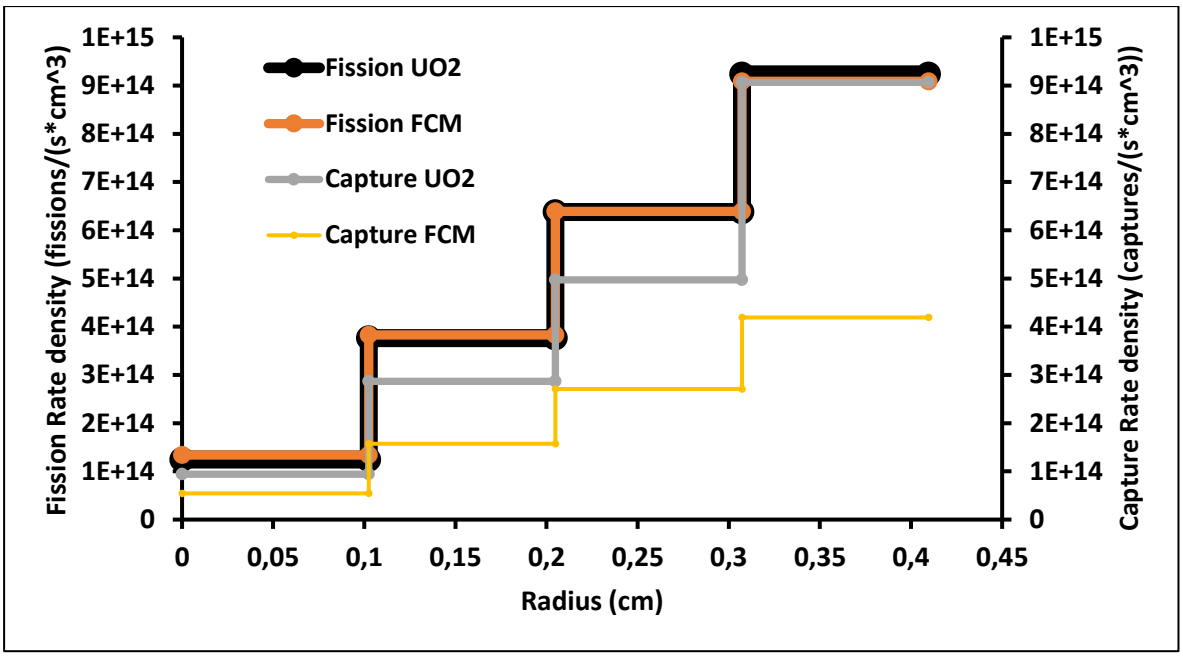

Figure 4-7:Fission and capture rate density for the UO_2 and FCM fuel

Figure 4-7 shows the radial fuel pin's fission and capture rate density. The fuel pin is divided into four rings of 0.102394 cm radius. We see that the fission rate density for the UO_2 and FCM fuels behave in remarkably similar fashions. The capture rate density for the FCM fuel is much lower than for the UO_2 fuel. We see that for the UO_2 fuel the outer layers where the capture predominately happens before a sharp decrease when moving towards the centre of the fuel for the first interval of the outer fuel layer, while in the FCM fuel, the sharp decrease is more evenly along the intervals. This means that the spatial self-shielding is predominantly in the UO_2 fuel. This helps to explain why the spatial self-shielding in the FCM fuel is lower, which lowers the production of plutonium, as seen in Figure 4-4.

4.2.3 Fractional releases and failure fractions of TRISO particles

This section will examine the failure fraction and the effects of the fractional release.

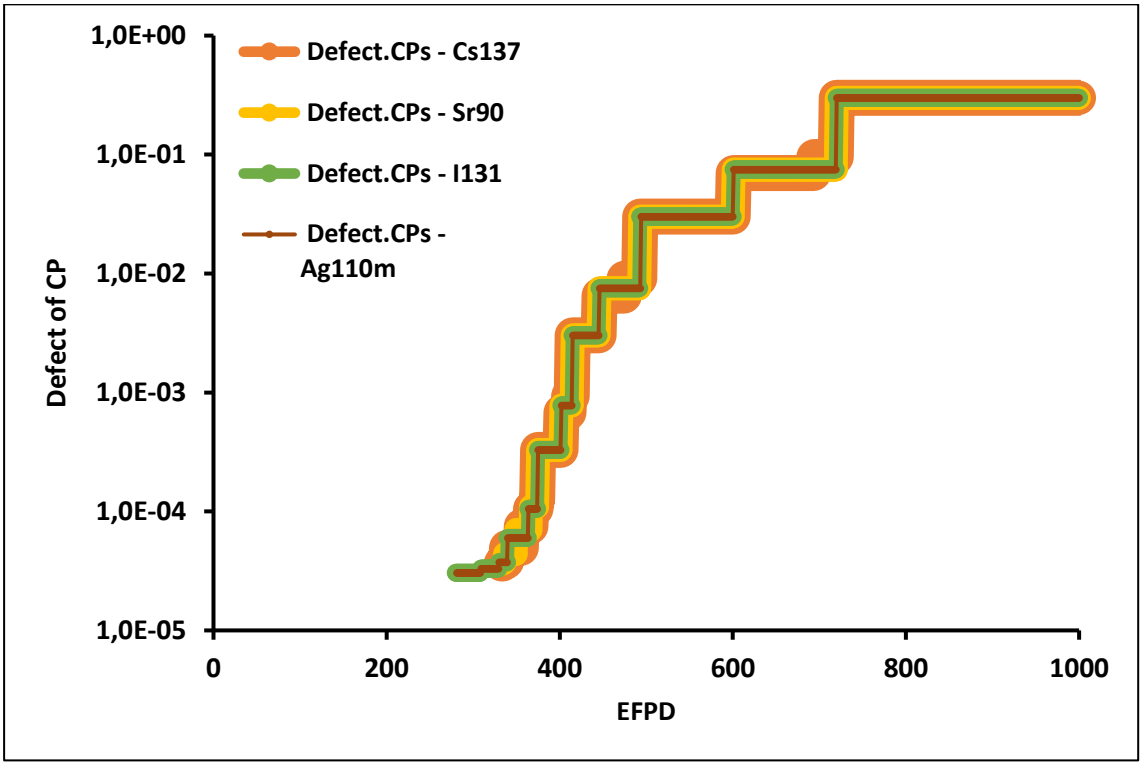

Figure 4-8:Failure fraction of TRISO particles

Figure 4-8 shows that the fraction of failed TRISO particles starts between the 250 and 280 EFPD marks. It is seen that ^{110m}Ag causes the TRISO layers to fail earlier than the other isotopes in Figure 4-8. Figure 4-8 focus on the number of TRISO that become defective as the EFPD increases and the nuclides show that as soon as a TRISO layer fails there isn't much of a difference in release behaviour from the coated particle layer failure. The layers don't necessary fail simultaneously either.

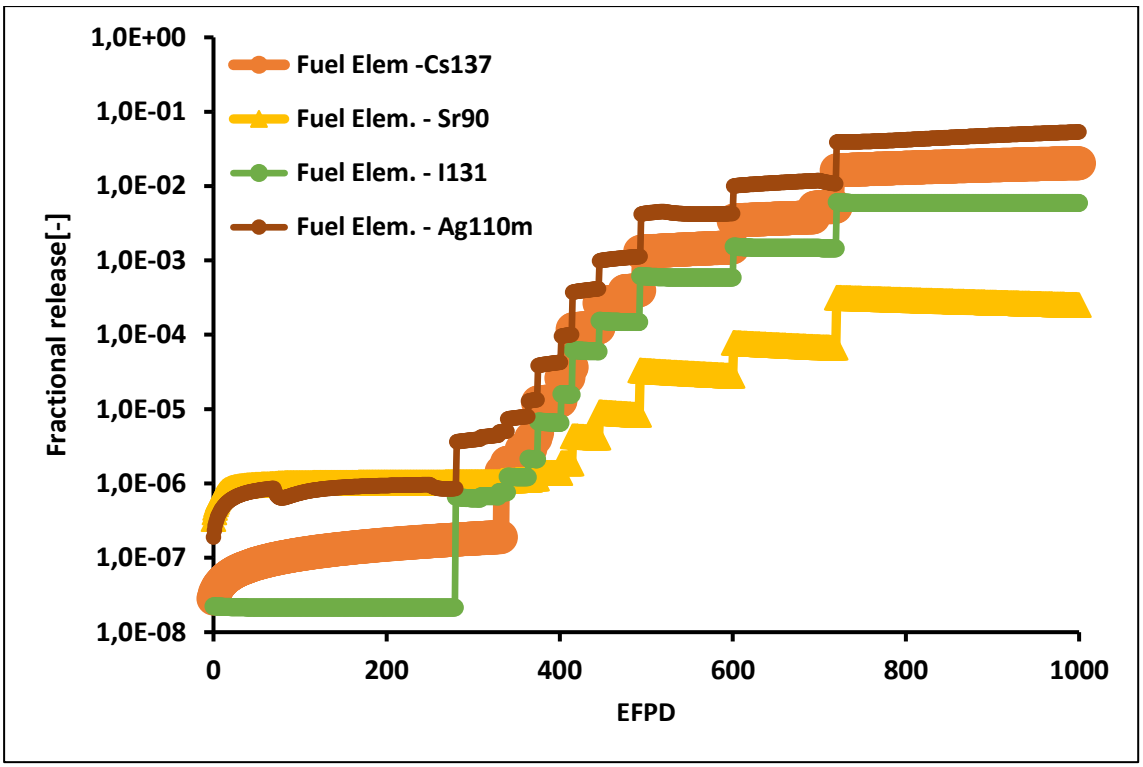

Figure 4-9:Fractional release of isotopes outside the FCM fuel

Figure 4-9 shows the fractional releases that reach the outside of the FCM fuel, and we see from EFPD 250 and 280 that there is an increase in the fractional releases in different fission product isotopes that correspond to the failure fraction of Figure 4-8 around the 250 and 280 EFPD marks.

4.2.4 Conclusion

This section showed us that more energy could be produced from less total uranium mass loadings than the UO_2 fuel pin. The section shows us that the cycle length of the FCM fuel is also shorter than the UO_2 fuel because of lower plutonium production. The section showed how both fuels' neutron spectrum differ in softening and hardening. The section also examined how self-shielding affects both fuels and how they differ. The section also examined fractional releases and how failure fraction increases the fission product's overall release.

4.3 Fuel assembly

This section analyses the cycle length of the fuel assembly and presents a power map used to analyse the neutron spectrum and fractional releases of the hottest fuel pin.

4.3.1 Power map

This section examines the power distribution to extract and isolate the hottest pin to examine the fuel performance.

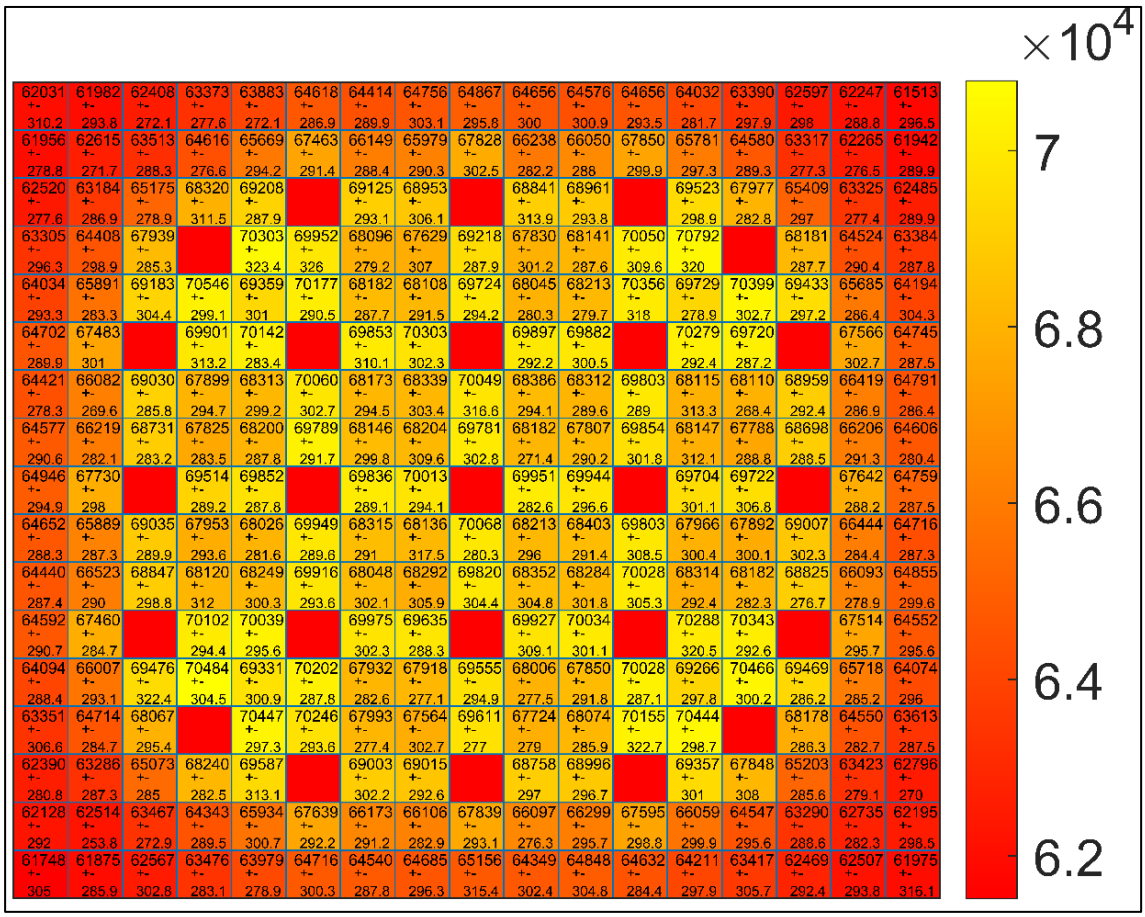

Figure 4-10:Pin power distribution in the UO_2 fuel assembly in Watts

The power map in Figure 4-10 shows the fission power in each fuel rod of the UO_2 fuel assembly with its power uncertainty. The power map shows that the maximum fission energy released into the system is 70,792 watts, while the minimum energy released is 61,513 watts. The power peaking in the fuel assembly is $p = \frac{Hottest\ rod\ power}{average\ rod\ power} = \frac{70{,}792}{66{,}951} = 1.057$

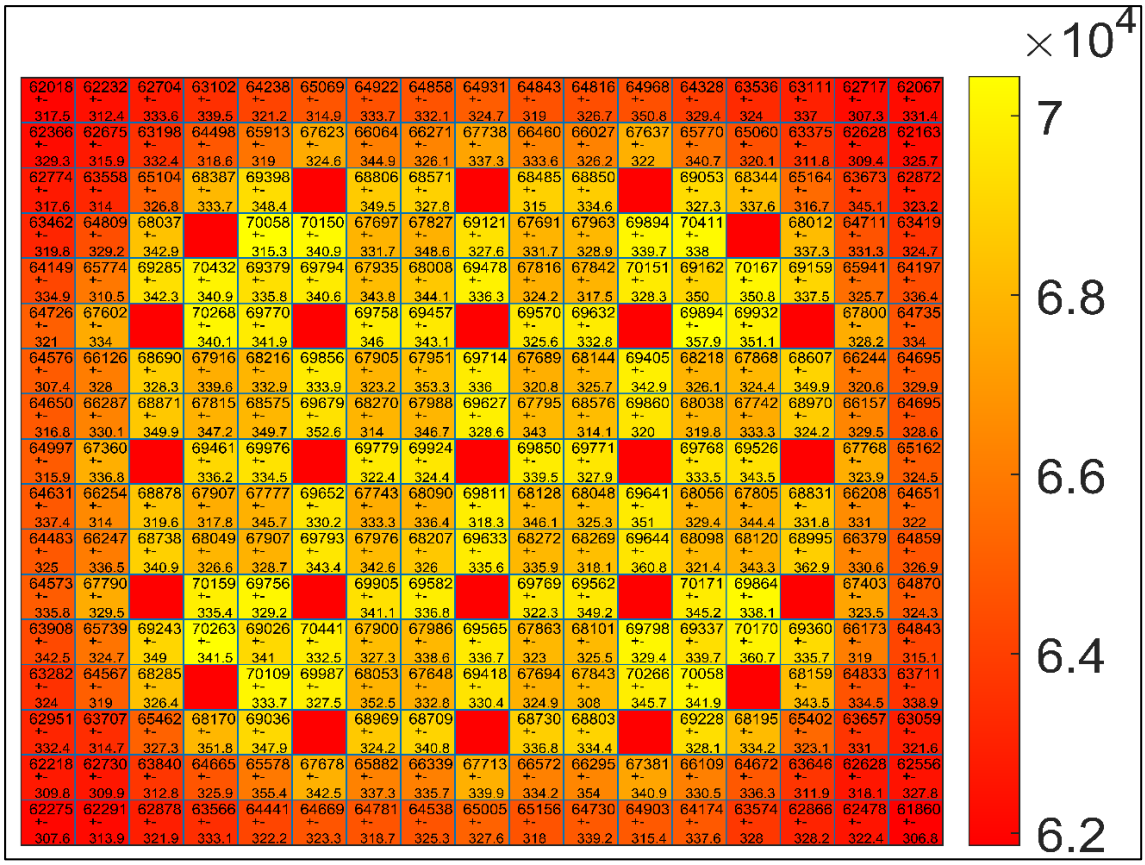

Figure 4-11:Pin power distribution in FCM fuel assembly in Watts

The power map in Figure 4-11 shows the fission power in each fuel rod for the FCM fuel assembly with its power uncertainty. The power map shows that the maximum fission energy released into the system is 70,411 watts, while the minimum energy released is 61,860 watts. The power peaking in the fuel assembly is $p = \frac{Hottest\ rod\ power}{average\ rod\ power} = \frac{70{,}411}{66{,}951} = 1.051$ .The FCM fuel assembly has a slightly flatter power profile than the UO_2 fuel assembly. The maximum power is in the same position in Figure 4-11 and Figure 4-10.This could be an inherent produt design in the fuel assembly.

4.3.2 Cycle length

This section examines the multiplication factor as a function of EFPD of the UO_2 and FCM fuel assembly.

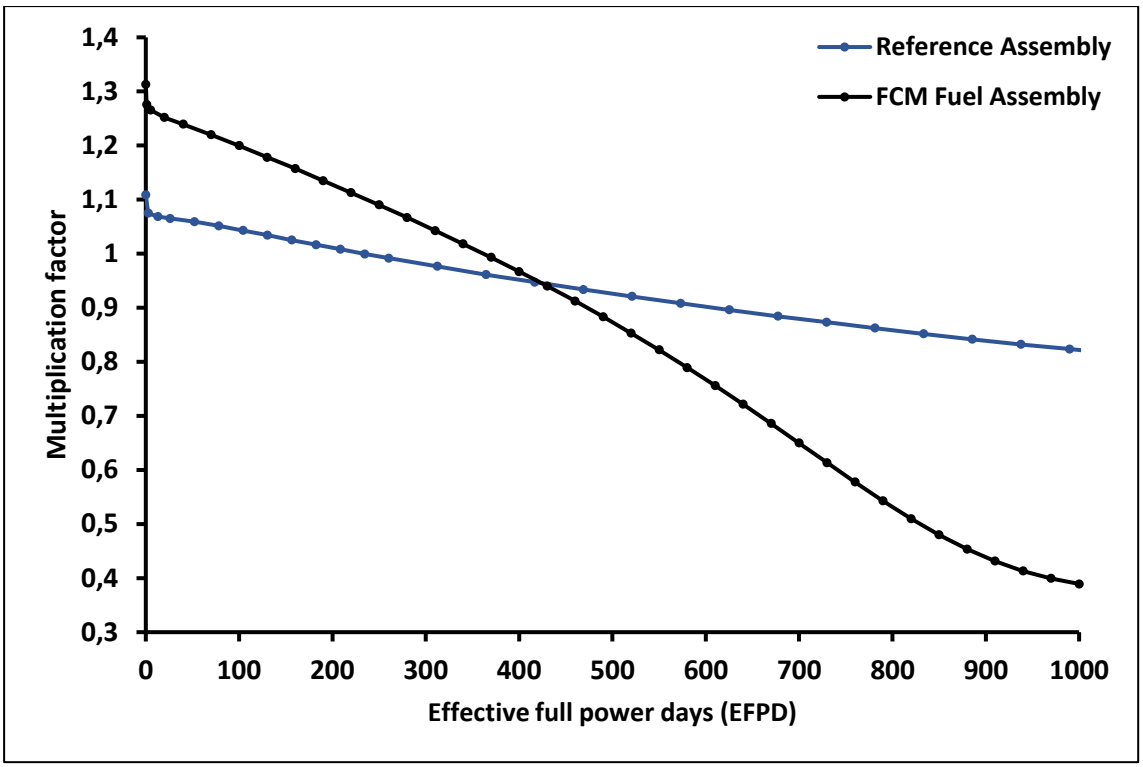

Figure 4-12: k_{eff} vs EFPD for UO_2 fuel and FCM fuel assembly

Figure 4-12 shows that the FCM fuel assembly has higher reactivity at the BOC than the UO_2 fuel assembly. After all, the FCM fuel has a higher enrichment because the FCM fuel has a lower total uranium mass loadings (^{235}U and ^{238}U) and aims to maintain that the number of ^{235}U in the FCM and UO_2 fuel are the same. The masses differ slightly because the ^{235}U is constant but the ^{238}U decreased and this overall decrease in mass because ^{238}U has 3 more neutrons than ^{235}U which effects the resonance absorption. The UO_2 pellet fuel falls from super-critical to subcritical between 208 and 230 EFPD, while the FCM fuel is between 340 and 370 EFPDs. The UO_2 pellet fuel and the FCM fuel reactivity cross between 430 and 460 EFPD as the ^{235}U is depleted quickly because of the FCM fuel material properties that thermalise neutrons and reduced breeding. The UO_2 has a smoother gradient than the FCM fuel, which allows it to last longer as the number of EFPD increases because of the excessive production of plutonium compared to FCM fuel, as plutonium plays a role in energy production. That is why at the EOC, the reactivity of the UO_2 pellet fuel is higher than the FCM fuel. The maximum statistical uncertainty for the results of the UO_2 pellet assembly is 25 pcm, while for the FCM fuel, it is 36 pcm.

The number of ^{235}U atoms between the two fuel designs remain the same but the ratio of $\frac{^{235}U}{^{238}U}$ increases which could contribute to an overall lower resonanace absorption leading to a higher multiplicaton factor for the FCM fuel at the BOC. Lastly because the FCM fuel is in carbon and

silicon based matrix they carbon is known to moderator which contributes to a softer neutron spectrum.

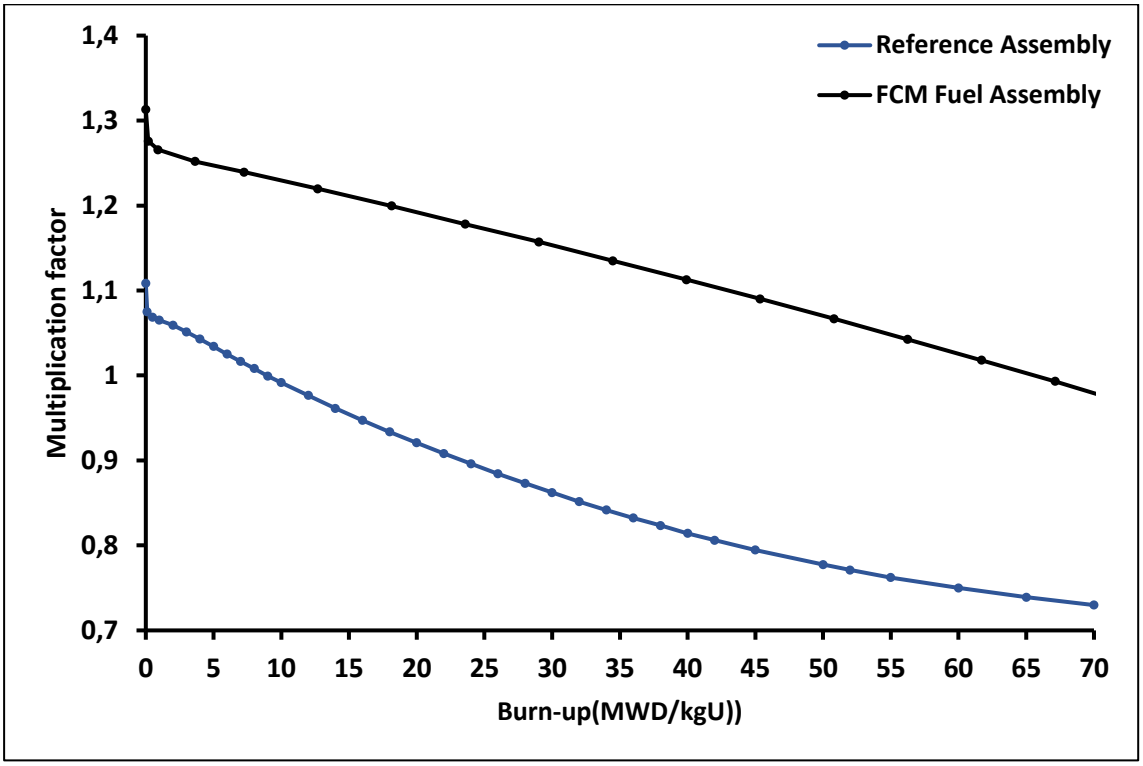

Figure 4-13: k_{eff} vs burnup for UO2 and FCM fuel

Figure 4-13 shows that at the BOC, the reactivity of FCM fuel is higher than the UO_2 fuel assembly and remains higher than the UO_2 pellets until 70 MWD/kgU. At 70 MWD/kgU, it is about 370 to 400 EFPD for the FCM fuel, while for the UO_2 fuel, it is at 1823 EFPD. This is first because of the lower total uranium mass loadings(^{235}U and ^{238}U), and secondly, it also tells us that with the FCM fuel, more power can be extracted from lower total uranium mass loadings. This tells us that the efficiency of converting mass into energy is better in the FCM fuel than in the UO_2 pellet. The improved efficiency is also attributed to the increased enrichment in the FCM fuel required. It should be bed noted that the results is limited because the FCM fuel assembly might only be optimally for one cycle use but there is a lack of understanding when used for more than one cycle.

4.3.3 Neutron spectrum

Figure 4-14 shows that the FCM fuel pin at 0 EFPD has a softer spectrum than the reference pin and that at the end of the cycle 1000 EFPD, the reference pin shows that the spectrum hardens while the FCM fuel pin spectrum softens.

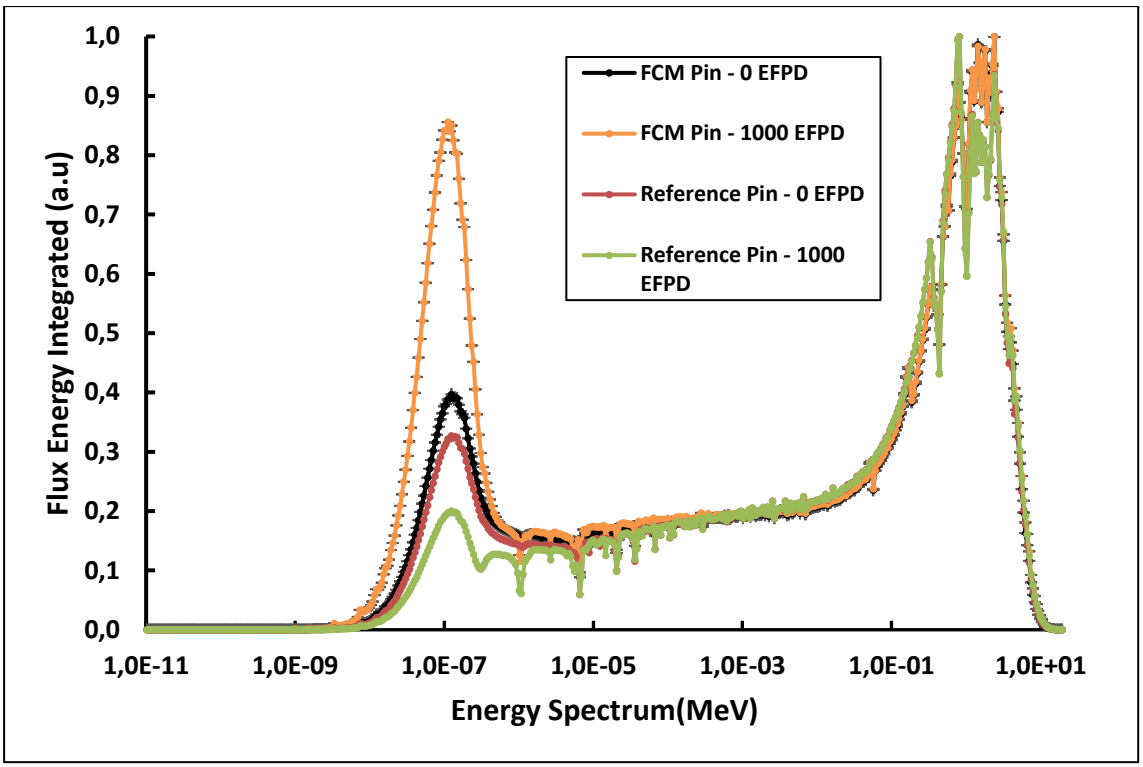

Figure 4-14:Neutron spectrum comparison between UO_2 and FCM fuel pin

The spatial self-shielding is not prevalent in the FCM fuel because the neutron is not absorbed by the SiC matrix, and the travel path for the neutron is not blocked by the outer surface of FCM fuel which prevents the neutron flux from being significantly lower in its inner surface. The energy and spatial self-shielding effect is not prevalent like in the UO_2 fuel, as the neutron softening in the FCM fuel shifts the neutron's energy away from the resonance region.

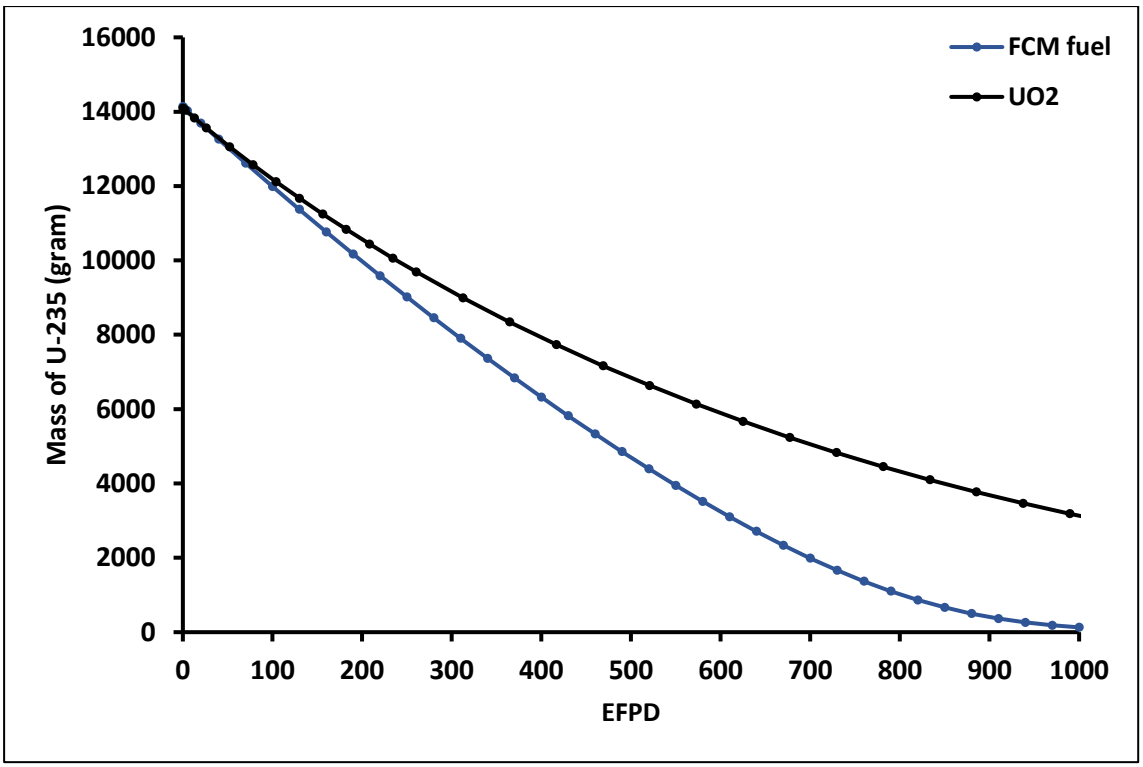

Figure 4-15:Mass of ^{235}U over EFPD

Figure 4-15 shows that in the FCM fuel, the amount of ^{235}U depletion rate in the FCM fuel is higher because of the softening of the spectrum as the EFPD increases and the lower total uranium mass loadings. The softening of the neutron spectrum means that the energy of the neutrons moves further away from the resonance region as EFPD increases. This leads to a higher burnup and lowers plutonium production, as the energy and spatial self-shielding plays a minimal role in the energy production of the FCM fuel.

4.3.4 Fractional releases and failure fractions of TRISO particles

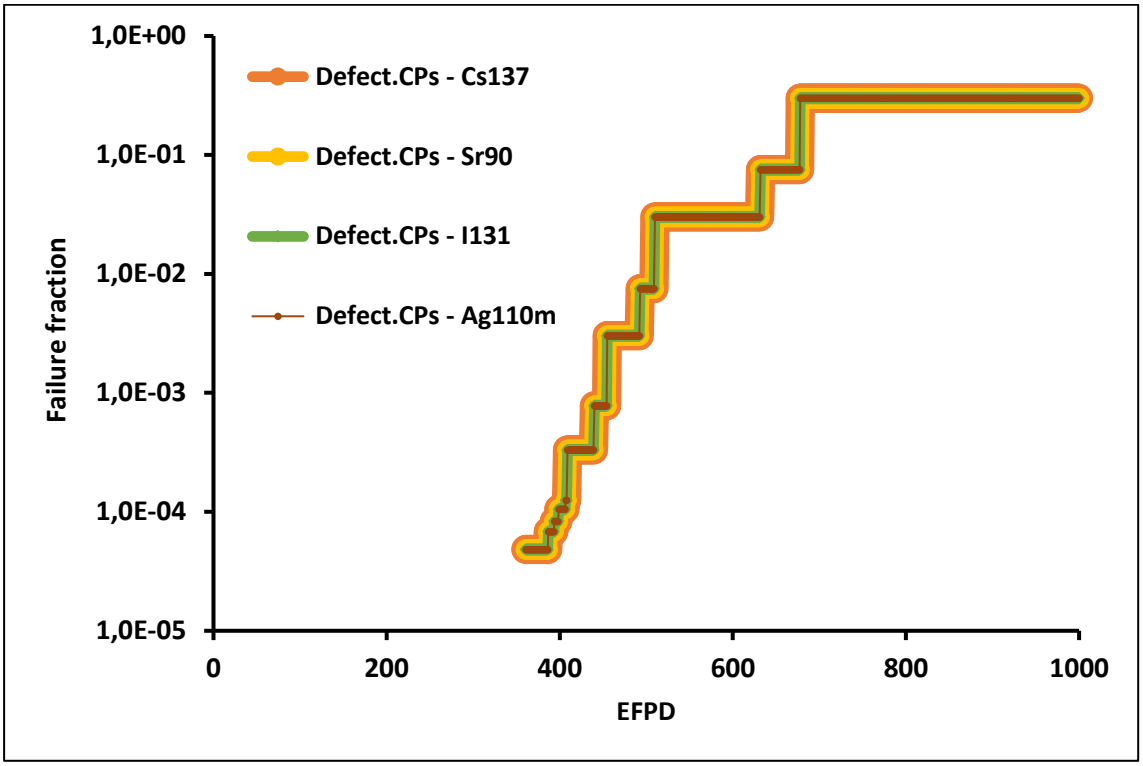

Figure 4-16: Failure fraction of TRISO particles

Figure 4-16, like Figure 4-8, shows when the failure of the TRISO particles begins and is seen when comparing the two figures. It is seen that the failure fraction of TRISO-coated particles happens 80 days earlier in the pin model than for the fuel assembly for conservative estimates when using ^{110m}Ag as a benchmark for comparison. The neutron spectrum in a fuel assembly is softer than in a pin model because of the guide tube moderating effect on the assembly neutron spectrum.

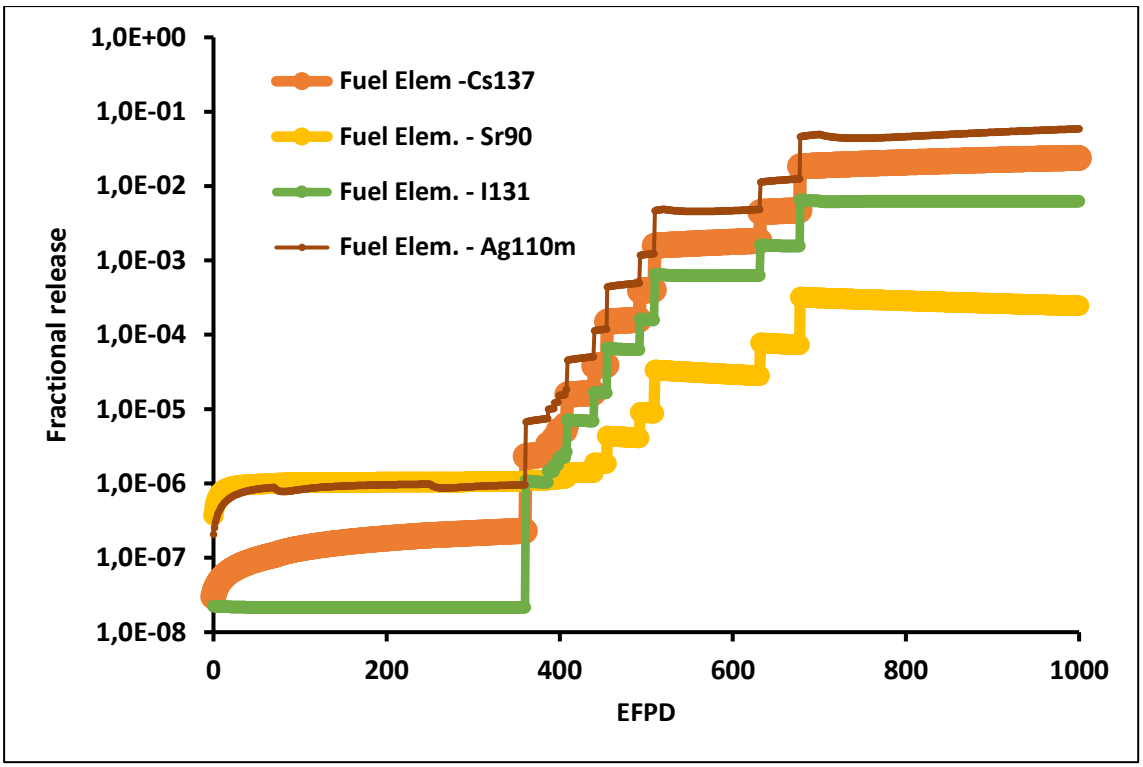

Figure 4-17: Fractional release of isotopes outside the FCM fuel

Figure 4-17, like Figure 4-9, shows the fractional release of different isotopes, and when comparing the two figures. The fractional release of the pin models shows that Figure 4-17 and Figure 4-9 are similar and that the failure of TRISO particles in the pin model begins 28 days earlier. Figure 4-17 shows that the fission product that escapes the most from the FCM fuel is ^{110m}Ag.

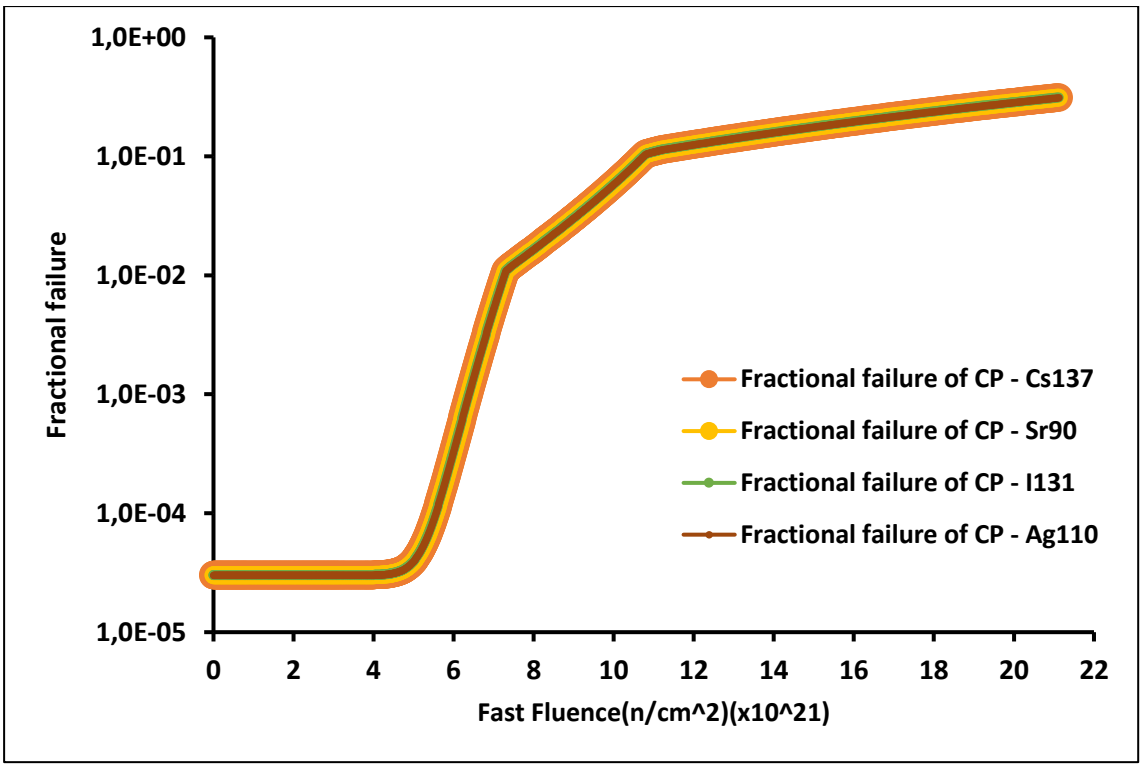

Figure 4-18:Fractional failure over fast fluence

Figure 4-18 shows that from $5 \times 10^{21} \frac{n}{cm^2}$ the fractional failure of particles gradient increases, and from $7 \times 10^{21} \frac{n}{cm^2}$ the fractional failure gradient decreases as the fractional failure increases, and its gradient further decreases at $11 \times 10^{21} \frac{n}{cm^2}$ as the fast fluence increases to the end of the cycle.

4.3.5 Conclusion

This section shows how the power peaking for the FCM fuel assembly is slightly flatter than the UO_2 fuel assembly. This section shows that the FCM fuel assembly cycle length is shorter because of the lower total uranium mass loadings and lower plutonium production. This section showed us that the FCM fuel assembly could produce more energy from less total uranium mass loadings than the UO_2 fuel assembly. The section showed how both fuels' neutron spectrum differ in softening and hardening. We also see that a high fast fluence in the LWR conditions compromises the structural integrity of the TRISO particles. The section also examined fractional releases and how failure fraction increases the fission product's overall release.

CHAPTER 5 COMPARISON

This section will compare the results from different literature sources on FCM fuel performance in similar conditions and irradiations.

It should be noted that for failure fraction, the notion of fractional failure is used and differs in the sense that failure fraction usually refers to the whole of TRISO particles. In contrast, fractional failure refers to the fraction of TRISO particles failing, which in some cases requires rounding off to the closest whole number of failed particles.

5.1 OGL-1 comparison

Table 5-1 compares the results from STACY of the hot pin with the ORGL experiments for limited comparison.

Table 5-1:Failure fraction and fractional release comparison

	Irradiation conditions			**Failure fraction (SiC coating)**		**EOL R/B (^{88}Kr)**
Name	Time (EFPD)	Temperature ℃	%FIMA	BOL	EOL	EOL
OGL-1	130.2	1331	2.8	7.5×10^{-4}	1.2×10^{-3}	3.2×10^{-6}
ORL-2	218	1180	2.3	5.1×10^{-5}	-	3.8×10^{-7}
STACY-hot pin	130	798	2.77	3×10^{-5}	3×10^{-5}	2.14×10^{-8}
STACY-hot pin	218	798	4.65	3×10^{-5}	3×10^{-5}	2.14×10^{-8}

Table 5-1 shows that the release from the OGL-1 is higher because the temperature is firstly higher, and the fast fluence for the STACY hot pin is low when examining Figure 4-18. The low release in the FCM fuel and low failure fraction of TRISO particles also contribute to the lower release in the fission products.

5.2 German irradiations

Table 5-2 compares the German irradiations and STACY's results to evaluate the fuel performance of the FCM fuel.

Table 5-2:German Irradiation releases comparison

Experiment	Compact name	Irradiation conditions			Release at the end of irradiation	
		Time (EFPD)	Temperature ℃ (Surface/Center Temperature)	%FIMA	Fractional release of ^{137}Cs	EOL R/B (^{88}Kr)
FRAJ2-P27	P27/1	232	880 / 1080	7.6	2×10^{-5}	2×10^{-6}
FRAJ2-P27	P27/2	232	1220 / 1320	8.0	1×10^{-4}	1×10^{-5}
STACY-hot pin	-	357	798	7.61	2.29×10^{-7}	2.14×10^{-8}
STACY-hot pin	-	376	798	8.01	2.38×10^{-6}	1.04×10^{-6}

Table 5-2 shows that when comparing similar FIMA for FCM fuel and FRAJ2-P27, we see more release in the FRAJ2-P27, which could be because the FRAJ2-P27 experiment was done at significantly higher temperatures than the hot pin for STACY.

5.3 Simulation of FCM fuel in LWRs

Table 5-3 compares the fuel performance between the STACY results for the hot pin and the simulation of the fuel performance for a Westinghouse fuel assembly.

Table 5-3:Simualation of FCM fuel comparison

	Irradiation conditions			Failure fraction		Fractional Release of ^{137}Cs
Name	Time (EFPD)	Temperature ℃	Fast fluence (10^{21} $\frac{n}{cm^2}$)	BOL	EOL	EOL
SiC 600 ℃	-	650	8.74	-	3.866×10^{-3}	-
SiC 800 ℃	-	850	8.703	–	4.41×10^{-4}	-
STACY-hot pin	580	798	8.712	3×10^{-5}	2.489×10^{-2}	4.48×10^{-3}
STACY-hot pin	582	798	8.733	3×10^{-5}	2.554×10^{-2}	4.49×10^{-3}

Table 5-3 shows that when a high fast fluence is reached, there is a severe degradation in the ability of the TRISO particles to retain the fission product in the fuel. When examining the amount of ^{137}Cs outside the FCM fuel, only 0.45% maximum was outside the FCM fuel, which can be attributed to the SiC matrix's ability to slow the diffusion of fission product inside its

matrix. When examining the failure fraction at the EOL, it is seen that the FCM fuel pin performs worse than the simulation results for the Westinghouse fuel assembly. The TRISO particles' structural integrity is vulnerable to high flux irradiation conditions; thus the poor performance compared to the Westinghouse fuel assembly simulation results.

5.4 Safety requirement

Table 5-4 compares the fuel performance of the hot pin from the fuel assembly and the safety requirement of the HTR and PBMR TRISO-based fuel design.

Table 5-4:Safety requirement comparison

	Irradiation conditions			**Failure fraction**	
Name	Time (EFPD)	Temperature ℃	Fast fluence ($10^{21}\ \frac{n}{cm^2}$)	BOL	EOL
HTR-Design	-	800 -1200	4-5	-	3×10^{-4}
PBMR-Design	-	800 -1200	4-5	–	2×10^{-4}
STACY-hot pin	303	798	4.002	3×10^{-5}	3.01×10^{-5}
STACY-hot pin	367	798	5.012	3×10^{-5}	3.98×10^{-5}

Table 5-4 shows that no significant failure takes place for $(4-5) \times 10^{21}\frac{n}{cm^2}$ as shown from Figure 4-8, and that significant fractional failure only begins to increase above $5 \times 10^{21}\frac{n}{cm^2}$ gradually. The comparison is limited because it shows that the FCM fuel for the hot pin is superior compared to HTR and PBMR data, but the HTR and PBMR designs are for gas reactors with lower fast fluence than the typical LWR, as the LWR reactors have a higher power density than gas reactors.

5.5 Conclusion

The section shows us how in section 5.1, the FCM fuel performs better because of the low fast fluence the FCM fuel experiences. Section 5.2 shows that the FCM fuel performs better because of the much lower fuel temperature. Section 5.3 shows how the FCM fuel performance is worse because of the high fluence the FCM fuel experiences. Section 5.4 shows that the design criteria in HTGR for the FCM fuel are within the design specifications.

CHAPTER 6 CONCLUSION

6.1 Findings

- The FCM fuel has a better fission product retention ability than the traditional PBMR pebble or HTR-modul fuel. Examining the FCM fuel reveals the benefits and shortcomings of the FCM fuel in LWR conditions. The FCM fuel, as a replacement for the traditional UO_2, will increase the safety redundancy by improving the fuels' safety barrier.
- From an inhalation toxicity perspective, the FCM fuel can reduce inhalation toxicity by two orders of magnitude of sieverts should an accident occur. This uses conservative estimates (assuming that the fuel is the only safety barrier).
- When comparing the FCM and the UO_2 multiplication factor gradient as the EFPD increases, it is seen that the UO_2 fuel reactivity decreases slower as the EFPDs increase, which means the UO_2 can burn longer.
- When comparing the burnup, the FCM fuel and the UO_2 show that the FCM fuel has a larger burnup, meaning that the FCM fuel can produce more energy from lower total uranium mass loadings.
- The increased safety redundancy for FCM fuel comes at the cost of shorter cycle length. More frequent reloading is required and there is a lowered capacity factor because of the lower production of plutonium but increased efficiency on energy extraction from total uranium mass loadings.
- The FCM fuel is shown not to have power peaking issues in its fuel assembly and is an improvement attributed to its improved thermal conductivity of the FCM fuel. The improved thermal conductivity also means that the FCM fuel has a much lower fuel centreline temperature, which is beneficial in accident conditions and extends the cooling time before failure.
- The fast fluence nature of LWR compromises the TRISO particle structural integrity. The fast fluence nature of the LWR reduces the fuel performance of the FCM fuel. This is seen when comparing the defect fraction of the FCM fuel in a pin model and assembly model. The pin with a high fast fluence shows the TRISO particles are compromised first.
- The FCM fuel benefits from an improved thermal spectrum, allowing more thermalised neutrons as burnup increases. This increase in thermalised neutrons also means that plutonium production is lowered because the energy spectrum is shifted away from the resonance region, which means the energy self-shielding effect is less prominent.

6.2 Shortcomings

There are shortcomings with the simulation. Firstly, the fuel temperature at each burn and day (MWd/kgU and EFPD) is constant, and then the fuel dimensions remain constant even through irradiation. The experimental comparison cases are limited as the FCM in the LWR condition is compared with HTGR reactors for experimental results, while for LWR conditions, only simulation data exist for comparison.

A significant shortcoming is the failure to use the South African PBMR data as this was unavailable. This limited the number of comparisons that could be made relevant to a South African context.

The aim and objectives were completed, except that it was impossible to compare the retention ability of the FCM fuel and UO_2 directly. The substitute inhalation toxicity was used to compare the FCM fuel and UO_2 fuel, which relies on the assumption that UO_2 has zero retention ability.

6.3 Recommendations

- Improvements could be made to the project with the help of coupling a thermal hydraulics code into the neutronics code to be more accurate.
- The project could use STACY, which incorporates the full core instead of the stand-alone version that can only calculate one fuel rod at a time.
- The fuel and the moderator temperature coefficient could be investigated to understand better the reactor stability of a reactor fuelled by FCM fuel.
- The UO_2 fuel for the FCM kernel could be replaced with a (U, Th)O_2 oxide mixture to extend the FCM fuel cycle length and promote breeding.
- The design of FCM fuel is optimised for higher fluences and power densities to reduce the failure fractions of TRISO particles in FCM fuel.
- Future experimental works for the use of FCM could be used to better corroborate the results presented here and possibly consolidate results in a single database.
- The FCM fuel could be examined when used as a multi-cycle fuel and not as a single use fuel use.
- The method used to calculate temperature lack accuracy of CFD codes and a CFD could be used to improve the accuracy.
- Diffusion modelling in helium and in cladding could be added to the STACY code in the future.

BIBLIOGRAPHY

Al-Zahrani, Y.A. *et al.* (2021) 'Neutronic performance of fully ceramic microencapsulated of uranium oxycarbide and uranium nitride composite fuel in SMR', *Annals of Nuclear Energy*, 155, p. 108152. Available at: https://doi.org/10.1016/j.anucene.2021.108152.

Allelein, H.J. *et al.* (2016) 'First results for fluid dynamics, neutronics and fission product behavior in HTR applying the HTR code package (HCP) prototype', *Nuclear Engineering and Design*, 306, pp. 145–153. Available at: https://doi.org/10.1016/j.nucengdes.2016.04.028.

Bergman, T.L. *et al.* (2007) *Fundamentals of heat and mass transfer*. 7th edn. John Wiley & Sons.

Bowman, S. and Suto, T. (1996) *SCALE-4 Analysis of Pressurized Water Reactor Critical Configurations :*, *Oak Ridge National Laboratory,Oak Ridge*.

Brown, F.B. (2006) 'On the use of shannon entropy of the fission distribution for assessing convergence of Monte Carlo criticality calculations', *PHYSOR-2006 - American Nuclear Society's Topical Meeting on Reactor Physics*, pp. 1–6.

Brown, N.R. *et al.* (2022) 'High volume packing fraction TRISO-based fuel in light water reactors', *Progress in Nuclear Energy*, 146, p. 104151. Available at: https://doi.org/10.1016/j.pnucene.2022.104151.

Chen, S. and Yuan, C. (2017) 'Neutronic Analysis on Potential Accident Tolerant Fuel-Cladding Combination U 3 Si 2 -FeCrAl', *Science and Technology of Nuclear Installations*, 2017, pp. 1–12. Available at: https://doi.org/10.1155/2017/3146985.

Cho, Y.S. and Hong, S.G. (2020) 'Physics analysis of new TRU recycling options using FCM and MOX fueled PWR assemblies', *Nuclear Engineering and Technology*, 52(4), pp. 689–699. Available at: https://doi.org/10.1016/j.net.2019.10.006.

Collin, B. and Power, K. (2013) *Modeling and analysis of FCM UN TRISO Fuel Using the PARFUME Code*. Available at: https://doi.org/10.2172/1111502.

Collin, B.P. *et al.* (2016) 'Comparison of fission product release predictions using PARFUME with results from the AGR-1 safety tests', *Nuclear Engineering and Design*, 301(August), pp. 378–390. Available at: https://doi.org/10.1016/j.nucengdes.2016.03.023.

Collin, B.P. (2016) *Diffusivities of Ag, Cs, Sr, and Kr in TRISO Fuel Particles and Graphite*,

Idaho National Laboratory,Idaho. Available at: https://inldigitallibrary.inl.gov/sites/sti/sti/7245704.pdf.

Deng, Q. *et al.* (2022) 'Neutronic design and evaluation of the solid microencapsulated fuel in LWR', *Nuclear Engineering and Technology*, xxx(xxxx), p. xxx. Available at: https://doi.org/10.1016/j.net.2022.03.020.

Eltawila, F. (2004) *TRISO-Coated Particle Fuel Phenomenon identification and ranking tables (PIRTs) for Fission Product Transport Due to Manufacturing, Operations, and Accidents*, *NUREG/CR-6844,Nuclear Regulatory Commission,Washington*.

Fang, C. *et al.* (2021) 'Analysis of Fission Products' Release in Pebble-Bed High-Temperature Gas-Cooled Reactor Fuel Elements Using a Modified FRESCO II Numerical Model', *Science and Technology of Nuclear Installations*, 2021. Available at: https://doi.org/10.1155/2021/6627789.

Gerczak, T.J. (2021) 'Irradiation Performance: High-Temperature Gas Reactor Fuels', *Encyclopedia of Nuclear Energy*, 2, pp. 407–419. Available at: https://doi.org/10.1016/b978-0-12-819725-7.00095-7.

Gorton, J.P. *et al.* (2019) 'Reactor performance and safety characteristics of ThN-UN fuel concepts in a PWR', *Nuclear Engineering and Design*, 355(July), p. 110317. Available at: https://doi.org/10.1016/j.nucengdes.2019.110317.

Hakim, A.R. *et al.* (2019) 'Neutronic analysis of fuel assembly design in Small-PWR using uranium mononitride fully ceramic micro-encapsulated fuel using SCALE and Serpent codes', *Nuclear Engineering and Technology*, 51(1), pp. 1–12. Available at: https://doi.org/10.1016/j.net.2018.08.007.

Hales, J.D. *et al.* (2021) 'Modeling fission product diffusion in TRISO fuel particles with BISON', *Journal of Nuclear Materials*, 548, p. 152840. Available at: https://doi.org/10.1016/j.jnucmat.2021.152840.

Horelik, N. *et al.* (2017) 'MIT Benchmark for Evaluation And Validation of Reactor Simulations', *Proc. Int. Conf. Mathematics and Computational Methods Applied to Nuc. Sci. & Eng., Sun Valley, Idaho* [Preprint].

IAEA (1997) 'Fuel Performance and Fission Product Behaviour in Gas-Cooled Reactors', *IAEA-TECDOC-978, International Atomic Energy Agency, Vienna*, pp. 1–529.

IAEA (2010) ‘High Temperature Gas Cooled Reactor Fuels and Materials’, *IAEA TECDOC-1645-CD, International Atomic Energy Agency, Vienna*, pp. 1–182.

IAEA (2012) ‘IAEA-TECDOC-1674-advanccs in high temperature gas cooled reactor fuel technology’, *Technical committee meeting held in Vienna* [Preprint], (IAEA-TECDOC-CD-1674).

IAEA (2014) *Accident Tolerant Fuel Concepts for Light Water Reactors*, *Proceedings of a Technical Meeting held at Oak Ridge National Laboratories*. Edited by IAEA. Tennessee. Available at: https://www.iaea.org/publications/10972/accident-tolerant-fuel-concepts-for-light-water-reactors.

Jiang, W. *et al.* (2021) ‘TRISO particle fuel performance and failure analysis with BISON’, *Journal of Nuclear Materials*, 548, p. 152795. Available at: https://doi.org/10.1016/j.jnucmat.2021.152795.

Kasselmann, S. *et al.* (2014) ‘Status of the development of a fully integrated code system for the simulation of high temperature reactor cores’, *Nuclear Engineering and Design*, 271, pp. 341–347. Available at: https://doi.org/10.1016/j.nucengdes.2013.11.059.

Kępisty, G. and Cetnar, J. (2017) ‘On the discrepancies between FIMA and specific burnup’, *Progress in Nuclear Energy*, 98, pp. 187–192. Available at: https://doi.org/10.1016/j.pnucene.2017.03.016.

Keun, C. *et al.* (2014) ‘Preliminary Core Analysis of a Micro Modular Reactor’, *Transactions of Korean Nuclear Society Spring Meeting*, p. 4.

Kim, Y. *et al.* (2005) ‘Reactivity-Equivalent Physical Transformation for Homogenization of Double-Heterogeneous Fuels’, *Transactions of the Korean Nuclear Society Autumn Meeting, Busan, Korea, October 27-28, 2005* [Preprint].

Lamarsh, J.R. and Baratta, A. (2001) *Introduction to Nuclear Engineering*. 3rd edn. Prentice Hall. Available at: https://doi.org/10.1119/1.1933896.

Lavarenne, J. *et al.* (2022) ‘Burn-Up Dependent Modeling of Fuel-to-Clad Gap Conductance and Temperature Predictions for Mixed-Oxide Fuel in the ESFR-SMART Core’, *Journal of Nuclear Engineering and Radiation Science*, 8(1), pp. 1–11. Available at: https://doi.org/10.1115/1.4050479.

Lee, W.J. *et al.* (2013) *Fully ceramic micro-encapsulated (fcm) replacement fuel assembly for lwrs*, *International Congress on Advances in Nuclear Power Plants, ICAPP 2013: Nuclear*

Power - A Safe and Sustainable Choice for Green Future, Held with the 28th KAIF/KNS Annual Conference.

Lepp, J. (2011) 'Serpent – a Continuous-energy Monte Carlo Reactor Physics Burnup Calculation Code', *Technical Research Centre of Finland*, p. 157.

Li, J. *et al.* (2021) 'A comparison study on mechanical models for TRISO fuel particle in HTGR', *Annals of Nuclear Energy*, 161, p. 108484. Available at: https://doi.org/10.1016/j.anucene.2021.108484.

Liu, H. (2017) *HIGH TEMPERATURE DEGRADATION OF SILICON CARBIDE (SIC) BY METALLIC FISSION PRODUCTS (PALLADIUM, SILVER) AND OXIDATION*, *A thesis submitted to the University of Manchester for the degree of Doctor of Philosophy in Material Science,Manchester*.

Massih, A. (2006) *Models for MOX fuel behaviour*, *SKI Report*. Sweden.

Massoud, M. (2005) *Engineering Thermofluids: Thermodynamics, Fluid Mechanics, and Heat Transfer*.

Miller, G.K. *et al.* (2010) 'Calculating failure probabilities for TRISO-coated fuel particles using an integral formulation', *Journal of Nuclear Materials*, 399(2–3), pp. 154–161. Available at: https://doi.org/10.1016/j.jnucmat.2010.01.012.

Mizokami, S. and Rempe, J.L. (2020) *The Events at Fukushima Daiichi*, *Reference Module in Earth Systems and Environmental Sciences*. Elsevier Inc. Available at: https://doi.org/10.1016/b978-0-12-409548-9.12148-7.

Morris, R.N. and Pappano, P.J. (2007) 'Estimation of maximum coated particle fuel compact packing fraction', *Journal of Nuclear Materials*, 361(1), pp. 18–29. Available at: https://doi.org/10.1016/j.jnucmat.2006.10.017.

Mulasi, C. (2021) 'Criticality study of a spent fuel pool using SCALE 6.2.3 and MCNP6.2', *Master ed. North West University,Potchefstroom,South Africa*, pp. 1–76.

NEA (2010) *Under Reactivity-initiated Accident (RIA) Conditions ORGANISATION FOR ECONOMIC CO-OPERATION AND DEVELOPMENT*. Vienna.

NRC (2016) 'North Anna Power Station Updated Final Safety Analysis Report Chapter 1'.

Pope, M.A. *et al.* (2012) 'Neutronic analysis of the burning of transuranics in fully ceramic micro-

encapsulated tri-isotropic particle-fuel in a PWR', *Nuclear Engineering and Design*, 252, pp. 215–225. Available at: https://doi.org/10.1016/j.nucengdes.2012.07.013.

Powers, J.. *et al.* (2013) *Fully Ceramic Microencapsulated (FCM) Replacement Fuel for LWRs*. Tennessee.

Powers, J.J. and Wirth, B.D. (2010) 'A review of TRISO fuel performance models', *Journal of Nuclear Materials*, 405(1), pp. 74–82. Available at: https://doi.org/10.1016/j.jnucmat.2010.07.030.

Qasim Awan, M. *et al.* (2018) 'Neutronic design study of a small modular IPWR loaded with accident tolerant-fully ceramic micro-encapsulated (AT-FCM) fuel', *Nuclear Engineering and Design*, 335(28), pp. 18–29. Available at: https://doi.org/10.1016/j.nucengdes.2018.04.023.

Reihman, T.C. (1980) *Nuclear Engineering Computer Modules, Thermal-Hydraulics, TH-1: Pressurized Water Reactors.*

Schappel, D.P. (2017) *Improvements to the Predictive Capability of FCM Fuel Performance Modeling*, *Tennessee Research and Creative Exchange Doctoral,University of Tennessee, Knoxville*.

Snead, L.L. *et al.* (2007) 'Handbook of SiC properties for fuel performance modeling', *Journal of Nuclear Materials*, 371(1–3), pp. 329–377. Available at: https://doi.org/10.1016/j.jnucmat.2007.05.016.

Suman, S. (2021) 'Impact of hydrogen on rupture behaviour of Zircaloy-4 nuclear fuel cladding during loss-of-coolant accident: a novel observation of failure at multiple locations', *Nuclear Engineering and Technology*, 53(2), pp. 474–483. Available at: https://doi.org/10.1016/j.net.2020.07.017.

Terrani, K.A. *et al.* (2021) 'Architecture and properties of TCR fuel form', *Journal of Nuclear Materials*, 547, p. 152781. Available at: https://doi.org/10.1016/j.jnucmat.2021.152781.

Thomas, S. (2008) *Safety issues with the South African Pebble Bed Modular Reactor : When were the issues apparent ? A briefing paper by*. London. Available at: https://core.ac.uk/download/pdf/67307.pdf.

Verfondern, K. (2012) *Triso fuel performance modeling and simulation*, *Comprehensive Nuclear Materials*. Elsevier Inc. Available at: https://doi.org/10.1016/B978-0-08-056033-5.00076-8.

Verfondern, K. *et al.* (2014) 'Conclusions from V&V studies on the German codes PANAMA and

FRESCO for HTGR fuel performance and fission product release', *Nuclear Engineering and Design*, 271, pp. 84–91. Available at: https://doi.org/10.1016/j.nucengdes.2013.11.015.

Wells, B.E. *et al.* (2021) *TRISO Fuel : Properties and Failure Modes*, *PNNL-31427,Pacific Northwest National Laboratory,Oak Ridge*.

Xhonneux, A. and Allelein, H. (2014) 'Development of an integrated fission product release and transport code for spatially resolved full-core calculations of V / HTRs', *Nuclear Engineering and Design*, 271, pp. 361–369. Available at: https://doi.org/10.1016/j.nucengdes.2013.11.063.

Xhonneux, A. and Verfondern, K. (2016) 'Full Integration of the Fission Product Release Module STACY into the HTR Code Package (HCP)', pp. 1049–1058.

Zakova, J. (2012) *Advanced fuels for thermal spectrum reactors*, *Stockholm,Sweden*. Available at: http://kth.diva-portal.org/smash/get/diva2:558528/FULLTEXT01.pdf.

Zhang, C. *et al.* (2020) 'Multidimensional multiphysics modeling of TRISO particle fuel with SiC/ZrC coating using modified fission gas release model', *Annals of Nuclear Energy*, 145(May), p. 107599. Available at: https://doi.org/10.1016/j.anucene.2020.107599.

Zinkle, S.J. *et al.* (2014) 'Accident tolerant fuels for LWRs: A perspective', *Journal of Nuclear Materials*, 448(1–3), pp. 374–379. Available at: https://doi.org/10.1016/j.jnucmat.2013.12.005.

APPENDIX

7.1 Shannon Entropy

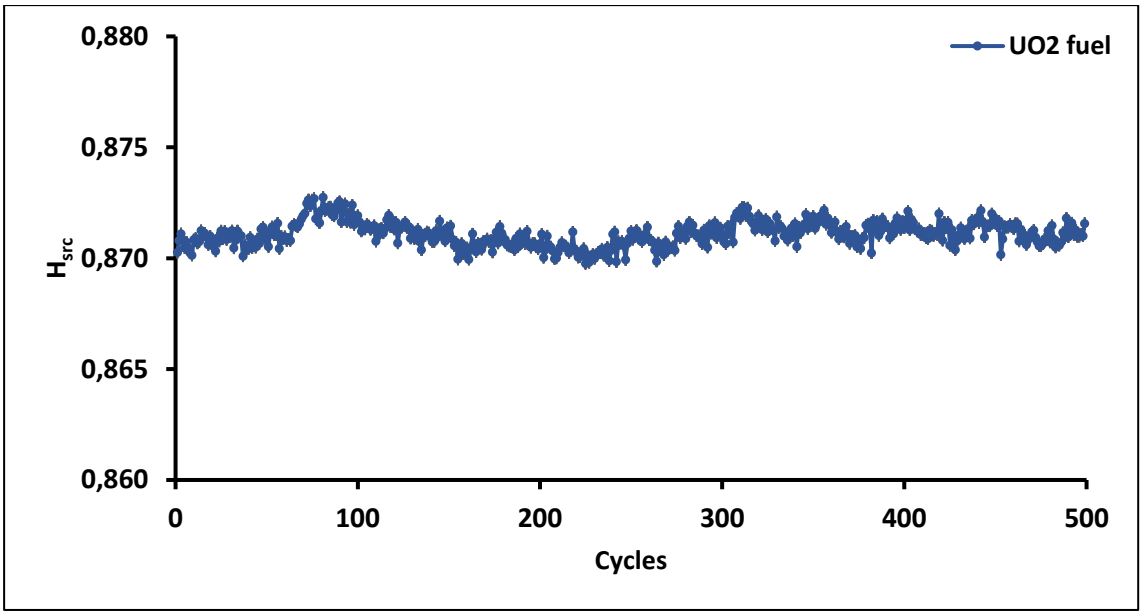

Figure 7-1:Shannon entropy for UO_2 pin fuel

Figure 7-1 shows the simulation in SERPENT convergence.

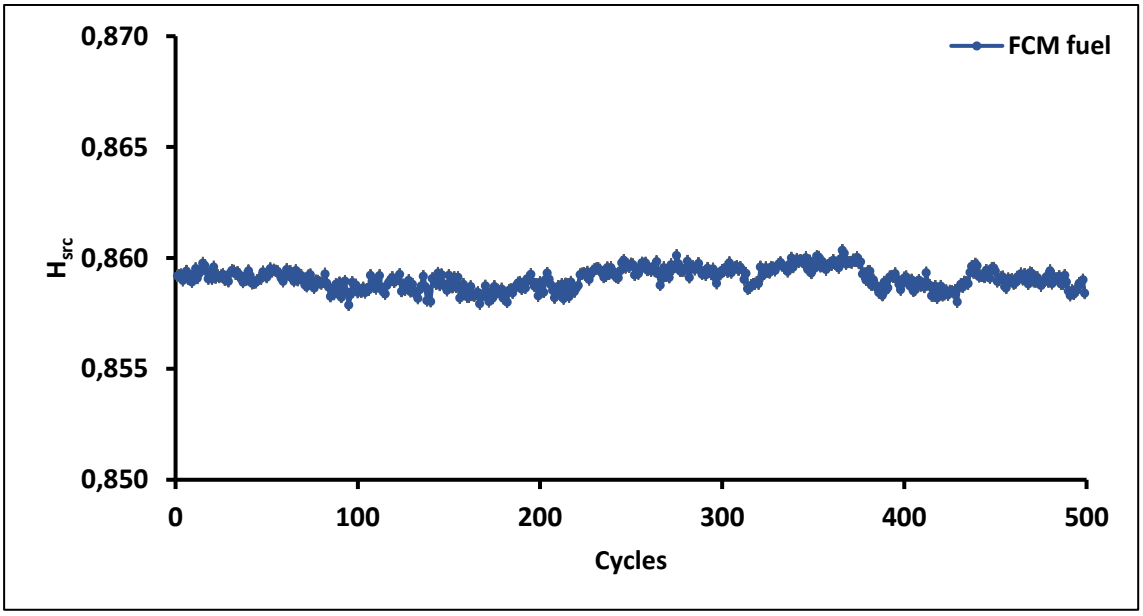

Figure 7-2: Shannon entropy for FCM pin fuel

Figure 7-2 shows the simulation in SERPENT convergence.

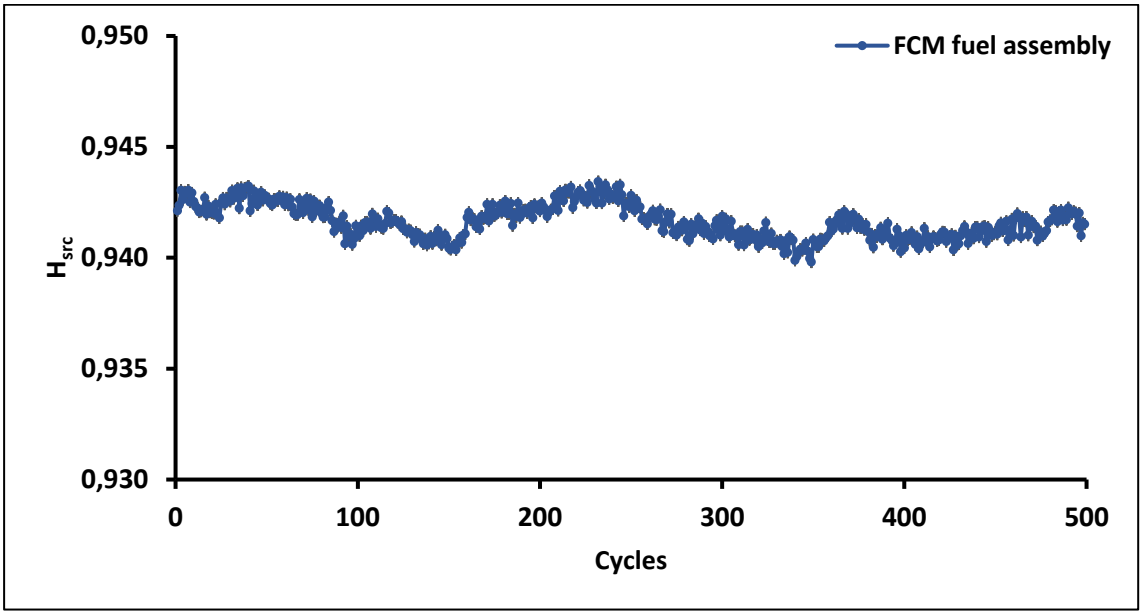

Figure 7-3: Shannon entropy for FCM fuel assembly

Figure 7-3 shows the simulation in SERPENT convergence.

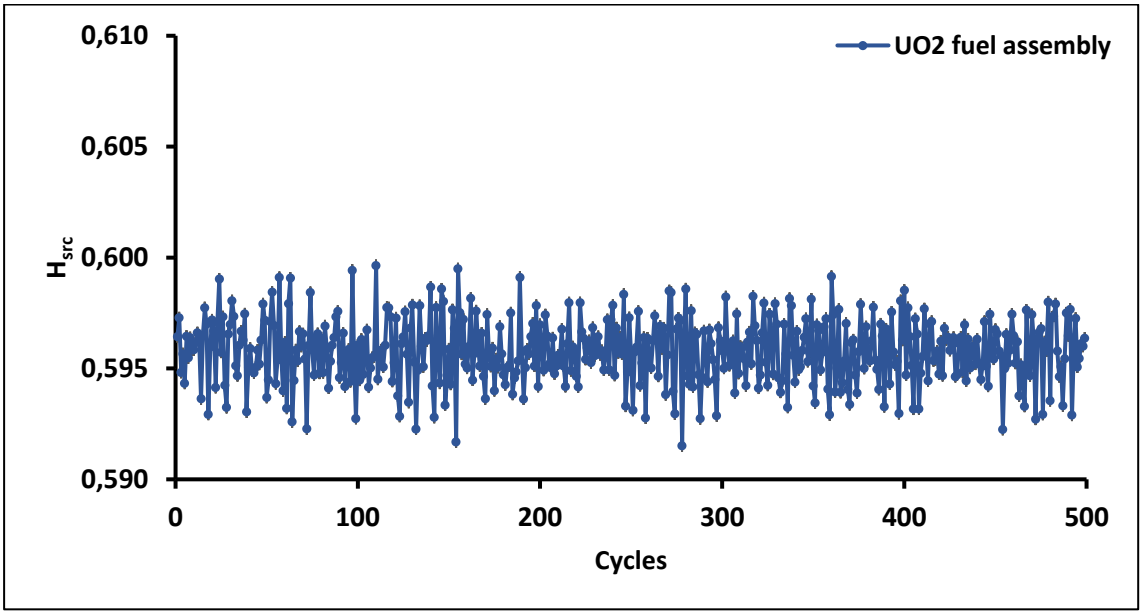

Figure 7-4: Shannon entropy for UO_2 fuel assembly

Figure 7-4 shows the simulation in SERPENT convergence.

7.2 SERPENT code

7.2.1 Pin model

7.2.1.1 UO_2 fuel

This section contains the SERPENT code for the pin model.

```
set acelib "/share/apps/Serpent2020/xsdata/endfb7/sss_endfb7u.xsdata"
set declib "/share/apps/Serpent2020/xsdata/endfb7/sss_endfb7.dec"
set nfylib "/share/apps/Serpent2020/xsdata/endfb7/sss_endfb7.nfy"
%set title "Pin"
include "/home/28862163/Serpent/Pin/burnup/Materials"
%include "/home/28862163/Serpent/PinTrisoRandom/Geometry"
%include "/home/28862163/Serpent/Burnup"
% --- Neutron population and criticality cycles:
set pop 100000 500 250
set bc 2 2 1
set power 66951
%set entr 10 10 330 -0.62992 0.62992 -0.62992 0.62992 -207.8990 207.8990
%set his 1
%set fsp 1 100
surf 1 cylz 0.0 0.0 0.409575 -182.499 182.499
%surf 7 cylz 0.0 0.0 0.209575 -182.499 182.499
surf 2 cylz 0.0 0.0 0.41783 -182.499 182.499
surf 3 cylz 0.0 0.0 0.47483 -182.499 182.499
surf 4 pz -182.499
surf 5 pz 182.499
surf 6 cuboid -0.62992 0.62992 -0.62992 0.62992 -207.8990 207.8990
%pin 100
%fuel 0.409575
%cool
cell 10 1 fuel -1
%cell 11 1 fill 100 -7
cell 20 1 helium -2 1
cell 30 1 clad -3 2
cell 40 1 cool 3
cell 50 0 fill 1 -6 4 -5
cell 51 0 reflbot -6 -4
```

```
cell 52 0 refltop -6 5
cell 60 0 outside 6
%Flux per Lethargy
%det EnergyDetector de MyEnergyGrid dt -3
%ene MyEnergyGrid 3 500 1e-11 2e1
%Axial Power Distribution
%det AxialPower du 1 dm fuel dz -182.499 182.499 10
%Radial Power Distribution
%det RadialPower du 1 dm fuel dx -0.62992 0.62992 6
%Fast Flux 0.18MeV 20 MeV
%ene EnergyGrid 1 0.1 1
%det FluxDetector ds 1 -2 de EnergyGrid dt -6
dep butot
  0.1
  0.5
  1.0
  2.0
  3.0
  4.0
  5.0
  6.0
  7.0
  8.0
  9.0
 10.0
 12.0
 14.0
 16.0
 18.0
 20.0
 22.0
 24.0
 26.0
 28.0
 30.0
 32.0
```

```
  34.0
  36.0
  38.0
  40.0
  42.0
  45.0
  50.0
  52.0
  55.0
  60.0
  65.0
  70.0
% --- Nuclide inventory:
set inventory
942390
942410
551370
471101
531310
380900
922350
922380
%ifc "/home/28862163/Serpent/Pin/burnup/Fuelface.ifc"
ifc "/home/28862163/Serpent/Pin/burnup/Coolant.ifc"
set rfw 1
set nbuf 10
set fpcut 1e-5
set gcu -1
set cmm 0
set shbuf 1 1
set repro 0
set opti 2
%plot 1 1000 1000
%plot 3 1000 1000
%mesh plots
det fission dr -8 void
```

```
mesh 8 3 fission 3  2000  2000
mesh 8 3 fission 1  2000  2000
det RadialFission dr -6 void dm fuel dn 1 0.0 0.409575 4 0 360 1 0 0 1
det RadialCapture dr -2 void dm fuel dn 1 0.0 0.409575 4 0 360 1 0 0 1
```

7.2.1.2 FCM fuel

This section contains the SERPENT code for the pin model for the FCM fuel

```
set acelib "/share/apps/Serpent2020/xsdata/endfb7/sss_endfb7u.xsdata"
set declib "/share/apps/Serpent2020/xsdata/endfb7/sss_endfb7.dec"
set nfylib "/share/apps/Serpent2020/xsdata/endfb7/sss_endfb7.nfy"
set title "PinTRISORandom"
include "/home/28862163/Serpent/PinTrisoRandom/burnup/Materials"
%include "/home/28862163/Serpent/PinTrisoRandom/Geometry"
%include "/home/28862163/Serpent/Burnup"
% --- Neutron population and criticality cycles:
set pop 100000 500 250
set bc 2 2 1
set power 66951
%set entr 10 10 330 -0.62992 0.62992 -0.62992 0.62992 -207.8990 207.8990
%set his 1
%set fsp 1 100
surf 1 cylz 0.0 0.0 0.409575 -182.499 182.499
%surf 7 cylz 0.0 0.0 0.209575 -182.499 182.499
surf 2 cylz 0.0 0.0 0.41783 -182.499 182.499
surf 3 cylz 0.0 0.0 0.47483 -182.499 182.499
surf 4 pz -182.499
surf 5 pz 182.499
surf 6 cuboid -0.62992 0.62992 -0.62992 0.62992 -207.8990 207.8990
%pin 100
%fill triso 0.409575
%cool
cell 10 1 fill triso -1
cell 20 1 helium -2 1
```

```
cell 30 1 clad -3 2
cell 40 1 cool 3
cell 50 0 fill 1 -6 4 -5
cell 51 0 reflbot -6 -4
cell 52 0 refltop -6 5
cell 60 0 outside 6
%Flux per Lethargy
ene EnergyGrid 1 0.1 20
det FluxDetector2 ds 1 -2 de EnergyGrid
dep daytot
1
5
20
40
70
100
130
160
190
220
250
280
310
340
370
400
430
460
490
520
550
580
610
640
670
700
```

```
730
760
790
820
850
880
910
940
970
1000
% --- Nuclide inventory:
set inventory
942390
942400
942410
551370
471101
531310
380900
922350
922380
%set bumode 1
%set xenon 1
%set samarium 1
%ifc "/home/28862163/Serpent/PinTrisoRandom/burnup/Fuelface2.ifc"
%ifc "/home/28862163/Serpent/PinTrisoRandom/burnup/buffer.ifc"
%ifc "/home/28862163/Serpent/PinTrisoRandom/burnup/SiC.ifc"
%ifc "/home/28862163/Serpent/PinTrisoRandom/burnup/matrix.ifc"
%ifc "/home/28862163/Serpent/PinTrisoRandom/burnup/Coolant.ifc"
set rfw 1
set nbuf 10
set fpcut 1e-5
set gcu -1
set cmm 0
set shbuf 1 1
set repro 0
```

```
set opti 2
%plot 1 1000 1000
%plot 2 10000 10000
%plot 3 10000 10000
%plot 1 10000 10000 0 -0.62992 0.62992 -0.62992 0.62992
%mesh plots
det fission dr -8 void
mesh 8 3 fission 3  2000  2000
mesh 8 3 fission 1  2000  2000
det RadialFission dr -6 void dm fuel dn 1 0.0 0.409575 4 0 360 1 0 0 1
det RadialCapture dr -2 void dm fuel dn 1 0.0 0.409575 4 0 360 1 0 0 1
```

7.2.2 Cool.ifc

This section shows the SERPENT code used to set temperature for the FCM fuel as an example

```
2 cool 0
1
1 -0.62992 0.62992  1 -0.62992 0.62992 10 -182.499 182.499
-0.7495          561.4196
-0.7418          565.4764
-0.7314          570.7055
-0.7188          576.6423
-0.7050          582.7593
-0.6912          588.5130
-0.6790          593.3920
-0.6696          596.9630
-0.6644          598.9085
-0.6640          599.0558
```

7.3 STACY

This section contains the STACY input file listingi used in the pin model for caesium and placed here as an example as the other inupt filesare variations of this input file.

```
1                                                   !nDifLib
TECDOC.txt                                                  !LibName
.True.                                              !FP_Rel_Input
.True.                                              !CP_Damage_Input
.False.                                             !IfWriteOpSeq
.False.                                             !IfRelativeFP_Release
1                                                   !Nuclide
.False.                                             !If_DiffConcDep
.False. 1.00                                                !If_FE_TempProfile
.False.                                             !If_SiC_Corr
.True.                                              !If_FP_Rel
1                                                   !CP_CalcMode
.False.                                             !IfThicknessDistr.
FCM fuel                                                    OutputTitle
*
*
*
1                                                   !nIntervals
1                                                   !nNOCIntervals
8.6400001E+07                                                       !TE
8.6400E+04                                                  !DT
1                                                   !ORF
F  F  F  F  F  F  F  F  F  F   F   F  T  T  F  F  T  F  F  F
        !If_Output(i). i = 1.20
10                                                  !ORF Output 1
100.                                                !AccTimePlot
2                                                   !Kerneltype
.True.                                              !If_TRISO
5                                                   !nZones_CP
UO2     Buffer  LTI     SiC     LTI                 !Mat_CP
4.00E-02        4.70E-02        5.05E-02        5.40E-02        5.60E-02                !R_CP
39      39      39      39      39                  !nSubzones_CP
50                                                  !VoidFrac
.False.                                             !If_Sphere
.True.                                              !If_Hollow
.False.                                             !If_CalcPlenum
```

```
0                                                   !Ri
364.998                                                 !H
1                                                   !nZones_FE
SiC                                                 !Mat_FE
T                                                   !If_CPs
0.409575                                                !R_FE
50                                                  !nSubzones_FE
3.00E-04                                                !R_Grain
5                                                   !nZones_Grain
151664                                                  !CP_Tot_Numb
1.00E-07    1.00E-07    1.00E-03    1.00E-04    1.00E-06    1.00E-06
        !U_Cont_Grain. U_Cont_Pores. U_Cont_CP(i).
TECDOC-FRG      1                                   !Parameter of Diffusion curve: Pores
(see **. for explanation)
TECDOC-FRG      1                                   !Parameter of Diffusion curve:
Grains (see **. for explanation)
TECDOC-FRG      1                                   !Parameter of Diffusion curve:
Coated Particle Layer 1 (see **. for explanation)
TECDOC-FRG      1                                   !Parameter of Diffusion curve:
Coated Particle Layer … (see **. for explanation)
TECDOC-FRG      1                                   !Parameter of Diffusion curve:
Coated Particle Layer … (see **. for explanation)
TECDOC-FRG      1                                   !Parameter of Diffusion curve:
Coated Particle Layer nZones_CP
TECDOC-FRG      1                                   !Parameter of Diffusion curve:
Coated Particle Layer nZones_CP
TECDOC-FRG      1                                   !Parameter of Diffusion curve:
Coated Particle Layer nZones_CP
0.00E+00    0.00E+00    0.00E+00                        !RecoilLengthCPKernel.
RecoilLengthPyC. RecoilLengthGraphit
2.19400E+01  -4.41E+04      1.13E+00    .False. 0.0
        !Henry1.Henry2.C_Limit.IF_Sorption
2.21100E+01  -4.45E+04      -1.37E+00   3.68E+03
        !Freund1.Freund2.Freund3.Freund4
7.290E-10                                               !DecayConst
Func                                                !Switch
```

```
6       6
d
0       70      250     520     700     1000
1.54E-07        0.969551        3.73262         8.74038         13.1062         24.1308
        !Gamma_EndNOC
1.03                                            !GammaScal
Const                                           !Fission product cencentration in coolant
0.00E+00
6       6                                       !FP Product inventory
d
0       70      250     520     700     1000
0.0     0.0013 0.0046 0.0094 0.0126 0.0179
mol
0.00E+00        !Fission product inventory @ Time = 0 s
        !FP_Inv_FE_Time0
1.79E-02        !End NOC                                        !Inventory_Tot
Lin                                             !Switch
0.2132                                          !Fima_EndNOC
8.34E+08        8.02    3.00E-05        0.31    0.0     .True.
        !Sigma_UnIrr.w_UnIrr.Phi0.FP_Yield.VTU.SiCIrrDepen
0.0001 4                                        !Alpha.Beta
6       6                                       !NumbNOCValues. NumbValPerLine_Input
d                                               !Time Unit NOC
0       70      250     520     700     1000
786     786     786     786     786     786     !NOCTempInVec
2       2                                       !NumbAccValues. NumbValPerLine_Input
h                                               !Time Unit Accident Conditions
0       100
1500    1500                                    !AccTempInVec
18                                              !NumbCP_Damage
6.00E-06                                                !UnitCP_Dam
7.00E-06
9.00E-06
3.00E-05
6.00E-05
9.00E-05
```

```
1.00E-04
5.00E-04
8.00E-04
1.00E-03
5.00E-03
8.00E-03
1.00E-02
5.00E-02
9.00E-02
1.00E-01
5.00E-01
9.99E-01
2147483562
```

7.3.1 TECDOC

```
TECDOC
TECDOC-FRG        ! Name of library
!-------------------------------------------------------------------------------------------------
 4  Cs-137   I-131 Sr-90 Ag-110          ! Number of nuclides
 7  SiC_P   UO2   SiC_G   Buffer   SiC LTI UO2_Def  ! Number of materials
!-------------------------------------------------------------------------------------------------
! Isotope  Material  nBranch   FluenceDep     D0(1)     AE(1)     FluenceDep     D0(2)     AE(2)
Comment
!       [-]  [-]  [cm**2/s]   [J/mol]    [-]  [cm**2/s]   [J/mol]
!-------------------------------------------------------------------------------------------------
 Cs-137 UO2             2        0.0      5.60E-04   209E+03   0.0        5.2E+00      362E+03
 Cs-137 UO2_Def              2        0.0      5.60E-04   209E+03   0.0        5.2E+00
         362E+03
 Cs-137          Buffer          1        0.0      1.00E-04   0.0E+00
 Cs-137 LTI             1        0.0      6.3E-04            222E+03
 Cs-137 SiC             2        5.0      5.5E-14            125E+03      0.0        1.6E-02
         514E+03
 Cs-137 SiC_G                2        5.0      5.5E-14            125E+03      0.0        1.6E-02
```

```
        514E+03
Cs-137        SiC_P        1       0.0     1.00E-04  0.0E+00
Sr-90  UO2           1      0.0     2.20E+01  488E+03
Sr-90  UO2_Def       1      0.0     2.20E+01  488E+03
Sr-90  Buffer        1      0.0     1.00E-04  0.0E+00
Sr-90  LTI           1      0.0     2.30E-02  197E+03
Sr-90  SiC           2      0.0     1.20E-05  205E+03  0.0      1.8E+10     791E+03
Sr-90  SiC_G         2      0.0     1.20E-05  205E+03  0.0      1.8E+10     791E+03
Sr-90  SiC_P         1      0.0     1.00E-04  0.0E+00
Ag-110  UO2         1      0.0     6.70E-05  165E+03
Ag-110 UO2_Def       1      0.0     6.70E-05  165E+03
Ag-110  Buffer       1      0.0     1.00E-04  0.0E+00
Ag-110  LTI          1      0.0     5.30E-05  154E+03
Ag-110  SiC          1      0.0     3.60E-05  215E+03
Ag-110 SiC_G         1      0.0     3.60E-05  215E+03
Ag-110  SiC_P        1      0.0     1.00E-04  0.0E+00
I-131  UO2           2      0.0     8.80E-11  5.4E+04   0.0     6.0E+03
        4.8E+05
I-131  UO2_Def       2      0.0     8.80E-11  5.4E+04   0.0     6.0E+03
        4.8E+05
I-131  Buffer        1      0.0     1.00E-04  0.0E+00
I-131  LTI           1      0.0     1.00E-26  0.0E+00
I-131  SiC           1      0.0     1.00E-26  0.0E+00
I-131 SiC_G          1      0.0     1.00E-26  0.0E+00
I-131  SiC_P         1      0.0     1.00E-04  0.0E+00
End
```